Investigation of Interfacial Engineering and Mechanisms of Water Oxidation under Plasmon-Nanocavity Strong Coupling Conditions

Thesis by

En Cao

In Partial Fulfillment of the Requirements

For the Degree of

Doctor of Philosophy

RESEARCH INSTITUTE FOR ELECTRONIC SCIENCE

HOKKAIDO UNIVERSITY

SAPPORO, JAPAN

2025

Dedication

To my parents and brother for their selfless support and endless love.

Table of contents

Acknowledgement

“I have never been exceptional, but I have never stopped trying.”

In early 2019, when I saw the word “*admitted*”, I quietly held onto this thought. Even now, I can still feel the excitement and joy of preparing for a new life overseas. The road ahead seemed long, and yet 6 years have flown by. As my PhD journey comes to an end, I realize how much I have grown. I am no longer the same inexperienced person I once was. Somewhere along the way, I learned to face challenges on my own and built a sense of belief and purpose that keeps me stronger. Looking back on these 6 years, I have worked hard to achieve many dreams and have also felt the sting of losing things I care about. There were moments of joy and times of struggle. Simply saying “time flies” doesn’t feel enough to capture how I feel now. Writing these words in my way of expressing gratitude-to everyone who has supported and inspired me and to these years of growth, which I will always hold close to my heat.

First and foremost, I would like to sincerely thank my advisor, Prof. Hiroaki Misawa, for accepting me into his group to pursue my PhD. Prof. Misawa is deeply knowledgeable and dedicated to his work. In my academic journey, he has not only provided me with selfless guidance and support, but also profoundly shaped my thinking and scientific approach. His positive attitude and diligent work ethic have greatly inspired me, allowing me to truly understand the meaning of research and science. Through engaging in these challenging and novelty projects, I have gradually come to understand how to become a qualified researcher.

I would like to express my heartfelt thanks to Prof. Xu Shi for your selfless help and guidance during my PhD research. In my experimental work, you offered invaluable advice and direction. Your rigorous thinking and practical experience helped me overcome many challenges in my research. Whenever I faced difficulties in experimental design or data analysis, you were always there to provide guidance, for which I am truly grateful. Moreover, despite your busy schedule, you took the time to review my papers and offer valuable feedback. Your attention to detail and patience have greatly improved my writing. Furthermore, I would like to express my special

thanks to Prof. Quan Sun. It is through your help that I was able to quickly integrate into the laboratory and adapt to life abroad. Your thoughtful care and attention to every detail made me feel warmth even in a foreign country. During the year and a half we spent together, your rigorous academic attitude and diligent work ethic have deeply influenced me. I am truly appreciative of Prof. Tomoya Oshikiri for his invaluable guidance throughout my research process. I am deeply appreciative of the time and effort you devoted to mentoring me, offering insightful feedback, and providing valuable suggestions. I am grateful to Prof. Kosei Ueno for generously granting me access to the experimental equipment, which has been essential for the smooth progress of my research.

I am deeply grateful to Ms. Yumiko Yamaguchi from our research group for your patience and selfless support throughout my entire PhD process. Whether in work or in life, you have always been there to patiently answer my questions and offer valuable advice, helping me advance my research smoothly. Your help has been essential to my successful completion of the PhD.

I am deeply grateful to all the members of Misawa's lab. Mr. Ya-guang Wang, Ms. Xiao-qian Zang, Ms. Yan-feng Cao, Ms. Xin Fan and Mr. Yen-En Liu provided invaluable support when I first arrived in Japan. Throughout my entire PhD research period, they have continued to offer substantial help, both in my research and in daily life. Mr. Yocefu Hattori shared this experience of experiment with selflessly and I am impressed with his humorous personality and outstanding experimental skills. Ms. Lin Qiao provided invaluable assistance during my PhD studies. Due to my limited proficiency in Japanese, she patiently helped me navigate various challenges arising from language barriers. Mr. Yoshiki Suganami, Mr. Minori Ishihara, Mr. Kazuki Furuya, Mr. Fuki Shimizu, Ms. Azusa Onishi introduced a lot of interesting culture to me. They are amazing people who are responsible and hardworking, and I've learned so much. The time spent with my colleagues in Misawa's lab has been the most treasured memory of my PhD journey. Your support and encouragement have not only helped me continuously progress academically but have also filled this journey with friendship and warmth.

I would like to especially thank Prof. Yu-zhi Song and Prof. Meng-tao Sun for their encouragement and comfort during times when my experiments faced setbacks and my mindset was off balance. I am deeply grateful to my friends in China for their encouragement and affirmation during times of uncertainty. Your support and kindness helped me regain confidence and rediscover the motivation to move forward. During this period, your unwavering encouragement and understanding brought me warmth and strength, enabling me to overcome numerous challenges.

Finally, I am grateful for my parent’s respect and support in every decision I have made on my academic journey, always being the unwavering backbone behind my pursuit of dreams and dedication to my work. I also thank my younger brother, who always knows how to make me laugh and forget my worries when I feel down. I am deeply thankful for the constant care and companionship of my parents and brother. I wish for my family's health, safety, and happiness always.

Thesis Abstract

The Au nanostructure (Au NS)/TiO_2 electrode has garnered significant attention for its potential applications in photoelectronic devices, solar cells, and artificial photosynthesis. This potential arises from the generation of hot electrons at the Au NS/ TiO_2 interface when the localized surface plasmon resonance (LSPR) of Au NS is excited under visible light, followed by their injection into the TiO_2 conduction band. However, a single layer of Au NS exhibits low light absorption efficiency and insufficient electron injection into TiO_2. Recent studies in our laboratory have demonstrated that modal strong coupling between the LSPR mode of Au NS and the Fabry-Pérot (FP) nanocavity mode enhances electron injection from Au NS to TiO_2 as well as the quantum efficiency of water oxidation reactions. Improving the electron injection efficiency from Au NS to TiO_2 and elucidating the mechanism of water oxidation under plasmon-nanocavity strong coupling conditions represent crucial and meaningful research directions toward the realization of plasmon-based artificial photosynthesis.

In this doctoral dissertation, I aimed to enhance electron injection by modifying the Au NS/TiO_2 interface with materials that facilitate electron emission under strong coupling conditions. Additionally, the plasmon-nanocavity strong coupling structure was employed to conduct kinetic analyses of the reaction processes involving electrons injected into TiO_2 and holes trapped at the Au NS/TiO_2 interface. Activation energies for the formation of water oxidation intermediates were evaluated to elucidate the mechanism of plasmon-induced water oxidation reactions.

The doctoral dissertation is composed of five chapters, with summaries of each chapter provided below.

Chapter 1 outlines the research background, covering the interaction between light and matter, surface plasmon resonance, plasmon-induced hot electron generation, plasmon-driven light energy conversion, and an overview of the dissertation's structure.

Chapter 2 describes the fabrication of strongly coupled Au nanodisk (ND)/Ti/ TiO_2/Au film (ATTA) structures, where a Ti film with a lower work function than Au

was introduced at the Au ND/TiO_2 interface. Near-field mapping and near-field spectra of ATTA structures with Ti film thicknesses ranging from 0.5 nm to 5.0 nm were measured using a photoelectron emission microscopy (PEEM) system. The results showed that the near-field attenuation increased with the Ti film thickness. Furthermore, time-resolved PEEM measurements using an interferometric pump-probe technique revealed that the phase relaxation time of the hybrid mode in ATTA structures decreased as the Ti film thickness increased.

Chapter 3 investigates the effect of Ti film thickness on the electron injection efficiency at the Au ND/TiO_2 interface. Transient absorption (TA) measurements were conducted to quantify electron injection into TiO_2. Under modal strong coupling conditions, increasing the Ti film thickness from 0.5 nm to 5.0 nm enhanced the apparent quantum efficiency (AQE) of electron injection into TiO_2 by approximately 1.8 times. This enhancement was attributed to energy transfer from the Au ND to the Ti film via the near-field, which generated high-energy electrons in the Ti film that were subsequently injected into the conduction band of TiO_2.

Chapter 4 focuses on the fabrication of strong coupling Au nanoparticle (NP)/ TiO_2/Au film (ATA) structures and the kinetic analysis of reaction processes involving electrons injected into TiO_2 and holes trapped at the Au NP/TiO_2 interface. The activation energy for the generation of water oxidation intermediates was elucidated. Temperature-dependent TA decay curves were used to evaluate the activation energy of electron-hole recombination, revealing that electrons injected from Au NPs into TiO_2 were primarily trapped at shallow trap sites within TiO_2. Additionally, temperature-dependent incident photon-to-current efficiency measurements were performed to determine the activation energy related to photocurrent generation and evaluate the activation energy for water oxidation intermediates. The electrochemical potential levels of holes trapped at the AuNP/TiO_2 interface were also examined. Compared with AT electrodes without strong coupling, ATA structures demonstrated a 40-fold increase in the frequency factor for intermediate generation and a significant improvement in water oxidation efficiency. This enhancement was attributed to quantum coherence in the LSPR of AuNPs facilitated by the nanocavity.

This dissertation demonstrates that modifying the Au ND/TiO_2 interface with Ti films in strongly coupled ATA electrodes improves the electron injection efficiency into TiO_2 and identifies the optimal Ti film thickness for this enhancement. Furthermore, kinetic analyses of temperature-dependent TA and IPCE measurements reveal that quantum coherence in ATA electrodes significantly enhances the efficiency of water oxidation intermediate generation. The findings of this study provide essential guidelines for the design of plasmon-enhanced photocatalytic devices and offer practical insights into improving solar energy conversion and artificial photosynthesis systems. Moreover, the results highlight the potential of leveraging quantum coherence for novel technological advancements, paving the way for future practical applications.

Chapter 1

Introduction

1.1 Background

The use of fossil fuels has been instrumental in significantly advancing our standard of living over the past two centuries, it is now widely acknowledged that the ongoing combustion of fossil fuels and associated release CO_2 into the atmosphere carry significant environmental risks. Decarbonizing energy system is widely acknowledged as a critical step toward stabilizing global temperatures,[1] with studies indicating that achieving net-zero or net-negative emissions by the latter half of this century is essential to limit warming to no more than 2°C.[2] Despite the development of numerous technologies aimed at reducing emissions, they remain prohibitively costly in comparison to fossil fuel combustion, especially as the environmental and health costs associated with fossil fuel emissions are still externalized.

Solar energy, a renewable and carbon-neutral resource, is by far the most abundant energy source, comprising over 99% of all renewable energy available on Earth.[3] However, to effectively replace fossil fuels, large-scale energy storage systems are essential to counteract the intermittent nature of solar irradiation, as well as other renewable sources. Photovoltaic technology directly converts solar energy into electrical and chemical energy, positioning it as a highly effective approach to mitigating the global energy crisis.[4] Water splitting plays a pivotal role, efficiently transforming solar energy into chemical energy and thereby supporting the generation of clean, sustainable energy sources.[5] Semiconductor primarily facilitate the water splitting process under UV-vis light irradiation.[6, 7] In these systems, the semiconductor absorbs a stream of photons, generating high-energy charge carriers in the form of electron (e^-)-hole (h^+) pairs. These charge carriers subsequently separate and migrate to catalytically active sites at the semiconductor/liquid interface, where they drive the chemical reactions. In the case of photocatalytic water splitting process, the energetic holes drive the oxygen (O_2)-evolution half-reaction, while energetic electrons facilitate

the hydrogen (H_2)-evolution half-reaction.[8, 9] one often-used design, first introduced by Fujishima and Honda,[8] utilizes a working n-type semiconductor electrode deposited on a conductive substrate. This electrode is connected through an external circuit to a platinum [10] wire serving as the counter electrode. In this configuration, energetic electrons migrate toward the counter electrode, where they participate in the H_2-evolution half-reaction, while holes contribute to the O_2-evolution half-reaction, as illustrated in Figure 1.1a. However, several inherent constraints have made it challenging to identify effective photocatalysts for water splitting. For instance, n-type semiconductors such as titanium dioxide (TiO_2), with band gaps of 3.0 eV for rutile and 3.2 eV for anatase,[11] restricts their photo-absorption to the UV region of the solar spectrum. Since the UV region constitutes only about 5% of the solar spectrum (Figure 1.1b), wide-bandgap semiconductor materials are unable to effectively harness sunlight to drive the reactions.

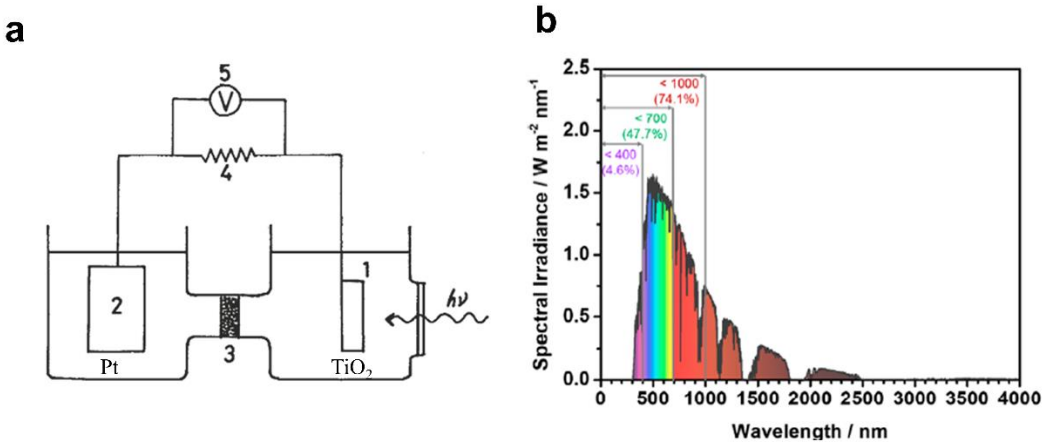

Figure 1.1 Semiconductor photocatalysis. (a) Photochemical cell design for water splitting (processes for an n-type semiconductor are shown).[8] When illuminated with photons ($h\nu$) of energy exceeding the bandgap, excited charge carriers are formed in semiconductor photoanode. The holes diffuse to the semiconductor surface and drive the O_2-evolution half-reaction. Electrons are collected and travel to the counter electrode where they drive the H_2-evolution half-reaction. (b) The composition of solar energy is approximately 5% ultraviolet light; 43% visible light and 52% near infra-red radiation.[13]

The use of semiconductors for photochemical water splitting faces several challenges. First, their light absorption efficiency is limited, primarily in the UV-visible range, leaving most of the solar energy in the near-infrared spectrum underutilized. Second,

photogenerated charge carriers tend to recombine quickly, reducing the efficiency of charge separation and hindering the sustained water splitting reaction. Third, the catalytic efficiency of semiconductor surfaces is often low, requiring co-catalysts, but their introduction can create new recombination sites, diminishing overall performance. Additionally, the bandgap of semiconductors must be properly tuned to drive both water oxidation and reduction reactions, which limits material choices. One class of these materials comprises co-catalyst nanoparticles, such as Pt,[14] gold (Au),[14-16] and silver (Ag),[17, 18] which are deposited directly onto the semiconductor. Typically, the role of the co-catalyst is to facilitate catalytic reactions by providing active sites and prolonging the lifetime of energetic charge carriers that reach the semiconductor surface by enhancing the rate of electron-hole separation at the plasmonic-metal/semiconductor interface.[19] A unique characteristic of composite photocatalysts compose of semiconductor and plasmonic-metal nanostructures is that plasmonic nanostructures interact with light via the excitation of localized surface plasmon resonance (LSPR). Strong evidence indicating that LSPR significantly enhances the rate of photocatalytic reactions on adjacent semiconductor has been demonstrated through measurements of rate enhancements induced by plasmonic metals as a function of excitation wavelengths. These measurements revealed that for all investigated reactions, including the O_2- and H_2-evolution half-reactions across various semiconductors, the highest rate enhancements occurred at wavelengths corresponding to the LSPR of the metals.[18, 20-25] These studies conclusively established a positive correlation between LSPR intensity and rate enhancements, leading to the hypothesis that metallic LSPR enhances the rates of photocatalytic reactions on nearby semiconductors by transferring energy to them and increasing the steady-state concentration of chemically useful energetic charge carriers. In such a plasmonic-metal/semiconductor system, charge carriers are directly injected from the excited plasmonic-metal nanostructures into the semiconductor.[16, 26] The charge injection mechanism is analogous to dye sensitization, in which a dye molecule anchored to a semiconductor absorbs light and transfers energetic charge carriers to the semiconductor.[27, 28] In this context, as shown Figure 1.2, metallic plasmonic nanoparticles function similarly to dye sensitizers by absorbing resonant

photons and transferring the energetic electrons generated during the LSPR excitation to the adjacent semiconductor. Plasmonic metal nanostructures exhibit excellent charge carrier mobility and high absorption cross-sections, which, under resonance conditions, can be up to 10^5-fold larger than the cross-sections of typical dye-sensitizer molecules. As a result, they represent highly promising sensitizers.[20] Furthermore, the ability to tune the resonance wavelength by altering the size or shape of the nanostructures suggests that plasmonic-metal sensitizers can effectively exploit the entire solar spectrum.[29] In our previous study, we demonstrated plasmonic photocurrent generation from visible to near-infrared wavelengths using an electrode composed of Au nanostructures deposited on a TiO_2 substrate. [30-33] However, the LSPR of monolayer Au NPs on a TiO_2 substrate suffers a low light absorption efficiency, resulting in a low quantum yield for water oxidation. Very recently, we developed a TiO_2 electrode with an optical nanocavity by depositing TiO_2 on a gold reflective film and supporting gold nanoparticles (Au NPs) on top (denoted as Au NPs/TiO_2/Au film: ATA), achieving modal strong coupling between cavity resonance and LSPR.[34-36] A notable advantage of ATA is its significantly enhanced absorption intensity in the visible region and its broader wavelength range compared to Au NPs/TiO_2 (AT) without a nanocavity. As a photoanode, ATA has demonstrated improved quantum efficiency for water oxidation relative to the conventional AT photoanode.

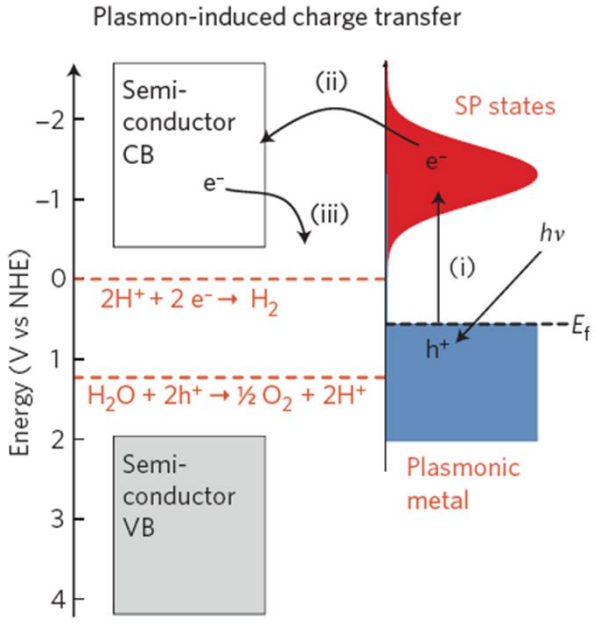

Figure 1.2 Mechanism of LSPR-induced charge transfer in plasmonic-metal/semiconductor photocatalysis. The dashed red lines represent the water-splitting redox potentials. The process involves three key steps: (i) Electron near the metal's Fermi level are excited to surface plasmon states; (ii) these excited electrons are transferred to the adjacent semiconductor; (iii) the transferred electrons drive electron-mediated processes, such as the hydrogen-evolution half-reaction.[12]

Although numerous studies have investigated water splitting using Au/TiO_2 heterostructures, including our group, the influence of rationally modulating the interfacial structure on electron injection efficiency remains underexplored. Since the Au/TiO_2 interfacial structure plays a critical role in electron transfer reactions, understanding its structural effects is crucial. Moreover, while plasmon-nanocavity strong coupling has been shown to enhance the quantum efficiency of water oxidation, the underlying plasmon-induced water oxidation reaction kinetics are still insufficiently studied. The activation energy for the formation of water oxidation intermediates, which serve as precursors in the water oxidation process under strong coupling conditions, remains unclear. This thesis aims to address these gaps by modifying the Au/TiO_2 interface to enhance electron transfer from Au nanoparticles to TiO_2 and to elucidate the activation energy of water oxidation under strong coupling conditions.

1.2 Light matter interaction

From ancient times to nowadays, light has been integral to the lives of biological species, from plant photosynthesis to human vision and countless examples. With advancements in modern technology, scientists can now manipulate light across the entire electromagnetic spectrum-from gamma rays to radio waves-leading to significant progress in various aspects of daily life. The interaction between light and matter is a fundamental area of optical and photonics science, with extensive applications across physics, chemistry, biology, and medicine. Consequently, exploring the mechanisms of light-matter interactions and engineering their optical and electromagnetic properties have become major focal points in scientific research. In recent decades, as research has shifted from the microscale to the nanoscale, the unique ability to concentrate and manipulate light through coupling with nanostructured materials has been explored,

achieving significant optical responses and field enhancements. This progress opens promising avenues in nonlinear optics,[37] solar energy conversion,[38] photocatalysis,[12, 39] and sensing.[40]

1.2.1 Fundamentals of light: Electromagnetic wave propagation

The modern electromagnetic theory of light originated from James Clerk Maxwell's groundbreaking work in the 1860s. Later, Josiah Willard Gibbs and Oliver Heaviside independently reformulated Maxwell's ideas into the vectorial representations widely used today. Maxwell's contributions were initially presented in two seminal papers, *"On the Physical Lines of Force"* and *"A Dynamical Theory of the Electromagnetic Field."* Through this work, Maxwell unified the concepts of light, electricity, and magnetism, which were subsequently consolidated into the four differential equations now known as Maxwell's equations. These equations establish the foundational link between electromagnetic waves and light, encompassing wavelengths from long radio waves to short ultraviolet light. Maxwell's equations provide a mathematical framework describing the spatial and temporal propagation of electromagnetic waves within materials:

$$\nabla \cdot \vec{D} = \rho \quad (1.1)$$

$$\nabla \cdot \vec{B} = 0 \quad (1.2)$$

$$\nabla \times \vec{E} = -\frac{\partial \vec{B}}{\partial t} \quad (1.3)$$

$$\nabla \times \vec{H} = \frac{\partial \vec{D}}{\partial t} + \vec{J} \quad (1.4)$$

Here $\vec{D}$ is the electric displacement, $\vec{E}$ is the electric field, $\vec{B}$ is the magnetic induction, ρ is the free charge density, $\vec{H}$ is the magnetic field and $\vec{J}$ is the current density. In a linear and isotropic medium, the magnetic induction $\vec{B}$ and electric displacement $\vec{D}$ are constituted by two terms: one component is the electromagnetic wave in vacuum and the other is the polarization ($\vec{P}$) or magnetization ($\vec{M}$), respectively. The constitutive relations are denoted as follows:

$$\vec{D} = \varepsilon_0 \vec{E} + \vec{P} = \varepsilon_0 \varepsilon \vec{E} \quad 1.5$$

$$\vec{B} = \mu_0 \vec{H} + \vec{M} = \mu_0 \mu \vec{H} \quad 1.6$$

Where ε_0 is the vacuum electric permittivity, μ_0 is the vacuum magnetic permeability. The overall response can be expressed by the relative electric permittivity ε and relative magnetic permeability μ of the medium. Both ε and u are dimensionless complex numbers (strictly speaking, both are second-rank tensors), depending on the frequency of radiation. The real part reflects the magnitude of polarization or magnetization, indicating the material's ability to respond to an electromagnetic field, while the imaginary part represents the absorption loss, characterizing the energy dissipated within the material.

$$\varepsilon = \varepsilon' + i\varepsilon' \quad 1.7$$

$$\mu = \mu' + i\mu' \quad 1.8$$

These two parameters characterize the interaction between the electromagnetic wave and the medium. They enable the description of the wave's response to the medium, specifically through the refractive index n, which determines the wave's phase velocity, and the wave impedance z, which governs the relationship between the electric and magnetic fields within the medium.

$$n = \sqrt{\varepsilon \mu} \quad 1.9$$

$$z = \sqrt{\frac{\mu}{\varepsilon}} \quad 1.10$$

The refractive index n is defined as the ratio of the speed of light in a vacuum (c) to its speed (v) in a given medium: $n = c/v$. On the other hand, the wave impedance zzz quantifies the material's resistance to wave propagation. These parameters are crucial for characterizing the interaction between light and matter. Determining their values is essential when designing devices and selecting appropriate material combinations to achieve specific optical functionalities, such as strong light confinement, high absorption, enhanced transmission, reduced reflection, or other tailored optical properties.

1.2.2 Optical properties of metals

For metallic materials, their optical properties are predominantly governed by the behavior of conduction electrons, which impart their characteristic shiny appearance. As depicted in Figure 1.3, the real part of the electric permittivity, $Re(\varepsilon)$, for gold remains negative across the displayed wavelength range. This negative value arises from free electrons oscillating out of phase with the applied electric field, effectively shielding the electromagnetic wave and yielding a reflectivity close to unity. However, when the frequency of the incident light exceeds the plasma frequency (ω_p), typically located in the ultraviolet region and corresponding to the natural oscillation frequency of free electrons, the electrons can no longer keep pace with the oscillating electromagnetic field. Under these conditions, the metal loses its high reflectivity, allowing electromagnetic radiation to penetrate into the bulk, albeit with significant damping.

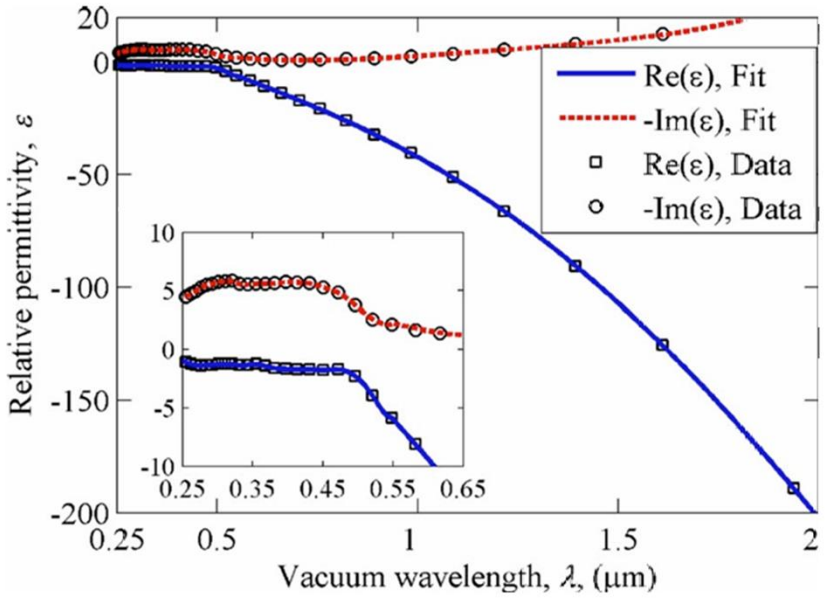

Figure 1.3 The real and imaginary components of the relative permittivity of gold are plotted as functions of wavelength, spanning from 250 nm to 2 μm. The inset provides an enlarged view of the material's dispersion characteristics within the visible and ultraviolet ranges, offering a detailed perspective on the behavior of gold in these spectral regions.[41]

1.3 Surface plasmon resonance

Surface plasmons (SPs) enhance light-matter interaction through the collective oscillation of free electrons, generating strong electromagnetic fields at the excited metal nanostructure's surface. The use of SPs for light scattering and absorption date back over a thousand years, exemplified by the incorporation of noble metal particles in glass to create stained glass vessels and windows.[42] Recently, SPs-based photonics and plasmonics have been used to enhance light-matter interactions at the nanoscale, enabling precise control over light emission,[43] propagation,[44] and localization.[45] Plasmonics has become a prominent research area with numerous applications, including in the development of metamaterials,[46, 47] optical cloaking,[48] and lasers.[49] Furthermore, plasmonics has been used to improve the performance of devices such as photodetectors,[50, 51] photovoltaic cells,[52, 53], and sensors.[54, 55] Generally, SPs exist in two primary modes: localized surface plasmon resonances confined to the surfaces of metal nanoparticles and propagating surface plasmon polaritons along planar interfaces.

1.3.1 Localized surface plasmon resonance

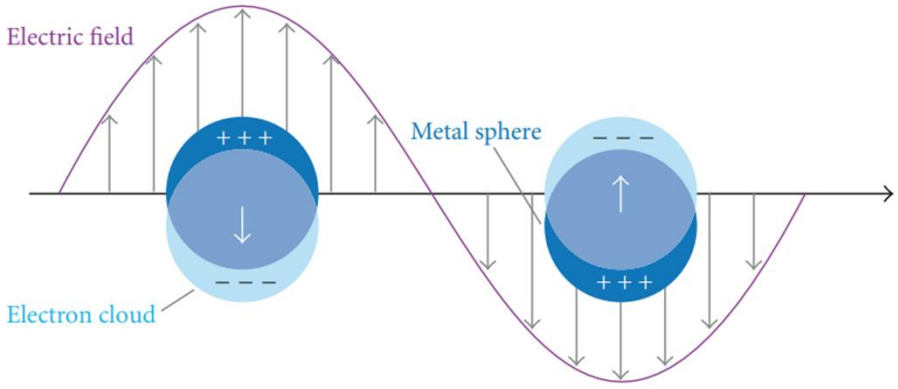

Figure 1.4 Representation of localized surface plasmon resonance in metal nanoparticles.[56]

Localized surface plasmon resonances (LSPRs) arise from the collective oscillation of free electrons in metal nanostructures when excited by an external electromagnetic field. This interaction leads to a resonant oscillation between electron motion and the electromagnetic field, as depicted in Figure 1.4. One of the earliest applications of

LSPR can be traced back to the Lycurgus Cup, crafted during Roman times and now displayed at the British Museum (see Figure 1.5). This artifact contains nanoscale gold and silver particles embedded in glass, which enable surface plasmon excitation when illuminated. Consequently, the cup's color changes depending on the light source's position: it appears greenish when the source is outside and reddish when the source is inside. These effects arise from the differing absorption and scattering of light across various wavelength ranges.

Over the years, extensive research has utilized the LSPR properties of noble metal nanostructures in diverse fields, including catalysis,[57] Surface enhanced Raman scattering,[58] and sensing[59]. The characteristics of LSPR are highly sensitive to factors such as the material, shape, size, composition, and dielectric environment of the metallic nanostructure. By adjusting these parameters, the LSPR wavelength can be tuned across the visible, near-infrared, and even far-infrared spectral regions, enabling tailored applications that require specific wavelengths.

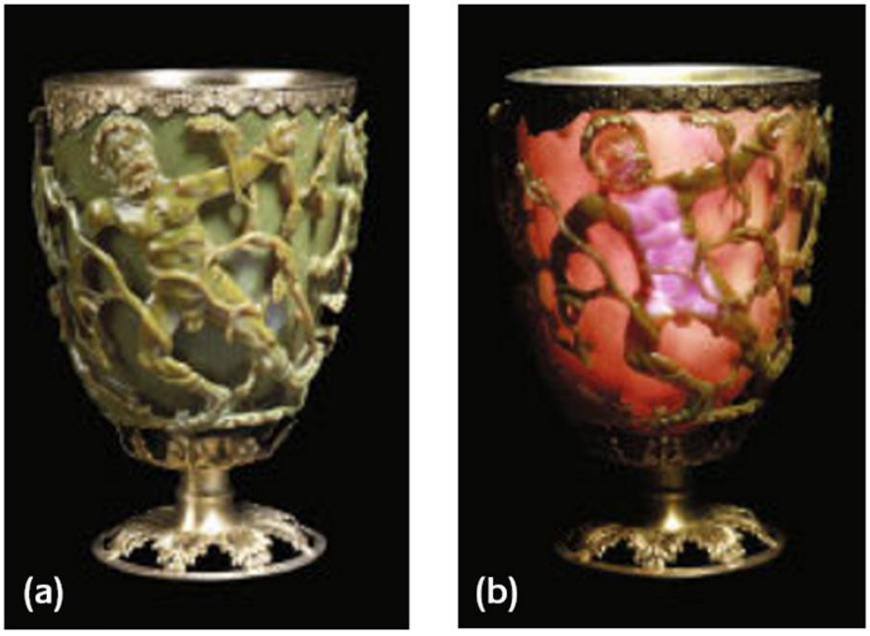

Figure 1.5 The Lycurgus cup, 4th century A.D. The cup shows greenish color when irradiated from outside (a), and reddish color when irradiated in the cup (b). [60]

1.3.2 Influence of size, shape, and material on plasmon resonance

As described by Mie theory, when the radius of spherical particles is smaller than

the wavelength of incident light, the LSPR absorption and scattering cross-sections can be expressed as follows:[61]

$$C_{sca} = \frac{8\pi}{3} k^4 r^6 \left|\frac{\varepsilon-\varepsilon_m}{\varepsilon+2\varepsilon_m}\right|^2 \quad 1.11$$

$$C_{abs} = 4\pi k r^3 Im\left|\frac{\varepsilon-\varepsilon_m}{\varepsilon+2\varepsilon_m}\right| \quad 1.12$$

where ε and ε_m are dielectric function of metal and medium respectively. $k = 2\pi/\lambda$ is the wavenumber, and r is the radius of metal nanoparticles.

From these functions, it can be concluded that both C_{sca} and C_{sca} are related to the radius of metal nanoparticles. Specially, C_{abs} is proportional to r^3, while C_{sca} scales with r^6. Consequently, as particle size increases, scattering becomes the domination effect, as indicated by the relationship between C_{sca}/C_{abs} and radius of particles (Figure 1.6a).

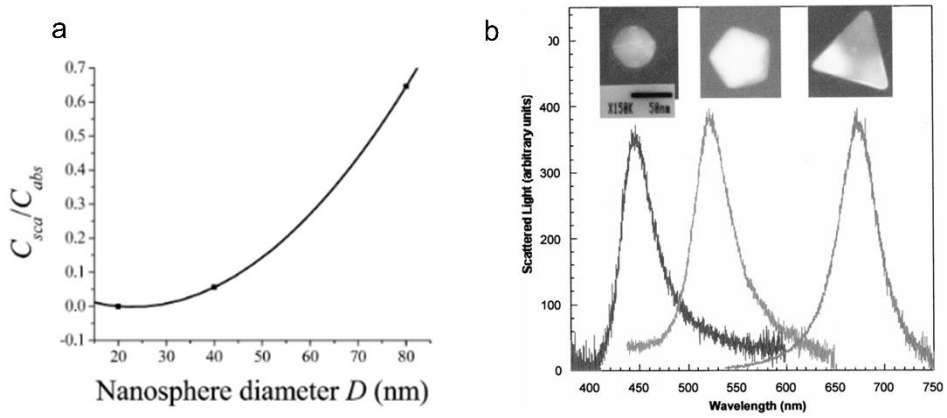

Figure 1.6 (a) Correlation between C_{sca}/C_{abs},[62] and (b) scattering spectra of silver nanoparticles with different sizes and shapes.[63]

While Mie theory simplifies by assuming spherical nanoparticles, extensive experiments and calculations have shown that plasmonic properties are indeed shape-dependent. Gbgb et al. fabricated metal nanoparticles in various shapes, revealing that the LSPR wavelength shifts according to particle geometry, as illustrated in Figure 1.6b.

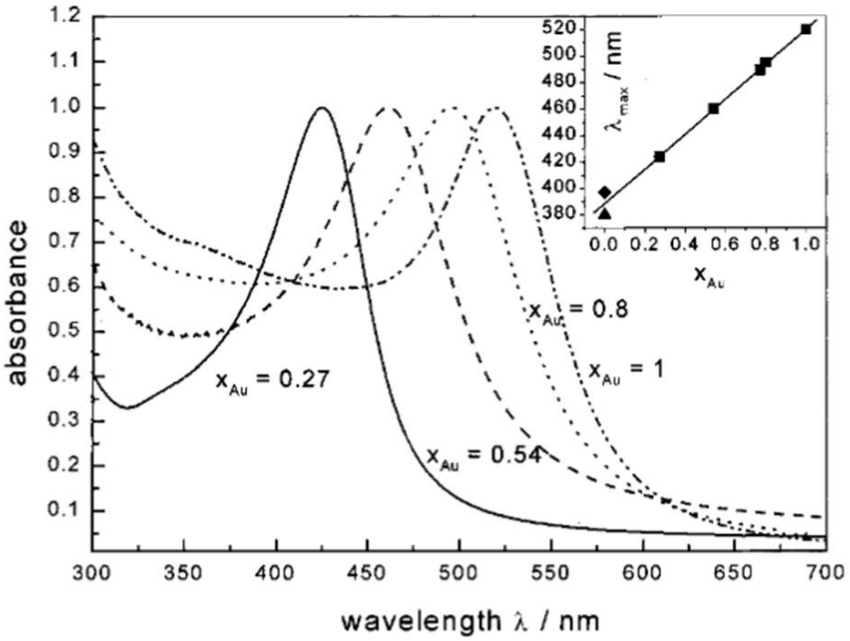

Figure 1.7 Absorption spectra of Au and Au-Ag alloy NPs with varying of Au content are shown. The inset figure indicates the correlation between the absorption peak position and the Au fraction.[64]

In addition to size and shape, the intrinsic properties of metals also affect plasmon behavior. The frequency of LSPR is influenced by the dielectric constant of the surrounding medium ε_m and must satisfy the condition $\varepsilon_1 = -2\varepsilon_m$. Consequently, different metals exhibit distinct LSPR frequencies. For instance, the real and imaginary components of the dielectric functions of Ag and Au are shown in Figure 1.7. Link et al. fabricated Au-Ag alloys and investigated the absorption dependence on alloy composition, finding that increasing the Au content induces an LSPR red shift.[64]

1.4 Plasmon-induced hot electron generation

The remarkable capabilities of surface plasmons to harvest incident photons and concentrate electromagnetic fields have enabled numerous applications in plasmonics. LSPR occurs in well-designed nanostructures, where free electrons oscillate with the same frequency as the incident radiation and eventually enter resonance, generating intense, highly localized electromagnetic fields. Upon LSPR excitation, plasmons undergo decay, transferring accumulated energy to conduction band electrons, thereby

generating energetic electrons (as known as hot electrons).

1.4.1 Hot electron generation through LSPR decay

Hot electrons are high-energy electrons above the Fermi level that exist in non-thermal equilibrium with the lattice. When metal nanostructures absorb incident photons, hot electron are generated and emitted through the photoelectric effect.[65] Recent advances in this field focus on enhancing hot electron generation via surface plasmon decay.[66] Plasmons decay within a femtosecond timescale, either radiatively (re-emitting photons) or non-radiatively through intraband and interband excitations, thereby creating energetic hot electrons (Figure 1.8). This process, known as Landau damping, generates hot electrons with effective temperatures surpassing the lattice temperature, driven by plasmonic resonance.[67] Therefore, maximizing hot electron production requires optimizing the non-radiative decay pathway relative to radiative processes, minimizing re-radiation for greater efficiency.

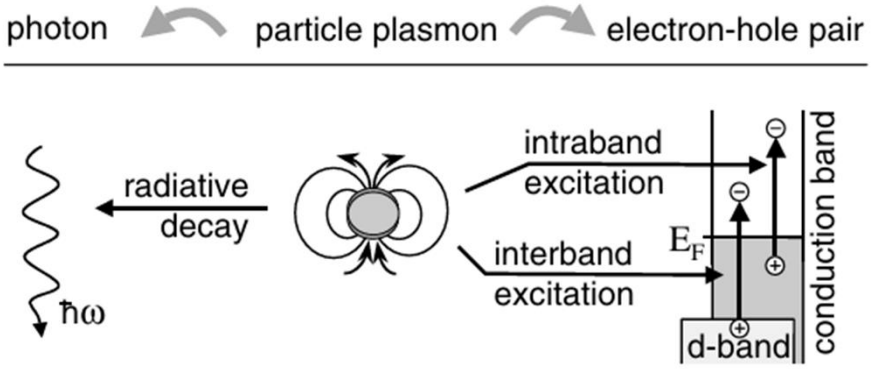

Figure 1.8 Surface plasmon decay and hot electron generation. LSPR can decay via reemitted photons or non-radiatively via excitation of hot electrons. (In noble-metal nanostructure, non-radiative decay can occur through intraband within the CB or through interband excitations resulting from transitions between other bands ((e.g,. d bands) and the CB).[68]

Photoexcitation of LSPR channels light into metallic nanoparticles, where Landau damping typically occurs on a timescale of 1~100 fs. During this period, the hot carrier distribution is highly athermal: hot electrons exceed the Fermi level in energy, while hot holes below the Fermi level (Figure 1.9b). Over the subsequent 100 fs to 1ps, energy

redistribution among hot carriers take place via electron-electron scattering (Figure 1.9c). Finally, thermal energy is transferred to the surrounding environment through conduction, a process that typically spans 100 ps to 10 ns, depending on the metallic material, nanoparticle size, and heat transfer characteristic of the surrounding medium, as shown in Figure 1.9d.[69]

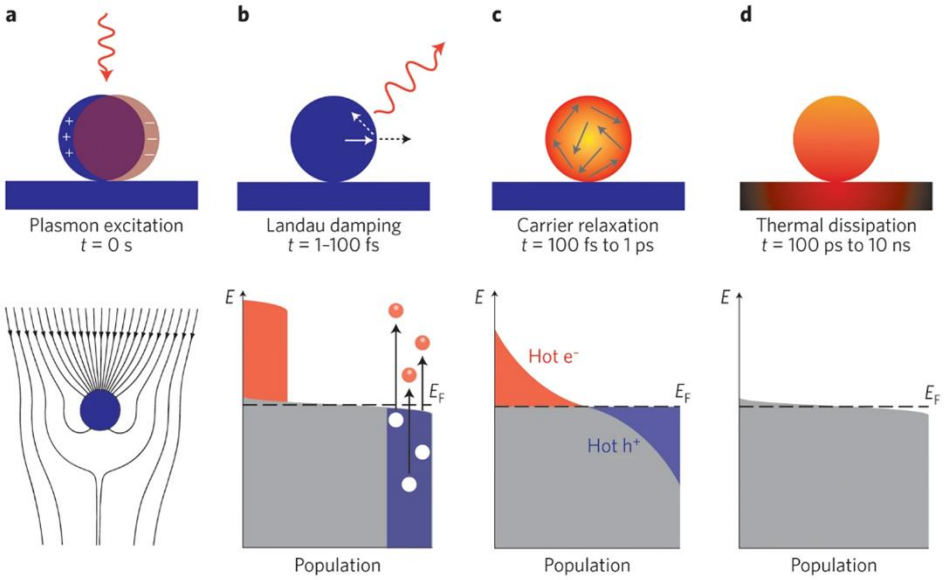

Figure 1.9 Photoexcitation and relaxation of metallic NPs. (a) Distribution of electromagnetic field under the LSPR excitation. (b-d) Representation of electronic states (grey) after plasmon excitation, with hot electrons [70] above the Fermi level E_F and hot holes (blue) below E_F . (b) Landau damping occurs within 1–100 fs, producing a non-thermal distribution of excited electron-hole pairs. (c) Hot carriers redistribute their energy through electron-electron interactions, leading to thermal equilibration. (d) Over a longer timescale of 100 ps to 10 ns, energy is transferred to the surroundings of the metallic structure via thermal conduction.[69]

1.4.2 Plasmon-induced hot electron injection

Hot electrons generated via non-radiative plasmon decay in isolated plasmonic nanostructure typically lose energy through collisions with other electrons and phonons, ultimately dissipating as heat.[71] However, by employing a Schottky barrier at the interface between a plasmonic metal and semiconductor, these electrons can be effectively transferred. As illustrated in Figure 1.10, when a plasmonic metal is in contact with a semiconductor, hot electrons with sufficient energy can either overcome or tunnel through the Schottky barrier at the interface. Notably, the energy required for this process only needs to surpass the Schottky barrier height, which is significantly

smaller than the bandgap of the semiconductor.

The hot electron injection mechanism into the semiconductor proceeds through three steps: (1) the plasmonic nanostructure absorbs incident photons, exciting electrons to higher energy states; (2) the excited hot electrons migrate towards the plasmonic metal /semiconductor interface before thermalization occurs; and (3) upon overcoming the Schottky barrier, the hot electrons are injected into the CB of semiconductor via internal photoemission, enabling their extraction as electric current through an external circuit.

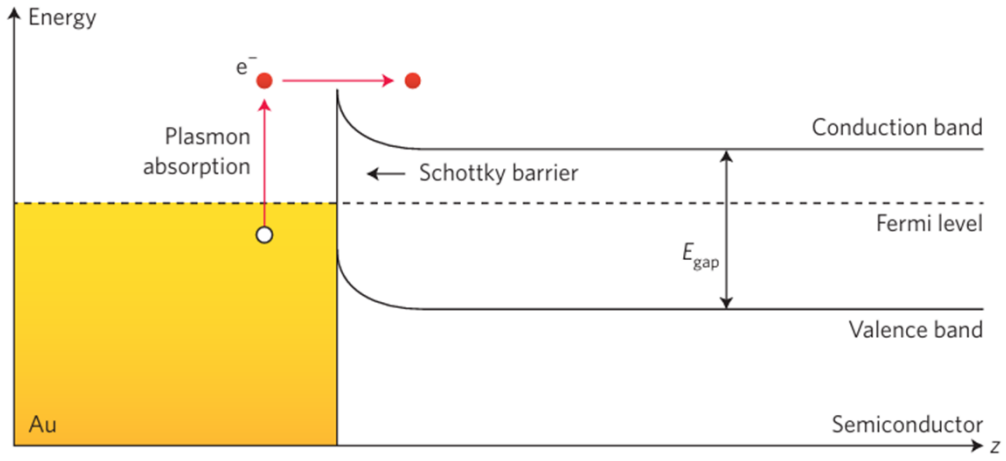

Figure 1.10 Upon plasmon excitation, hot electron generated during plasmon decay can acquire enough energy to across the Schottky barrier at the metal/semiconductor interface. This energy requirement is determined through the Schottky barrier height, which is substantially lower than the bandgap energy (E_{gap}) of semiconductor, enabling efficient electron transfer.[65]

One-dimensional (1D) plasmonic-metal/semiconductor heterostructures, as depicted in Figure 1.11a, represent a foundational model for advancing surface plasmon-induced charge and energy transfer processes.[72, 73] Recent studies have extensively investigated the mechanisms underlying the conversion of plasmon-induced hot electrons, with the conventional plasmon-induced interfacial hot electron transfer (PIHET) being one of the most well-characterized (Figure 1.11b). In PIHET, photoexcited plasmons decay into electron-hole pairs within the plasmonic metal, after which hot electron across the barrier enter the CB of semiconductor.[73, 74] However, the efficiency of PIHET is constrained by ultrafast electron-electron and electron-phonon scattering losses, as well as the requirement for electron momentum conservation at the metal/semiconductor

interface.[75, 76]

An alternative mechanism, plasmon-induced interfacial charge-transfer transition (PIICTT), has been proposed to address these limitations. Driven by interfacial plasmonic coupling, PIICTT facilitates rapid excitation generation at the plasmonic interfacial via coupling and damping mechanisms, as shown in Figure 1.11c.[77] In this process, photoexcited plasmons generate holes below the Fermi level in the metal and simultaneously inject electrons into the CB of n-type semiconductor. Wu et al. demonstrated this mechanism in an Au-CdSe nanorod system, showing that PIICTT achieves higher quantum efficiency (> 24%) than PIHET process due to its ultrafast operation (< 10 fs), which occurs before significant plasmon energy dissipation as heat.[74]

In addition to PIHET and PIICTT, plasmon-induced resonant energy transfer (PIRET) offers another pathway for plasmon-enhanced solar energy harvesting (Figure 1.11d). PIRET involves the transfer of absorbed energy from the plasmonic metal to semiconductor through dipole-dipole coupling, generating electron-hole pairs near the semiconductor's band edge. For instance, Wu et al. also developed a plasmonic-Au@SiO_2@Cu_2O heteronanostructure, where PIRET dominates due to the insulating SiO_2 layer preventing direct charger transfer across the heterointeface.[78, 79] Similarly, Oener et al. designed a plasmonic-Au-Pd@Al_2O_3@SiN heterojunction nanowire network, where the Al_2O_3 layer reduces charge-carrier recombination and mitigates Fermi level pinning.[80] This heterojunction network demonstrated superior performance compared to traditional p-n heterojunction solar cells, achieving enhanced open-circuit voltage and short-circuit current density.

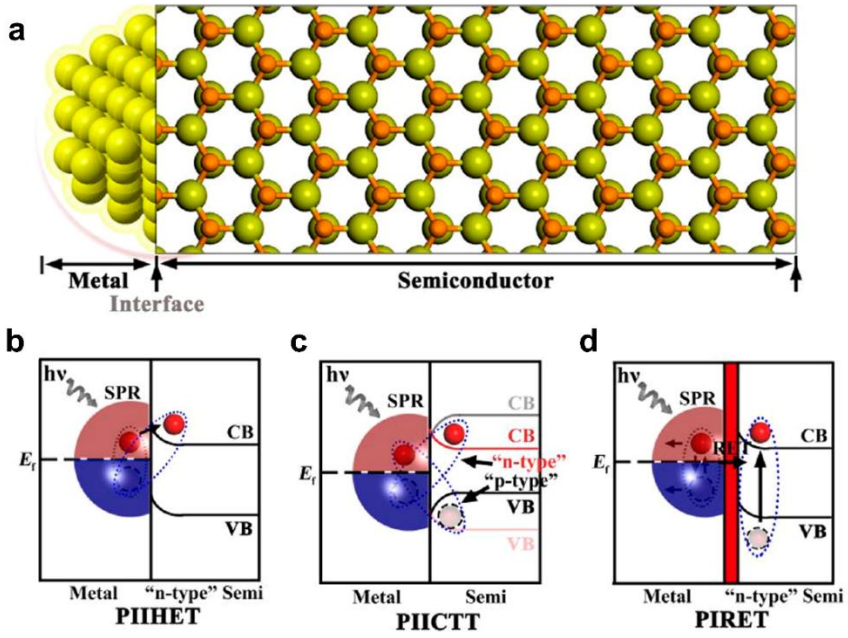

Figure 1.11 Plasmon-induced hot electron injection. (a) Schematic diagram of a plasmonic-metal/semiconductor heteronanostructure, (b) plasmon-induced interfacial hot electron transfer (PIIHET) process, (c) plasmon-induced interfacial charge-transfer transition (PIICTT) process, and (d) Plasmon induced resonant energy transfer (PIRET) process. CB and VB refer to conduction band and valence bands. Panels (b)-(c) also indicate schematically the Schottky barriers between the metal and semiconductor parts. For clarity, no more than two electron-hole pairs are shown.[81]

1.4.3 Effect of interfacial structure on electron injection

The enhanced properties of plasmonic metal/semiconductor nanocomposite photocatalysts, particularly when coupled with metal NPs, can be attributed to two main mechanisms: improved charge separation at the metal/semiconductor interface and enhanced visible light absorption due to the LSPR of the metal. Rational modulation of the heterointerfaces plays a crucial role in influencing charge transfer properties, thus directly determining the overall photocatalytic performance.

A key parameter in interface engineering is interfacial composition, which affects the component's abilities in light absorption and surface reactions. Typically, interfacial composition is controlled by introducing new components into the hybrid structure. For example, Li et al. enhanced the solar energy conversion efficiency of the Au/TiO_2 system for plasmon-induced water oxidation by intercalating Li^+ ions into TiO_2 film. This modification resulted in a remarkable 33-fold increase in photocurrent density and

a maximum IPCE of 2.0% in the Au/$Li_{0.2}TiO_2$ system, compared to the bare Au/TiO_2 system.[82]

The interfacial area also plays a significant role in enhancing photocatalytic efficiency. Core-shell structures, where the metal core is fully encapsulated by a semiconductor shell, maximize the heterogeneous contact interface, providing efficient charge transfer channels. These structures not only enhance electron transfer but also prevent particle aggregation and protect the metal core from corrosion or dissolution during the photocatalytic process. For instance, Wu et al.[83] demonstrated that a hexagonal closed-packed core-shell Au/TiO_2 array structure exhibited a 20% increase in H_2 production under both UV and visible light, outperforming bare TiO_2 thin films and randomly distributed Au/TiO_2 structures.

Moreover, the facets of the contacting components influence interfacial charge transfer efficiency. Our group studied the effect of Au NP-loaded STO with different facets as photoanodes for plasmon-induced water oxidation. The Au NP-loaded STO (100) facet exhibited the highest photocatalytic activity, showing more than 1.4 times greater photochemical water oxidation efficiency compared to the (110) and (111) facets.[84]

For plasmonic hot electron collection, overcoming the Schottky barrier at the metal/semiconductor interface is essential. Zheng et al. showed that incorporating a 2 nm Ti layer at the Au/TiO_2 interface aligned the Fermi level of Au with the conduction band of TiO_2, forming an ohmic contact that significantly enhanced electron transfer efficiency.[85] Similarly, the incorporation of a 1-2 nm Ti layer into the Au/Si interface reduced the Schottky barrier height from 1.1 eV to 0.5 eV, further improving the electron transfer process.[86]

1.5 Plasmon-induced light energy conversion

Photocatalysis and photovoltaics are two primary methods for solar energy conversion, both dependent on light absorption and the generation and separation of charge carriers within semiconductors. However, enhancing their efficiency remains

challenging due to inherent limitations of semiconductors, such as restricted light absorption and rapid charge recombination. A promising approach to overcome these challenges is the integration of plasmonic nanostructures with semiconductors. These nanostructures act as subwavelength antennas that concentrate light, thus enhancing the local electromagnetic field and promoting efficient electron-hole separation. Moreover, plasmonic nanostructures absorb light through the collective oscillations of surface electrons, facilitating the excitation and direct injection of free electrons into the conduction band. This process can drive chemical reactions or generate electricity. In summary, incorporating plasmonic nanostructures into photocatalysis and photovoltaics offers a promising strategy to improve solar energy conversion efficiency.

1.5.1 Plasmonic thin film energy conversion

Photovoltaic (PV) cells offer the potential for virtually unlimited clean energy by efficiently converting sunlight into electrical power. Si has traditionally been the material of choice for PV cells due to its low cost, abundance, non-toxicity, and well-established processing technology. However, to enable large-scale implementation, the cost of current PV modules must be significantly reduced, and efficiency must be substantially increased. Thin-film, second-generation silicon solar cells present a promising solution, owing to their lower material and processing costs.[87] Unfortunately, the light absorption depth in silicon is much greater than the electronic diffusion length in thin-film materials, particularly for photon energies near the bandgap. This disparity leads to lower energy conversion efficiencies in these cells compared to traditional crystalline, wafer-based cells.

As discussed in 1.3, surface plasmon excitations offer unique advantages in light concentration and trapping. Recently, metallic nanostructures have garnered renewed attention for PV applications, spurred by advancements in fabrication techniques and a growing understanding of their optical properties within the field of plasmonics.[44] In various cell designs, both near-field light concentration at individual particle resonances and effective light trapping using nanometals have been explored.[88-93] Experimental results have shown peak enhancements in the tens of percentage points at specific

wavelengths, with overall efficiency improvements of 8.3%, and 8% for cells using a-Si,[91] and GaAs,[94] respectively. Additionally, efforts to improve the omni-directional absorption characteristics for solar tracking and operation in diffuse sunlight have been pursued.[95] There is also a clear need for optimization strategies that provide broadband absorption enhancements across the entire solar spectrum. With recent advances in full-field electromagnetic simulations and computational power, robust optimization tools have been developed and are now widely used within the PV community, making such optimizations increasingly feasible.[96-98]

1.5.2 Plasmonic water splitting

Despite decades of research since the seminal work of Fujishima and Honda in 1972,[8] no photocatalyst has yet been developed that satisfies all of these requirements. Common semiconductor photocatalysts, such as TiO_2 and ZnO, are limited by their large bandgaps (~3.2 eV), restricting them to absorbing only ultraviolet light.[99] Other materials, like α-Fe_2O_3, are responsive to visible light but suffer from short minority carrier diffusion lengths and slow OER kinetics.[100] Consequently, the overall efficiency of solar water splitting systems remains insufficient for practical applications.

To enhance the performance of semiconductor photocatalysts, integrating noble metal nanoparticles is a highly effective strategy, leveraging the plasmonic effect. Noble metal nanoparticles, such as Au and Ag, exhibit LSPR when interacting with visible and near-infrared light. This interaction generates a significant electromagnetic field enhancement around the metal NPs, which can be several orders of magnitude stronger than the incident light fields.[44, 101, 102] Recent studies on plasmon-enhanced water splitting have identified two key mechanisms: (1) The electromagnetic field enhancement effect, associated with the plasmon-resonant energy transfer mechanism, promotes water splitting reactions when photocatalysts sensitive to visible light are employed, as depicted in Figure 1.12a. (2) The more widely recognized mechanism involves plasmon-induced charge separation, where efficient electron transfer from the metal nanoparticle to the semiconductor occurs, driving the photolysis of water. This process is often referred to as the hot electron-transfer mechanism, as shown in Figure

1.12b.

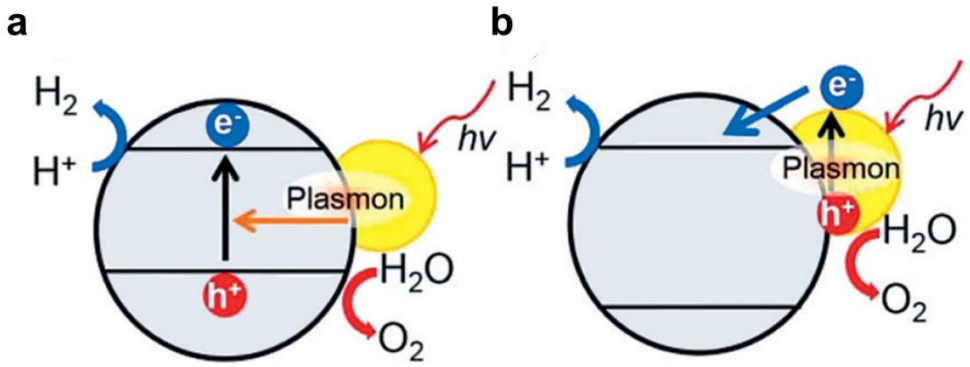

Figure 1.12 Schematic illustrations of reaction scheme using Au NPs-loaded semiconductor.[103]

Research on LSPR-induced electron transfer has predominantly focused on the Au-TiO_2 system. Early studies on the photoelectrochemical properties of TiO_2 films containing Au/Ag NPs revealed that these NPs significantly enhanced the photocurrent.[104] The first demonstration of the hot electron injection mechanism was carried out by Tian and Tatsuma, who employed an electrolyte-based plasmon-enhanced energy conversion system. Their results showed that the IPCE of the optimized Au/TiO_2 anode correlated with its absorption spectrum under visible-light irradiation.[20] Direct evidence of the hot electron injection process was later provided by Furube et al. using femtosecond transient absorption spectroscopy, observing a 40% yield of hot electrons transferred from Au nanoparticles into TiO_2.[105]

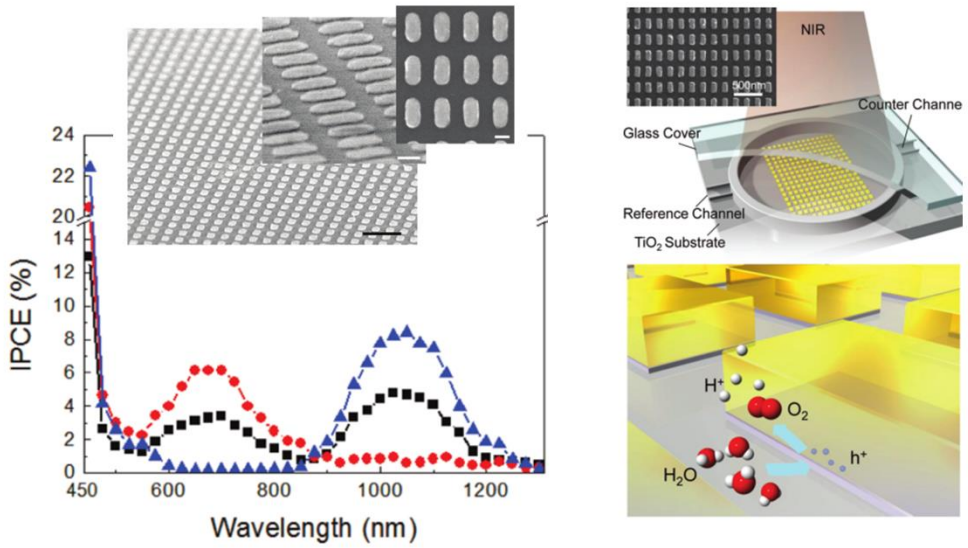

Figure 1.13 Plasmon-induced photocurrent generation and water oxidation using visible to infrared light irradiation.[30, 31]

In 2010, our group further confirmed plasmon-induced charge separation by observing photocurrent generation in Au nanorods loaded on a single crystal TiO_2 under visible to near-infrared light, driven by efficient water oxidation (Figure 1.13).[30] We also successfully utilized a strontium titanate ($SrTiO_3$) single crystal substrate as both an anode and cathode for O_2 and H_2 evolution (Figure 1.14). By setting the pH at the O_2-generating side to 13 and the H_2-generating side to 1, while varying the pH of the opposite side, the researchers observed the pH at which H_2 and O_2 evolution began. The minimum chemical bias of this system was achieved at a relatively low value due to the plasmonic effect, suggesting the feasibility of a low-energy consumption approach for artificial photosynthesis. [106]

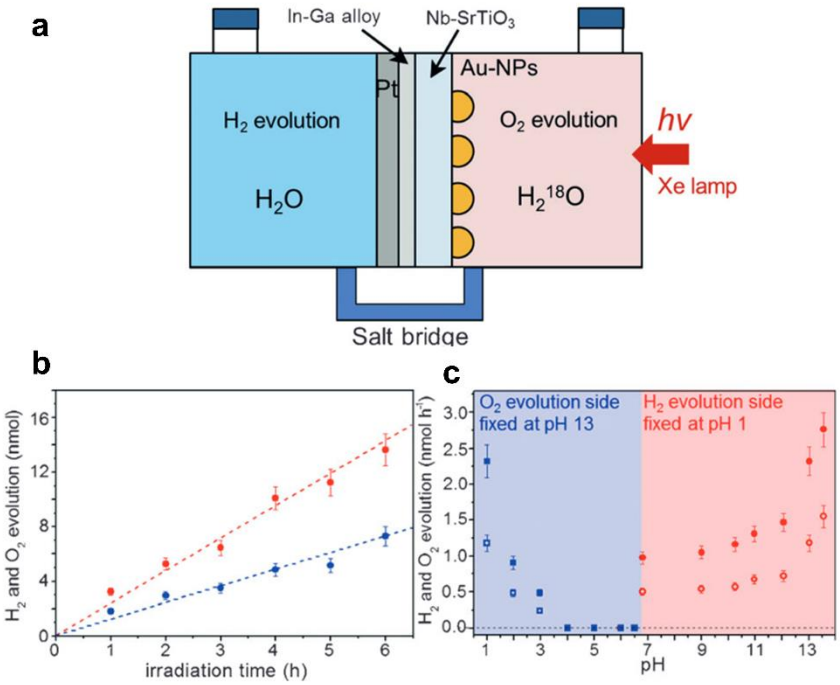

Figure 1.14 (a) Schematic illustration of plasmon-induced water-splitting system using two sides of the same $SrTiO_3$ substrate. (b) Relationship between the gas generation rate and irradiation time. (c) The relationship between gas generation rate and PH value. Points in red indicate H_2 evolution, while the points in blue indicate O_2 evolution.[106]

The development of effective cocatalysts for H_2 and O_2 evolution is essential to improve water splitting efficiency.[107] Adequate loading of semiconductors with cocatalysts significantly boosts their performance. Okazaki et al. demonstrated that site-selective deposition of nanosized CoO_x as a water oxidation cocatalyst at the edges of Au NPs on TiO_2 films enhances photoelectrochemical water oxidation activity.[108] The CoO_x was deposited via a photo-assisted electrochemical method onto the Au/TiO_2 thin film, which under visible light, showed a stable photoanodic current approximately 3 times higher than that obtained from Au/TiO_2 alone (Figure 1.15).

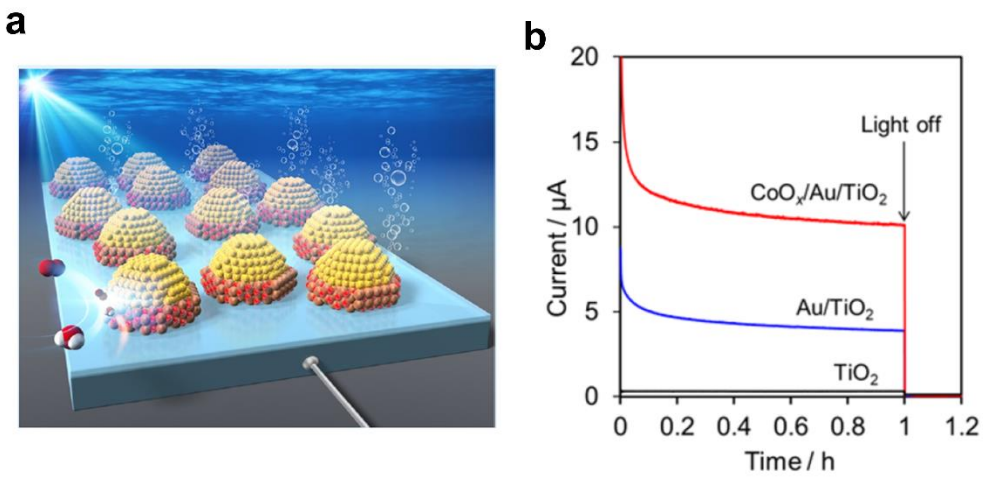

Figure 1.15 (a) Schematic illustration of the $CoO_x/Au/TiO_2$ electrode designed for the OER. (b) Photocurrent generation on $CoO_x/Au/TiO_2$ (red line), Au/TiO_2 (blue line), and bare TiO_2 (black line) electrodes.[108]

1.5.3 Enhancement of water oxidation under modal strong coupling

Plasmon-induced hot electron transfer has emerged as a promising mechanism for solar energy conversion. However, a single layer of metal nanoparticles on a semiconductor, as discussed in 1.5.2, is not sufficient for efficient light harvesting. To address this limitation, our group recently developed a novel photoanode that utilizes strong coupling between LSPR and Fabry-Pérot (F-P) nanocavities to improve plasmonic water splitting. As shown in Figure 1.16, this photoanode, composed of Au NPs on a TiO_2 substrate with an Au film (ATA), exhibits strong coupling when the resonant wavelengths of the nanocavity align closely with the LSPR of the Au NPs. Under strong coupling, hybrid states are formed at both shorter and longer wavelengths, expanding the absorption spectrum and leading to enhanced light absorption. As a result, the quantum yield of photocurrent generation for water oxidation is 1.5 times higher than that of the Au NP/TiO_2 photoanode without strong coupling.[34]

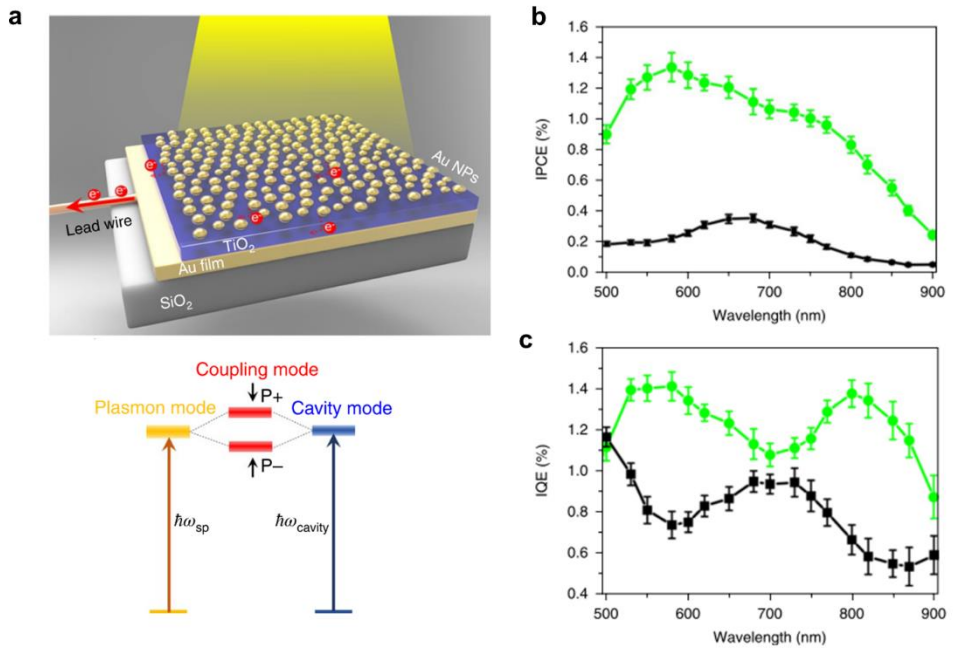

Figure 1.16 (a) A schematic diagram of the ATA photoelectrode and the energy levels associated with the modal strong coupling between the LSPR mode and the F-P cavity mode in the ATA structure. (b) IPCE action spectra and (c) IQE spectra of the ATA (green) and Au NPs/TiO_2 (black) photoelectrodes.[34]

To further enhance the quantum yield of water oxidation, Au-Ag alloy nanoparticles (NPs) with high oscillator strength and strong resistance to oxidation reactions were employed to construct a photoanode under ultrastrong coupling conditions for efficient photochemical water splitting.[36] This photoanode demonstrated a maximum incident photon-to-current efficiency (IPCE) of 4.0%, with the internal quantum efficiency (IQE) reaching 4.1% (Figure 1.17). Additionally, the electron injection enhancement mechanism under strong coupling was studied using Au nanodisks (Au NDs)/TiO_2/Au film, in which Au NDs shape was precisely controlled through electron beam lithography, as opposed to Au NPs (Figure 1.18). Upon photoexcitation, quantum coherence among multiple Au NDs through the F-P nanocavity significantly enhanced the quantum efficiency of hot electron injection into TiO_2.[109] This improvement in the quantum yield of photoelectron transfer at the Au NDs/TiO_2 interface during the initial reaction stages is crucial for optimizing the efficiency of plasmon-induced photochemical reactions. Furthermore, we also successfully applied the quantum coherence of strong coupling photoelectrode to surface enhanced Raman scattering

(SERS), obtaining high-sensitivity and spatially uniform SERS signals.[110-112]

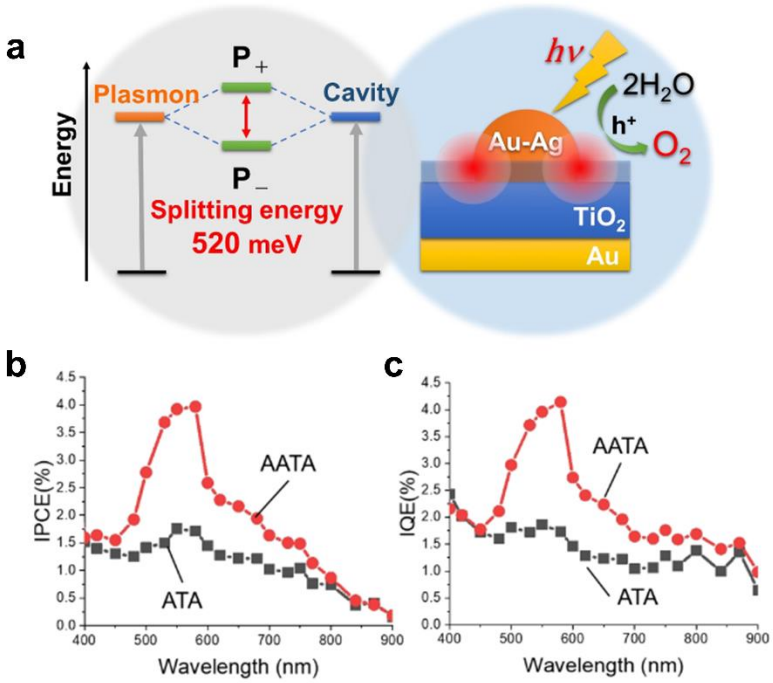

Figure 1.17 A schematic diagram of the AATA photoelectrode and the energy levels associated with the modal strong coupling between the LSPR mode and the F-P cavity mode in the ATA structure. (b) IPCE action spectra and (c) IQE spectra of the AATA [70] and ATA (black) photoelectrodes.[36]

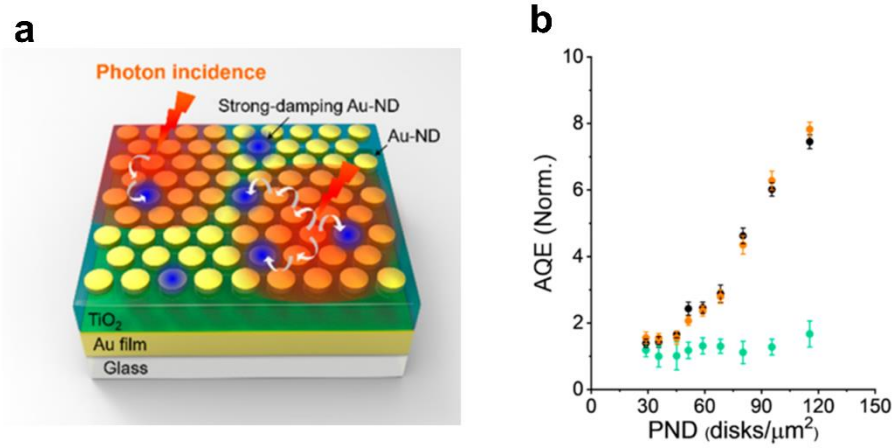

Figure 1.18 (a) Schematic diagram of the strong coupling Au NDs/TiO_2/Au film structure. (b) The apparent quantum efficiency of the hot electron injection from Au NDs to the CB of TiO_2 with various particle number densities (PND) of the Au NDs under modal strong coupling conditions.[109]

1.6 Overview of thesis

This thesis describes the design, fabrication, and characterization of plasmon-induced electron injection under modal strong coupling conditions, achieved through interfacial modulation, alongside an in-depth investigation the mechanism of plasmon-induced water oxidation enhancement under strong coupling conditions. Specifically, this work emphasizes: (a) the near field properties of Au NDs/Ti/TiO_2/Au film photoelectrodes after Au NDs/TiO_2 interface modulation using titanium (Ti) film, (b) the enhancement of electron injection into TiO_2 achieved through interfacial modification using an optimized Ti film thickness, and c) an in-depth investigation of kinetics of water oxidation process under strong coupling condition. Chapter 2 details the fabrication of strong coupling ATTA photoelectrodes with varying thicknesses of Ti film and investigates the effect of Ti film thickness on the near-field properties of ATTA using photoemission electron microscopy (PEEM). Chapter 3 discusses the enhancement of electron injection into TiO_2 under strong coupling conditions facilitated by a Ti film-induced energy transfer at the Au/ TiO_2 interface. The effect of Ti film thickness on the apparent quantum efficiency (AQE) of electron injection into TiO_2 is explored, showing an ~1.8-fold increase in AQE as the Ti film thickness is increased from 0.5 to 5.0 nm. In Chapter 4, a strong coupling Au NPs/TiO_2/Au film photoelectrode, where Au NPs are formed through annealing, is fabricated to study the activation energy of electron-hole recombination ($E_a(r)$) in TiO_2 and the generation of water oxidation intermediates ($E_a(1)$). The smaller $E_a(r)$ suggests that the injected electrons are primarily trapped in shallow trap-sites in TiO_2. Additionally, the activation energy for incident photon-to-current efficiency ($E_a(IPCE)$) is calculated to estimate $E_a(1)$. From this analysis, analysis of the activation energy for water oxidation intermediate generation revealed the potential electrochemical level of holes trapped at the surface states of the Au/TiO_2 interface. Chapter 5 concludes the thesis by summarizing the key findings and insights, discussing their broader implications, and offering a comprehensive conclusion based on the research outcomes.

1.7 References

[1] Davis, S. J.; Lewis, N. S.; Shaner, M.; Aggarwal, S.; Arent, D.; Azevedo, I. L.; Benson, S. M.; Bradley, T.; Brouwer, J.; Chiang, Y.-M. Net-zero emissions energy systems. *Science* **2018**, *360*, eaas9793.

[2] Rogelj, J.; Schaeffer, M.; Meinshausen, M.; Knutti, R.; Alcamo, J.; Riahi, K.; Hare, W. Zero emission targets as long-term global goals for climate protection. *Environ. Res. Lett.* **2015**, *10*, 105007.

[3] Kannan, N.; Vakeesan, D. Solar energy for future world: - A review. *Renew. Sustain. Energy Rev.* **2016**, *62*, 1092-1105.

[4] Parida, B.; Iniyan, S.; Goic, R. A review of solar photovoltaic technologies. *Renew. Sustain. Energy Rev.* **2011**, *15*, 1625-1636.

[5] Izumi, Y. Recent advances in the photocatalytic conversion of carbon dioxide to fuels with water and/or hydrogen using solar energy and beyond. *Coord. Chem. Rev.* **2013**, *257*, 171-186.

[6] Takata, T.; Tanaka, A.; Hara, M.; Kondo, J. N.; Domen, K. Recent progress of photocatalysts for overall water splitting. *Catal. Today* **1998**, *44*, 17-26.

[7] Kudo, A.; Miseki, Y. Heterogeneous photocatalyst materials for water splitting. *Chem. Soc. Rev.* **2009**, *38*, 253-278.

[8] Fujishima, A.; Honda, K. Electrochemical photolysis of water at a semiconductor electrode. *Nature* **1972**, *238*, 37-38.

[9] Bard, A. J.; Fox, M. A. Artificial photosynthesis: solar splitting of water to hydrogen and oxygen. *Acc. Chem. Res.* **1995**, *28*, 141-145.

[10] Crampton, K. T.; Joly, A. G.; El-Khoury, P. Z. Direct Visualization of Counter-Propagating Surface Plasmons in Real Space-Time. *J. Phys. Chem. Lett.* **2019**, *10*, 5694-5699.

[11] Bendavid, A.; Martin, P. J.; Jamting, Å.; Takikawa, H. Structural and optical properties of titanium oxide thin films deposited by filtered arc deposition. *Thin Solid Films* **1999**, *355*, 6-11.

[12] Linic, S.; Christopher, P.; Ingram, D. B. Plasmonic-metal nanostructures for efficient conversion of solar to chemical energy. *Nat. Mater.* **2011**, *10*, 911-921.

[13] Wang, Q.; Domen, K. Particulate photocatalysts for light-driven water splitting: mechanisms, challenges, and design strategies. *Chem. Rev.* **2019**, *120*, 919-985.

[14] Subramanian, V.; Wolf, E.; Kamat, P. V. Semiconductor-metal composite

nanostructures. To what extent do metal nanoparticles improve the photocatalytic activity of TiO_2 films? *J. Phys. Chem. B* **2001**, *105*, 11439-11446.

[15] Subramanian, V.; Wolf, E. E.; Kamat, P. V. Catalysis with TiO_2/gold nanocomposites. Effect of metal particle size on the Fermi level equilibration. *J. Am. Chem. Soc.* **2004**, *126*, 4943-4950.

[16] Gomes Silva, C.; Juárez, R.; Marino, T.; Molinari, R.; García, H. Influence of excitation wavelength (UV or visible light) on the photocatalytic activity of titania containing gold nanoparticles for the generation of hydrogen or oxygen from water. *J. Am. Chem. Soc.* **2011**, *133*, 595-602.

[17] Arabatzis, I.; Stergiopoulos, T.; Bernard, M. C.; Labou, D.; Neophytides, S.; Falaras, P. Silver-modified titanium dioxide thin films for efficient photodegradation of methyl orange. *Appl. Catal. B Environ.* **2003**, *42*, 187-201.

[18] Ingram, D. B.; Linic, S. Water splitting on composite plasmonic-metal/semiconductor photoelectrodes: evidence for selective plasmon-induced formation of charge carriers near the semiconductor surface. *J. Am. Chem. Soc.* **2011**, *133*, 5202-5205.

[19] Kamat, P. V. Photophysical, photochemical and photocatalytic aspects of metal nanoparticles. ACS Publications: 2002; Vol. 106, pp 7729-7744.

[20] Tian, Y.; Tatsuma, T. Mechanisms and applications of plasmon-induced charge separation at TiO_2 films loaded with gold nanoparticles. *J. Am. Chem. Soc.* **2005**, *127*, 7632-7637.

[21] Kowalska, E.; Abe, R.; Ohtani, B. Visible light-induced photocatalytic reaction of gold-modified titanium (IV) oxide particles: action spectrum analysis. *Chem.Commun.* **2009**, 241-243.

[22] Kowalska, E.; Mahaney, O. O. P.; Abe, R.; Ohtani, B. Visible-light-induced photocatalysis through surface plasmon excitation of gold on titania surfaces. *Phys. Chem. Chem. Phys.* **2010**, *12*, 2344-2355.

[23] Tian, Y.; Tatsuma, T. Plasmon-induced photoelectrochemistry at metal nanoparticles supported on nanoporous TiO_2. *Chem. Commun.* **2004**, 1810-1811.

[24] Thimsen, E.; Le Formal, F.; Gratzel, M.; Warren, S. C. Influence of plasmonic Au nanoparticles on the photoactivity of Fe_2O_3 electrodes for water splitting. *Nano Lett.* **2011**, *11*, 35-43.

[25] Liu, Z.; Hou, W.; Pavaskar, P.; Aykol, M.; Cronin, S. B. Plasmon resonant enhancement of photocatalytic water splitting under visible illumination. *Nano Lett.* **2011**, *11*, 1111-1116.

[26] Jiang, R.; Li, B.; Fang, C.; Wang, J. Metal/semiconductor hybrid nanostructures for plasmon‐enhanced applications. *Adv. Mater.* **2014**, *26*, 5274-5309.

[27] Grätzel, M. Photoelectrochemical cells. *Nature* **2001**, *414*, 338-344.

[28] Goldberger, J.; He, R.; Zhang, Y.; Lee, S.; Yan, H.; Choi, H.-J.; Yang, P. Single-crystal gallium nitride nanotubes. *Nature* **2003**, *422*, 599-602.

[29] Ueno, K.; Oshikiri, T.; Sun, Q.; Shi, X.; Misawa, H. Solid-state plasmonic solar cells. *Chem. Rev.* **2017**, *118*, 2955-2993.

[30] Nishijima, Y.; Ueno, K.; Yokota, Y.; Murakoshi, K.; Misawa, H. Plasmon-assisted photocurrent generation from visible to near-infrared wavelength using a Au-nanorods/TiO_2 electrode. *J. phys. chem. lett.* **2010**, *1*, 2031-2036.

[31] Nishijima, Y.; Ueno, K.; Kotake, Y.; Murakoshi, K.; Inoue, H.; Misawa, H. Near-infrared plasmon-assisted water oxidation. *J. phys. chem. lett.* **2012**, *3*, 1248-1252.

[32] Shi, X.; Ueno, K.; Takabayashi, N.; Misawa, H. Plasmon-enhanced photocurrent generation and water oxidation with a gold nanoisland-loaded titanium dioxide photoelectrode. *J. Phys. Chem. C* **2013**, *117*, 2494-2499.

[33] Shi, X.; Ueno, K.; Oshikiri, T.; Misawa, H. Improvement of plasmon-enhanced photocurrent generation by interference of TiO_2 thin film. *J. Phys. Chem. C* **2013**, *117*, 24733-24739.

[34] Shi, X.; Ueno, K.; Oshikiri, T.; Sun, Q.; Sasaki, K.; Misawa, H. Enhanced water splitting under modal strong coupling conditions. *Nat. Nanotechnol.* **2018**, *13*, 953-958.

[35] Cao, Y.; Oshikiri, T.; Shi, X.; Ueno, K.; Li, J.; Misawa, H. Efficient Hot‐Electron Transfer under Modal Strong Coupling Conditions with Sacrificial Electron Donors. *ChemNanoMat* **2019**, *5*, 1008-1014.

[36] Suganami, Y.; Oshikiri, T.; Shi, X.; Misawa, H. Water oxidation under modal ultrastrong coupling conditions using gold/silver alloy nanoparticles and Fabry–Pérot nanocavities. *Angew. Chem. Int. Ed.* **2021**, *60*, 18438-18442.

[37] Kauranen, M.; Zayats, A. V. Nonlinear plasmonics. *Nat. Photonics* **2012**, *6*, 737-748.

[38] Liu, Q.; Romero‐Gomez, P.; Mantilla‐Perez, P.; Colodrero, S.; Toudert, J.; Martorell, J. A Two‐Resonance Tapping Cavity for an Optimal Light Trapping in Thin‐Film Solar Cells. *Adv. Energy Mater.* **2017**, *7*, 1700356.

[39] Aslam, U.; Rao, V. G.; Chavez, S.; Linic, S. Catalytic conversion of solar to

chemical energy on plasmonic metal nanostructures. *Nat. Catal.* **2018**, *1*, 656-665.

[40] Xu, Y.; Bai, P.; Zhou, X.; Akimov, Y.; Png, C. E.; Ang, L. K.; Knoll, W.; Wu, L. Optical refractive index sensors with plasmonic and photonic structures: promising and inconvenient truth. *Adv. Opt. Mater.* **2019**, *7*, 1801433.

[41] Adato, R.; Guo, J. Modification of dispersion, localization, and attenuation of thin metal stripe symmetric surface plasmon-polariton modes by thin dielectric layers. *J. Appl. Phys.* **2009**, *105*.

[42] Zayats, A. V. Perspective: A glint of the future. *Nature* **2013**, *495*, S7-S7.

[43] Butun, S.; Tongay, S.; Aydin, K. Enhanced light emission from large-area monolayer MoS_2 using plasmonic nanodisc arrays. *Nano Lett.* **2015**, *15*, 2700-2704.

[44] Barnes, W. L.; Dereux, A.; Ebbesen, T. W. Surface plasmon subwavelength optics. *Nature* **2003**, *424*, 824-830.

[45] Schuller, J. A.; Barnard, E. S.; Cai, W.; Jun, Y. C.; White, J. S.; Brongersma, M. L. Plasmonics for extreme light concentration and manipulation. *Nat. Mater.* **2010**, *9*, 193-204.

[46] Shalaev, V. M. Optical negative-index metamaterials. *Nat. Photonics* **2007**, *1*, 41-48.

[47] Yao, K.; Liu, Y. Plasmonic metamaterials. *Nanotech. Rev.* **2014**, *3*, 177-210.

[48] Alù, A.; Engheta, N. Cloaking a receiving antenna or a sensor with plasmonic metamaterials. *Metamaterials* **2010**, *4*, 153-159.

[49] Park, I.-Y.; Kim, S.; Choi, J.; Lee, D.-H.; Kim, Y.-J.; Kling, M. F.; Stockman, M. I.; Kim, S.-W. Plasmonic generation of ultrashort extreme-ultraviolet light pulses. *Nat. Photonics* **2011**, *5*, 677-681.

[50] Li, W.; Valentine, J. Metamaterial perfect absorber based hot electron photodetection. *Nano Lett.* **2014**, *14*, 3510-3514.

[51] Sobhani, A.; Knight, M. W.; Wang, Y.; Zheng, B.; King, N. S.; Brown, L. V.; Fang, Z.; Nordlander, P.; Halas, N. J. Narrowband photodetection in the near-infrared with a plasmon-induced hot electron device. *Nat. Commun.* **2013**, *4*, 1643.

[52] Pillai, S. a.; Green, M. Plasmonics for photovoltaic applications. *Sol. Energy Mater. Sol. cells* **2010**, *94*, 1481-1486.

[53] Atwater, H. A.; Polman, A. Plasmonics for improved photovoltaic devices. *Nat.*

Mater. **2010**, *9*, 205-213.

[54] Anker, J. N.; Hall, W. P.; Lyandres, O.; Shah, N. C.; Zhao, J.; Van Duyne, R. P. Biosensing with plasmonic nanosensors. *Nat. Mater.* **2008**, *7*, 442-453.

[55] Han, X.; Liu, K.; Sun, C. Plasmonics for biosensing. *Materials* **2019**, *12*, 1411.

[56] Willets, K. A.; Van Duyne, R. P. Localized surface plasmon resonance spectroscopy and sensing. *Annu. Rev. Phys. Chem.* **2007**, *58*, 267-297.

[57] Gao, S.; Ueno, K.; Misawa, H. Plasmonic antenna effects on photochemical reactions. *Acc. Chem. Res.* **2011**, *44*, 251-260.

[58] Tan, T.; Tian, C.; Ren, Z.; Yang, J.; Chen, Y.; Sun, L.; Li, Z.; Wu, A.; Yin, J.; Fu, H. LSPR-dependent SERS performance of silver nanoplates with highly stable and broad tunable LSPRs prepared through an improved seed-mediated strategy. *Phys. Chem. Chem. Phys.* **2013**, *15*, 21034-21042.

[59] Cao, J.; Sun, T.; Grattan, K. T. Gold nanorod-based localized surface plasmon resonance biosensors: A review. *Sens. Actuators B: Chem.* **2014**, *195*, 332-351.

[60] Freestone, I.; Meeks, N.; Sax, M.; Higgitt, C. The Lycurgus cup—a roman nanotechnology. *Gold bulletin* **2007**, *40*, 270-277.

[61] Zhang, X.; Chen, Y. L.; Liu, R.-S.; Tsai, D. P. Plasmonic photocatalysis. *Rep. Prog. Phys.* **2013**, *76*, 046401.

[62] Jain, P. K.; Lee, K. S.; El-Sayed, I. H.; El-Sayed, M. A. Calculated absorption and scattering properties of gold nanoparticles of different size, shape, and composition: applications in biological imaging and biomedicine. *J. Phys. Chem. B* **2006**, *110*, 7238-7248.

[63] Mock, J.; Barbic, M.; Smith, D.; Schultz, D.; Schultz, S. Shape effects in plasmon resonance of individual colloidal silver nanoparticles. *J. Chem. Phys.* **2002**, *116*, 6755-6759.

[64] Link, S.; Wang, Z. L.; El-Sayed, M. Alloy formation of gold− silver nanoparticles and the dependence of the plasmon absorption on their composition. *J. Phys. Chem. B* **1999**, *103*, 3529-3533.

[65] Schuck, P. J. Hot electrons go through the barrier. *Nat. Nanotechnol.* **2013**, *8*, 799-800.

[66] Lee, H.; Park, Y.; Song, K.; Park, J. Y. Surface plasmon-induced hot carriers: generation, detection, and applications. *Acc. Chem. Res.* **2022**, *55*, 3727-3737.

[67] Li, X.; Xiao, D.; Zhang, Z. Landau damping of quantum plasmons in metal nanostructures. *New J. Phys.* **2013**, *15*, 023011.

[68] Sönnichsen, C.; Franzl, T.; Wilk, T.; von Plessen, G.; Feldmann, J.; Wilson, O.; Mulvaney, P. Drastic reduction of plasmon damping in gold nanorods. *Phys. Rev. Lett.* **2002**, *88*, 077402.

[69] Brongersma, M. L.; Halas, N. J.; Nordlander, P. Plasmon-induced hot carrier science and technology. *Nat Nanotechnol* **2015**, *10*, 25-34.

[70] Hanke, T.; Krauss, G.; Träutlein, D.; Wild, B.; Bratschitsch, R.; Leitenstorfer, A. Efficient nonlinear light emission of single gold optical antennas driven by few-cycle near-infrared pulses. *Phys. Rev. Lett.* **2009**, *103*, 257404.

[71] Hogan, N. J.; Urban, A. S.; Ayala-Orozco, C.; Pimpinelli, A.; Nordlander, P.; Halas, N. J. Nanoparticles heat through light localization. *Nano Lett.* **2014**, *14*, 4640-4645.

[72] Mokari, T.; Rothenberg, E.; Popov, I.; Costi, R.; Banin, U. Selective growth of metal tips onto semiconductor quantum rods and tetrapods. *Science* **2004**, *304*, 1787-1790.

[73] Menagen, G.; Macdonald, J. E.; Shemesh, Y.; Popov, I.; Banin, U. Au growth on semiconductor nanorods: photoinduced versus thermal growth mechanisms. *J. Am. Chem. Soc.* **2009**, *131*, 17406-17411.

[74] Wu, K.; Rodríguez-Córdoba, W. E.; Yang, Y.; Lian, T. Plasmon-induced hot electron transfer from the Au tip to CdS rod in CdS-Au nanoheterostructures. *Nano Lett.* **2013**, *13*, 5255-5263.

[75] Leenheer, A. J.; Narang, P.; Lewis, N. S.; Atwater, H. A. Solar energy conversion via hot electron internal photoemission in metallic nanostructures: efficiency estimates. *J. Appl. Phys.* **2014**, *115*.

[76] Link, S.; El-Sayed, M. A. Spectral properties and relaxation dynamics of surface plasmon electronic oscillations in gold and silver nanodots and nanorods. ACS Publications: 1999; Vol. 103, pp 8410-8426.

[77] Wu, K.; Chen, J.; McBride, J. R.; Lian, T. Efficient hot-electron transfer by a plasmon-induced interfacial charge-transfer transition. *Science* **2015**, *349*, 632-635.

[78] Cushing, S. K.; Li, J.; Meng, F.; Senty, T. R.; Suri, S.; Zhi, M.; Li, M.; Bristow, A. D.; Wu, N. Photocatalytic activity enhanced by plasmonic resonant energy transfer from metal to semiconductor. *J. Am. Chem. Soc.* **2012**, *134*, 15033-15041.

[79] Li, J.; Cushing, S. K.; Meng, F.; Senty, T. R.; Bristow, A. D.; Wu, N. Plasmon-induced resonance energy transfer for solar energy conversion. *Nat. Photonics* **2015**, *9*, 601-607.

[80] Oener, S. Z.; van de Groep, J.; Macco, B.; Bronsveld, P. C.; Kessels, W.; Polman, A.; Garnett, E. C. Metal–insulator–semiconductor nanowire network solar cells. *Nano Lett.* **2016**, *16*, 3689-3695.

[81] Liu, G.; Lou, Y.; Zhao, Y.; Burda, C. Directional damping of plasmons at metal–semiconductor interfaces. *Acc. Chem. Res.* **2022**, *55*, 1845-1856.

[82] Li, H.; Wang, S.; Wang, M.; Gao, Y.; Tang, J.; Zhao, S.; Chi, H.; Zhang, P.; Qu, J.; Fan, F. Enhancement of Plasmon‐Induced Photoelectrocatalytic Water Oxidation over Au/TiO_2 with Lithium Intercalation. *Angew. Chem. Int. Ed.* **2022**, *134*, e202204272.

[83] Wu, B.-H.; Liu, W.-T.; Chen, T.-Y.; Perng, T.-P.; Huang, J.-H.; Chen, L.-J. Plasmon-enhanced photocatalytic hydrogen production on Au/TiO_2 hybrid nanocrystal arrays. *Nano Energy* **2016**, *27*, 412-419.

[84] Shi, X.; Li, X.; Toda, T.; Oshikiri, T.; Ueno, K.; Suzuki, K.; Murakoshi, K.; Misawa, H. Interfacial structure-modulated plasmon-induced water oxidation on strontium titanate. *ACS Appl. Energy Mater.* **2020**, *3*, 5675-5683.

[85] Zheng, B. Y.; Zhao, H.; Manjavacas, A.; McClain, M.; Nordlander, P.; Halas, N. J. Distinguishing between plasmon-induced and photoexcited carriers in a device geometry. *Nat. Commun.* **2015**, *6*, 7797.

[86] Knight, M. W.; Sobhani, H.; Nordlander, P.; Halas, N. J. Photodetection with active optical antennas. *Science* **2011**, *332*, 702-704.

[87] Green, M. A. Recent developments in photovoltaics. *Sol. Energy* **2004**, *76*, 3-8.

[88] Westphalen, M.; Kreibig, U.; Rostalski, J.; Lüth, H.; Meissner, D. Metal cluster enhanced organic solar cells. *Sol. Energy Mater. Sol. cells* **2000**, *61*, 97-105.

[89] Soller, B. J.; Hall, D. G. Dynamic modifications to the plasmon resonance of a metallic nanoparticle coupled to a planar waveguide: beyond the point-dipole limit. *JOSA B* **2002**, *19*, 1195-1203.

[90] Schaadt, D.; Feng, B.; Yu, E. Enhanced semiconductor optical absorption via surface plasmon excitation in metal nanoparticles. *Appl. Phys. Lett.* **2005**, *86*.

[91] Derkacs, D.; Lim, S.; Matheu, P.; Mar, W.; Yu, E. Improved performance of amorphous silicon solar cells via scattering from surface plasmon polaritons in nearby metallic nanoparticles. *Appl. Phys. Lett.* **2006**, *89*.

[92] Pillai, S.; Catchpole, K.; Trupke, T.; Green, M. Surface plasmon enhanced silicon solar cells. *J. Appl. phys.* **2007**, *101*.

[93] Catchpole, K.; Polman, A. Design principles for particle plasmon enhanced

solar cells. *Appl. Phys. Lett.* **2008**, *93*.

[94] Nakayama, K.; Tanabe, K.; Atwater, H. A. Plasmonic nanoparticle enhanced light absorption in GaAs solar cells. *Appl. Phys. Lett.* **2008**, *93*.

[95] Shin, H.; Yanik, M. F.; Fan, S.; Zia, R.; Brongersma, M. L. Omnidirectional resonance in a metal–dielectric–metal geometry. *Appl. Phys. Lett.* **2004**, *84*, 4421-4423.

[96] Zeman, M.; Krc, J. Optical and electrical modeling of thin-film silicon solar cells. *J. Mater. Res.* **2008**, *23*, 889-898.

[97] Burgelman, M.; Verschraegen, J.; Degrave, S.; Nollet, P. Modeling thin‐film PV devices. *Prog. Photovolt: Res. Appl.* **2004**, *12*, 143-153.

[98] Ong, K. G.; Varghese, O. K.; Mor, G. K.; Shankar, K.; Grimes, C. A. Application of finite-difference time domain to dye-sensitized solar cells: The effect of nanotube-array negative electrode dimensions on light absorption. *Sol. Energy Mater. Sol. cells* **2007**, *91*, 250-257.

[99] Chen, X.; Mao, S. S. Titanium dioxide nanomaterials: synthesis, properties, modifications, and applications. *Chem. Rev.* **2007**, *107*, 2891-2959.

[100] Lin, Y.; Yuan, G.; Sheehan, S.; Zhou, S.; Wang, D. Hematite-based solar water splitting: challenges and opportunities. *EES* **2011**, *4*, 4862-4869.

[101] Jin, R.; Cao, Y.; Mirkin, C. A.; Kelly, K. L.; Schatz, G. C.; Zheng, J. Photoinduced conversion of silver nanospheres to nanoprisms. *Science* **2001**, *294*, 1901-1903.

[102] Ueno, K.; Misawa, H. Surface plasmon-enhanced photochemical reactions. *J. Photochem. Photobiol. C: Photochem. Rev.* **2013**, *15*, 31-52.

[103] Ueno, K.; Oshikiri, T.; Misawa, H. Plasmon‐induced water splitting using metallic-nanoparticle-loaded photocatalysts and photoelectrodes. *ChemPhysChem* **2016**, *17*, 199-215.

[104] Zhao, G.; Kozuka, H.; Yoko, T. Sol—gel preparation and photoelectrochemical properties of TiO_2 films containing Au and Ag metal particles. *Thin solid films* **1996**, *277*, 147-154.

[105] Furube, A.; Du, L.; Hara, K.; Katoh, R.; Tachiya, M. Ultrafast plasmon-induced electron transfer from gold nanodots into TiO2 nanoparticles. *J. Am. Chem. Soc.* **2007**, *129*, 14852-14853.

[106] Zhong, Y.; Ueno, K.; Mori, Y.; Shi, X.; Oshikiri, T.; Murakoshi, K.; Inoue, H.; Misawa, H. Plasmon‐assisted water splitting using two sides of the same

$SrTiO_3$ single‐crystal substrate: conversion of visible light to chemical energy. *Angew. Chem. Int. Ed. Engl.* **2014**, *53*, 10350-10354.

[107] Zhong, Y.; Ueno, K.; Mori, Y.; Oshikiri, T.; Misawa, H. Cocatalyst effects on hydrogen evolution in a plasmon-induced water-splitting system. *J. Phys. Chem. C* **2015**, *119*, 8889-8897.

[108] Okazaki, M.; Suganami, Y.; Hirayama, N.; Nakata, H.; Oshikiri, T.; Yokoi, T.; Misawa, H.; Maeda, K. Site-selective deposition of a cobalt cocatalyst onto a plasmonic Au/TiO_2 photoanode for improved water oxidation. *ACS Appl. Energy Mater.* **2020**, *3*, 5142-5146.

[109] Liu, Y.-E.; Shi, X.; Yokoyama, T.; Inoue, S.; Sunaba, Y.; Oshikiri, T.; Sun, Q.; Tamura, M.; Ishihara, H.; Sasaki, K. Quantum-coherence-enhanced hot-electron injection under modal strong coupling. *ACS Nano* **2023**, *17*, 8315-8323.

[110] Suganami, Y.; Oshikiri, T.; Mitomo, H.; Sasaki, K.; Liu, Y.-E.; Shi, X.; Matsuo, Y.; Ijiro, K.; Misawa, H. Spatially Uniform and Quantitative Surface-Enhanced Raman Scattering under Modal Ultrastrong Coupling Beyond Nanostructure Homogeneity Limits. *ACS Nano* **2024**, *18*, 4993-5002.

[111] Zang, X.; Shi, X.; Oshikiri, T.; Ueno, K.; Sunaba, Y.; Sasaki, K.; Misawa, H. Highly sensitive and spatially homogeneous surface-enhanced Raman scattering substrate under plasmon–nanocavity coupling. *J. Phys. Chem. C* **2021**, *125*, 19880-19886.

[112] Zang, X.; Shi, X.; Suganami, Y.; Liu, Y.-E.; Oshikiri, T.; Misawa, H. Investigation of enhanced water oxidation under plasmon–nanocavity strong coupling using in situ electrochemical surface-enhanced Raman spectroscopy. *J. Phys. Chem. C* **2023**, *127*, 15087-15095.

Chapter 2

Near-field properties of Au NDs/Ti/TiO_2/Au film structure under strong coupling conditions

2.1 Introduction

Sustainable energy generation is critical for mitigating future energy crises and relies on innovative breakthroughs in designing cost-effective and efficient systems for energy conversion and storage from renewable sources.[1-5] Among these, solar-to-chemical energy conversion has emerged as one of the most promising approaches to meet such demands.[6] In this context, photocatalysts have garnered significant attention due to their capability to convert solar energy into chemical energy. Metal oxides, particularly titanium dioxide (TiO_2), a wide bandgap semiconductor, have been extensively utilized for these applications.[7, 8] To further improve the performance of TiO_2-based photocatalysts, integrating plasmonic metals such as gold (Au) and silver (Ag) has proven highly effective due to the advantages offered by plasmonic effects. Plasmonic solar water splitting, in particular, holds great potential for providing a sustainable and continuous supply of green energy. A crucial prerequisite for plasmonic water splitting is the efficient separation of photogenerated charge carriers, where interfacial charge transfer plays a pivotal role in enhancing electron-hole separation.[9]

Recently, our group developed an Au nanodisk (Au NDs)/TiO_2/Au film (ATA) photoelectrode under modal strong coupling between localized surface plasmon resonance (LSPR) and Fabry-Pérot (F-P) nanocavity modes. This configuration efficiently harvests incident photons by generating two hybrid states and demonstrated that quantum coherence among Au NDs, mediated through the F-P nanocavity, significantly enhances the apparent quantum efficiency (AQE) of electron injection into the conduction band (CB) of TiO_2.[10] Moreover, titanium (Ti) has been reported to facilitate plasmon-induced electron transfer between Au and silicon.[11] Building on this concept, we investigated the enhancement of electron transfer by incorporating a Ti

film between Au NDs and the TiO_2 layer under strong coupling conditions.

The mechanism of electron transfer at the Au NDs/TiO_2 interface involves hot electrons generated by localized surface plasmon resonance (LSPR) excitation transferring to the conduction band (CB) of TiO_2, while the corresponding holes are captured by surface states of TiO_2 and participate in oxidation reactions. As plasmon-induced hot electron generation is closely linked to the nanoscale localization of the electromagnetic field near the metallic nanostructure,[12] near-field enhancement becomes crucial for photochemical and photocatalytic applications where hot electron transfer plays a significant role.[13, 14]

To further elucidate the impact of Ti film on the near-field properties of strong coupling Au NDs/Ti/ TiO_2/Au film (ATTA) photoelectrodes, detailed investigations are required. Various techniques have been employed to visualize the near-field properties of metallic nanostructures, including scanning photoionization microscopy,[15] scanning near-field optical microscopy,[16, 17] nonlinear photopolymerization,[18] and near-field ablation of substrates[19, 20]. However, these methods are often limited by resolution constraints and potential surface damage, making precise measurements of near-field properties challenging.

Recent advancements in photoemission electron microscopy (PEEM), using femtosecond laser pulses as the excitation source, have demonstrated its efficacy as a powerful tool for mapping the near-field properties of plasmonic metal structures. In this study, nanoscale Ti films were incorporated to modify the Au NDs/TiO_2 interface in the strong coupling ATA structure. The influence of Ti film thickness on the near-field properties of the ATTA photoelectrodes was systematically analyzed using PEEM. Additionally, time-resolved PEEM, which integrates PEEM with pump-probe techniques, was employed to investigate the dephasing time of hybrid modes under varying Ti film thicknesses.

2.2 Experimental details

2.2.1 ATTA structure fabrication

The silica glass (SiO_2) substrate with sizes of $10 \times 10 \times 1.0$ mm^3 was used to fabricate ATTA structure. After rinsing process with acetone, methanol, and ultrapure water in turn for 5 minutes in an ultrasonic bath and then dried with pure nitrogen flow. As shown in Figure 2.1, a 2 nm-thick Ti film and 100 nm-thick Au film were deposited onto SiO_2 substrate with Helicon sputtering (MPS-4000C1/HC1, ULVAC). Subsequently, a TiO_2 film was deposited on the Au reflective film using a commercial atomic layer deposition (ALD) reactor (SUNALE R series, Picosun) at 300°C. The deposition process utilized deionized water vapor and titanium tetrachloride ($TiCl_4$) as precursor sources. To prepare for patterning, the TiO_2 film was spin-coated with a diluted copolymer photoresist (ZEP-520, Zeon Chemicals, mixed with ZEP in a 2:1 ratio) at 1000 rpm for 10 seconds and then at 4000 rpm for 60 seconds. The coated substrate was prebaked on a hot plate at 180°C for 2 minutes to remove residual water from the photoresist. The Au nanodisk (Au NDs) patterns were created using an electron-beam lithography (EBL) system (ELS-F130, Elionix) operating at 130 kV with a working current of 300 pA. After exposure, development was carried out with ZED-N50. Following this, a Ti film and a 30 nm-thick Au film were sequentially deposited via sputtering. Finally, a lift-off process was performed by immersing the sample in anisole, acetone, and ultrapure water in an ultrasonic bath for 5 minutes at each step.

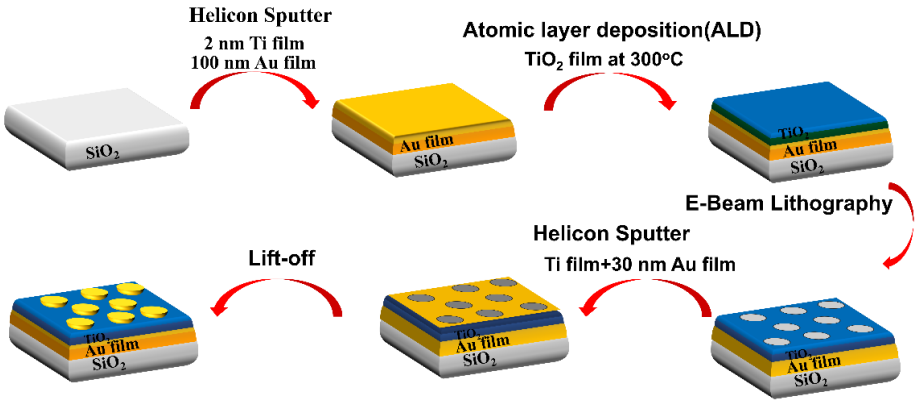

Figure 2.1 The sketch map of the ATTA structure fabrication process.

2.2.2 Optical properties and morphology characterization

A photonic multichannel analyzer (PMA C7473; Hamamatsu Photonics), operating in the wavelength range of 400–900 nm, was used to measure the far-field optical spectra. The morphology of the ATTA structure was characterized using field-emission scanning electron microscopy (FE-SEM, JSM-6700FT, JEOL) with a maximum resolution of 1 nm.

2.2.3 Near-field properties of ATTA

Near-field measurements in this study were conducted using a PEEM microscope (Elmetic GmbH) equipped with two femtosecond laser excitation sources, as illustrated in Figure 2.2. The PEEM system is equipped with an aberration corrector, achieving a spatial resolution down to 4 nm. The sample was placed in the main chamber under an ultrahigh vacuum of up to 10^{-11} Torr. To ensure the efficient collection of emitted electrons, a 20 kV ultrahigh voltage was applied to the system. Typically, the laser pulses were configured to irradiate the sample at either a fixed oblique incidence angle of 74 ◦ or normal incidence. For the present study, only the normal incidence configuration was utilized.

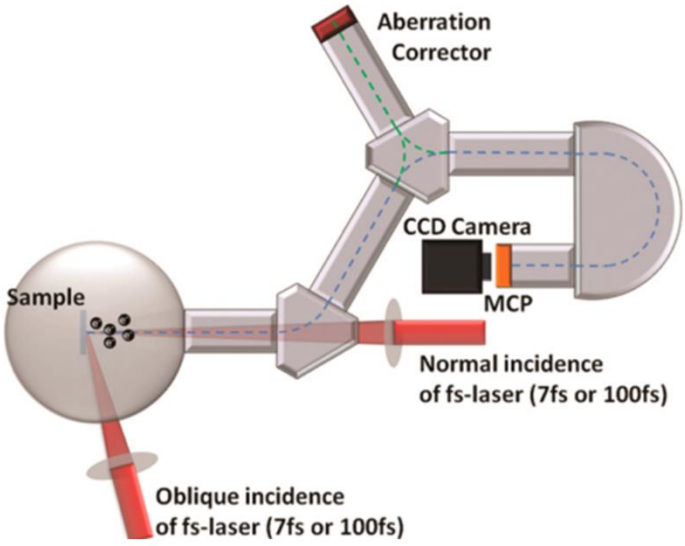

Figure 2.2 The sketch map of our PEEM system.

In the near-field spectra measurements, a femtosecond laser (Mai Tai, Spectra-Physics), delivering approximately 100 fs pulses and coupled with an optical parametric oscillator (OPO) for tunable excitation wavelengths, was employed. The laser beam was focused onto the sample using a lens with a focal length of 600 nm. This setup was utilized for wavelength-dependent PEEM measurements to obtain near-field spectra and to perform near-field mapping at various wavelengths. In plasmonic nanostructures, localized surface plasmon resonance (LSPR) facilitates the generation of significant photoemission (PE) via a nonlinear multiphoton photoemission process, particularly when the laser wavelength coincides with or is close to the absorption peak of the structure. When the ultrafast fs laser, with high peak intensity, irradiates the substrate at wavelengths near the absorption peaks, the near-field enhancement effect significantly promotes the multiphoton photoemission process. Given the nonlinear nature of PE intensity on the sample surface, the resulting PEEM images at different wavelengths can be interpreted as nonlinear near-field intensity maps of the structure. Notably, the near-field PE intensity signal was captured over the entire 30-μm field of view (FOV) in this study. By varying the incident wavelength from 500 to 870 nm in 10 nm increments, a series of PEEM images were obtained. The PE intensity from the full FOV was then integrated and plotted as a function of the incident wavelength, resulting in the near-field photoemission intensity spectra.

2.2.4 Dephasing time of hybrid modes of ATTA

A second femtosecond laser (Rainbow, Femtolasers), delivering 7 fs pulses at a central wavelength of 800 nm and a spectral range of 650–1050 nm, was used for time-resolved photoemission electron microscopy (TR-PEEM) measurements to investigate the dephasing time of hybrid modes in ATTA systems. As illustrated in Figure 2.3, the laser beam passed through a Mach-Zehnder interferometer to generate phase-correlated pump and probe pulses. The interferometer divides the laser beam into two identical pulses, with the critical aspect being the control of the delay time between them. This delay allows for the generation of the pump and probe pulses, which are then focused onto the sample. By adjusting the delay time between the pulses, a series of PEEM

images were recorded, with a frame interval of approximately ~ 0.7 fs (π/2 rad relative to the 800 nm carrier wave of the laser pulse).

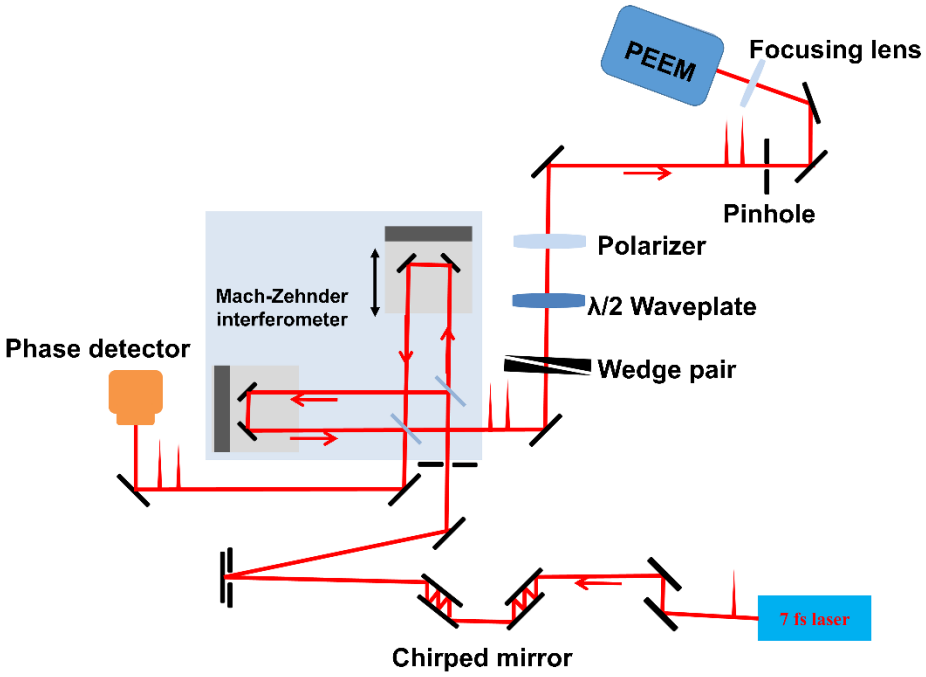

Figure 2.3 Schematic of TR-PEEM setup.

The principle behind determining the dephasing time of hybrid modes in the ATTA structure using TR-PEEM is illustrated in Figure 2.4. When the plasmon field of the Au NDs are excited by the pump pulse, the plasmon oscillates at its characteristic frequency. Upon introducing the probe pulse with a controlled delay, it can also excite the plasmon oscillation. The two plasmon fields, excited by the pump and probe pulses, can interfere with each other in two primary ways. If the plasmon oscillations from both pulses are in phase, constructive interference occurs, leading to electron excitation and subsequent detection by the PEEM. Conversely, if the plasmon oscillations are out of phase, destructive interference takes place, resulting in no electron emission. By varying the delay time between the pump and probe pulses, the oscillatory behavior of the hot spots can be observed.

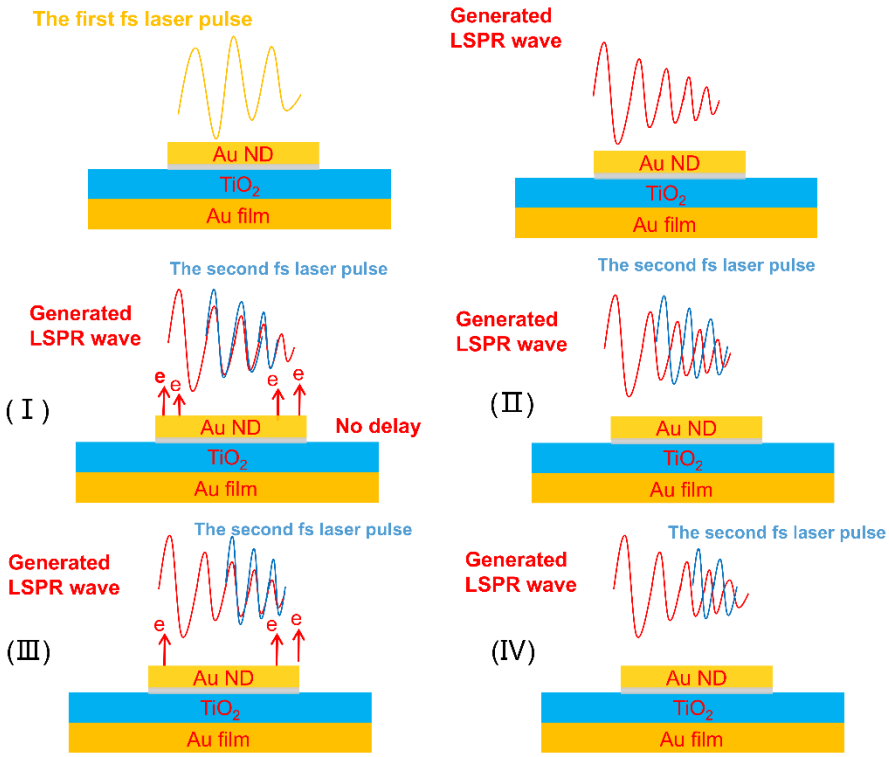

Figure 2.4. Principle sketch map of TR-PEEM experiments.

At short delay times, when the pump and probe beams overlap, the oscillation of the LSPR hot spots is primarily governed by the interference between the pump and probe pulses, with the oscillation occurring at the carrier frequency. As the delay time increases and the pump and probe pulses become separated, the two plasmon fields, excited by the pump and probe pulses, can then interfere with each other, influencing the oscillation of the hot spots. By comparing the experimental results with numerically calculated time-resolved nonlinear photoemission signals, the dephasing time of the measured nanostructure can be determined.

2.2.5 Numerical simulations

The optical properties of the fabricated ATTA structures were simulated using the finite-difference time-domain (FDTD) method (Lumerical, Inc.). The geometry of the ATTA structures in the simulation was based on the experimentally designed parameters. The refractive index of TiO_2 was set to 2.4, and the optical properties of the Au material were taken from the data provided by Johnson and Christy.[21] A plane wave with normal

incidence was used as the excitation source. The structure was modeled with perfectly matched layers along the z-direction and periodic boundary conditions along the x- and y-directions. The simulations were performed on a discrete grid with a uniform mesh size of 1 nm.

2.3 Results and discussion

2.3.1 Characterization of morphology and far-field spectra

The interfacial structure between plasmonic metals and semiconductors plays a critical role in plasmon-induced charge transfer, which is essential for efficiently converting solar energy into chemical energy. In this study, the Au NDs/TiO_2 interface in the strong coupling ATTA structure was modified with Ti films of varying thicknesses (0.5, 2.0, and 5.0 nm), as shown in Figure 2.5a. And the typical surface morphology of the ATTA structure is presented in the SEM image (Figure 2.5b). From the histogram of the Au ND diameter distribution, which was fitted using a Gaussian function, the average diameter of the Au NDs was determined to be 89 nm, as depicted in Figure 2.5c.

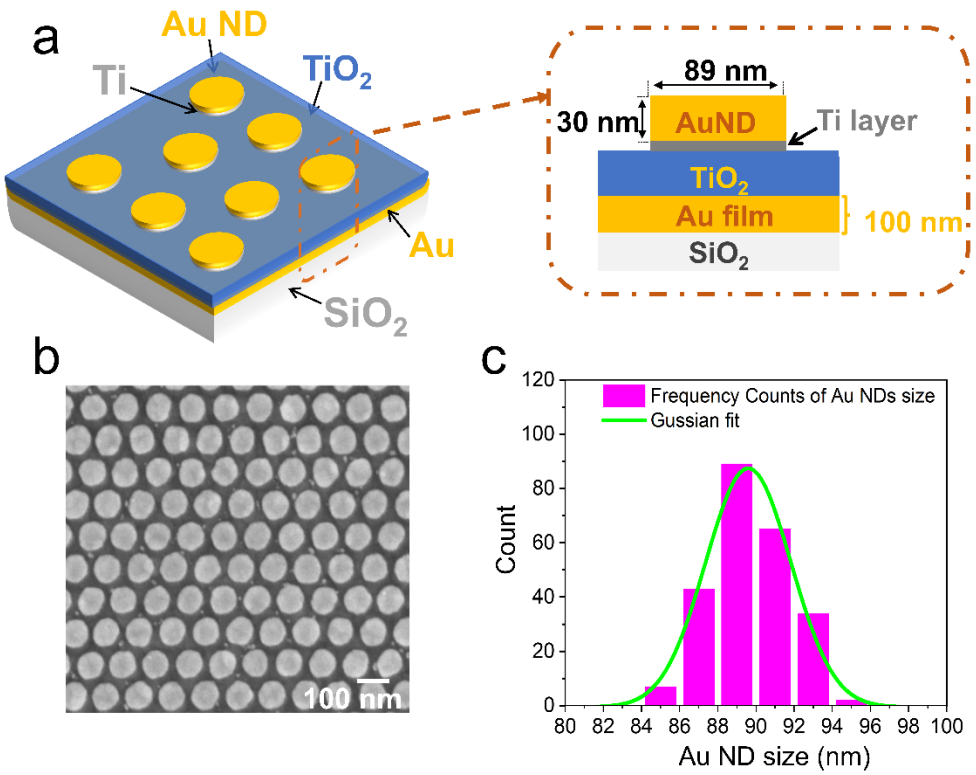

Figure 2.5 (a) Schematic diagram of the ATTA structure with cross-sectional view of the ATTA structure consisting of Au ND, Ti film, TiO_2 film, and 100 nm Au film. (b) Top-view SEM images of typical ATTA structure. (c) Histogram of Au ND diameter with Gaussian fit shown as green line. The size of Au ND was obtained to be 89 nm.

Figure 2.6a presents the absorption spectra of the ATTA structures with varying TiO_2 film thicknesses, where the LSPR and F-P nanocavity modes are well-matched. The absorption spectra were obtained by measuring the reflectance (R) and transmittance (T) of the ATTA structures and calculating $-log_{10}(R+T)$ as a function of wavelength. It should be note that T was nearly zero due to the 100 nm-thick Au film. For all ATTA structures, the absorption spectra exhibit two distinct bands in the measured wavelength range, an upper branch (P_+) and a lower branch (P_-). The generation of two new absorption bands at shorter and longer wavelengths is attributed to the strong coupling between the LSPR of Au NDs and the F-P cavity modes of the TiO_2/Au film,[22] as illustrated in Figures 2.6b-c.

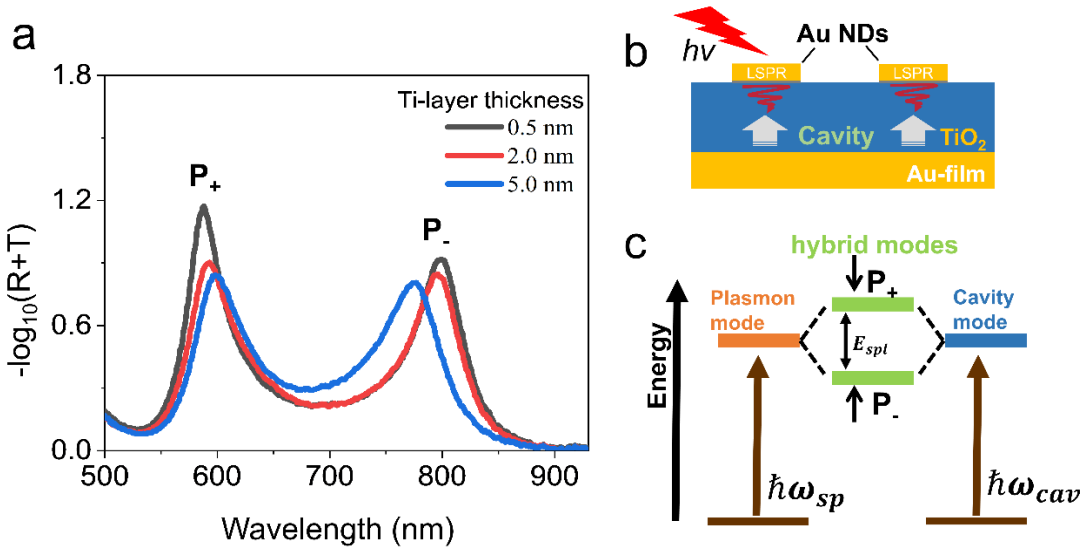

Figure 2.6 (a) Absorption spectra of ATTA structures with varying Ti film thicknesses at the Au NDs/TiO_2 interface. (b) Schematic illustration of the modal strong coupling between the LSPR of Au NDs and cavity modes in ATTA structure. (c) Energy-level diagram showing the modal strong coupling between the LSPR mode and F-P cavity mode in the ATTA system. The ω_{sp} and ω_{cav} present the resonance frequencies of plasmon mode and F-P cavity mode, respectively.

To verify that the ATTA structures in this study satisfy the conditions for modal strong coupling, we measured the absorption spectra of each structure as a function of TiO_2 film thickness. By plotting the energies corresponding to the longer and shorter wavelengths as a function of TiO_2 thickness (Figures 2.7a-c), we derived the dispersion curve, shown in Figures 2.7d-e. From this dispersion curve, the splitting energy (E_{spl}) of the ATTA structures with 0.5, 2.0, and 5.0 nm Ti film were determined to be 560, 520, and 460 meV, respectively, using a coupled harmonic oscillator model. For a strong coupling system, it should fulfill the following criterion:[22]

$$E_{spl} > \sqrt{\frac{\gamma_{P+}^2}{2} + \frac{\gamma_{P-}^2}{2}} \qquad 2.1$$

Where E_{spl} is the splitting energy, the γ_{P+} and γ_{P-} are the full widths at half maximum (FWHM) of the P_+ and P_-, respectively. The γ_{P+} and γ_{P-} of absorption band of each ATTA structure in Figure 2.6a were estimated using Lorentzian fitting. The $\sqrt{\frac{\gamma_{P+}^2}{2} + \frac{\gamma_{P-}^2}{2}}$ of the ATTA structure with 0.5, 2.0, and 5.0 nm was 130, 160, and 170 meV, respectively. These results confirm that the ATTA structures used in this study satisfy the modal

strong coupling condition.

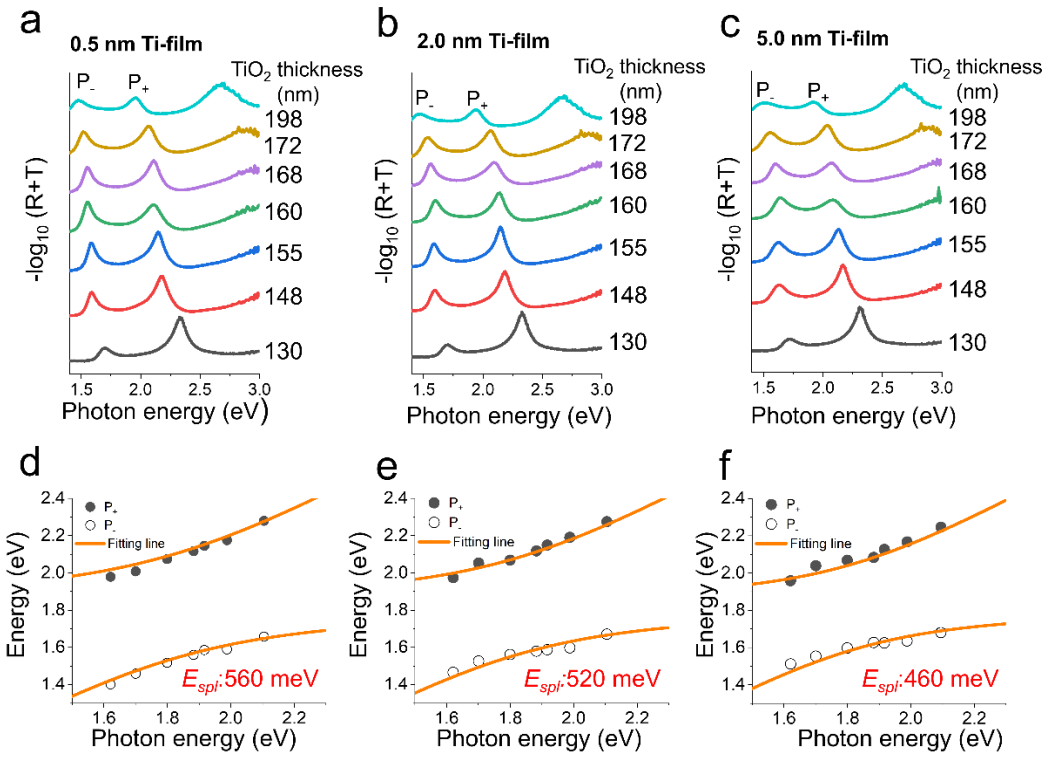

Figure 2.7 Absorption of ATTA structures with 0.5-5.0 nm (a)-(h) Ti film as a function of the thickness of TiO_2 film. The absorption of the samples was determined by measuring the total reflectance (R) from the samples and calculating $-log_{10}(R+T)$ as a function of photon energy. The transmittance (T) was almost zero in the ATTA system due to the presence of the Au film. The dispersion curves of hybrid modes in the ATTA structures with 0.5-5.0 nm Ti film (d)-(f). The E_{spl} were determined from their absorption spectra (a)-(c). The orange line shows the fit using the harmonic oscillator model. The P_+ represent upper branch, while P_- represent lower branch.

Form the E_{spl} analysis, the E_{spl} decreased from 560 to 460 meV with increasing Ti film thickness, as shown in Figures 2.7d-f. To understand the effect of Ti film thickness on E_{spl}, the E_{spl} can be expressed as follows:[23]

$$E_{spl} \propto \sqrt{Nf} \qquad 2.2$$

Where N and f represent the number of oscillator and oscillator strength, respectively. Due to the damping effect of the Ti film, which has a larger imaginary component as an adhesion layer, the oscillator strength of the LSPR of Au NDs decreases with increasing Ti film thickness. Consequently, the E_{spl} of the ATTA

system in strong modal coupling also decreases as the Ti film thickness increases.

2.3.2 Effect of Ti film thickness on near-field

To further investigate the near-field properties of ATTA structures with varying Ti film thicknesses, we employed the PEEM system to directly visualize the near-field enhancement. The PE intensity, which is nonlinearly correlated with the near-field, allows the PEEM image to be interpreted as a nonlinear map of the near-field intensity distribution near the metallic nanostructures. As shown in Figure 2.8, the PEEM images of ATTA structures with different Ti film thicknesses, excited by fs laser pulses at the absorption band peak position under normal incidence. It should be noted that the near-field PE intensity signal was captured from the entire 30 μm-FOV. It was observed that stronger localized hot spots were present in the ATTA structure with a 0.5 nm-thick Ti film. As the Ti film thickness increased, both the intensity and the number of hot spots decreased, indicating that the Ti film dampens the near-field enhancement.

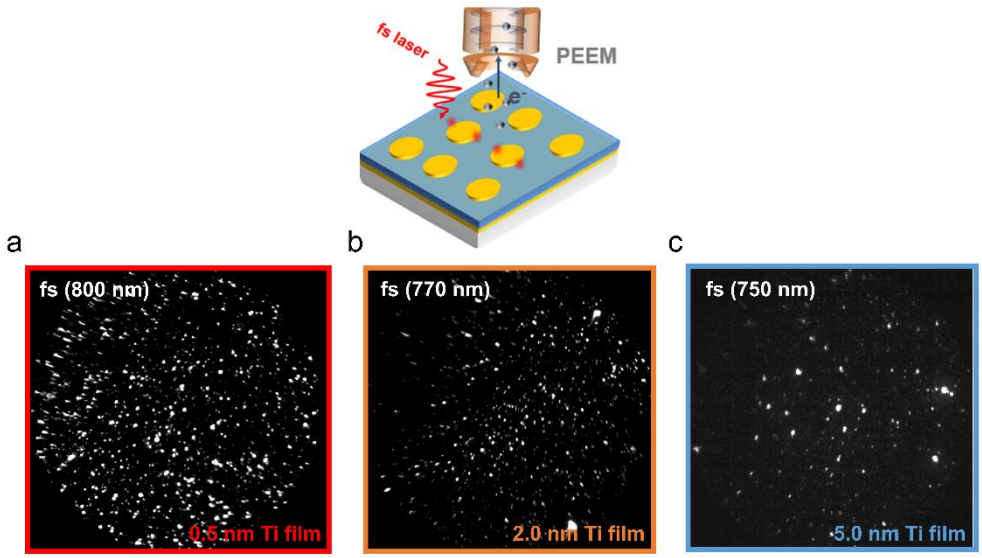

Figure 2.8 PEEM images (FOV of 30 μm) of ATTA with 0.5 (a), 2.0 (b), and 5.0 nm (c) under fs laser excitation.

Building on the previous discussions, the wavelength-dependent near-field enhancement of the ATTA structures with varying Ti film thicknesses under normal incidence was also explored. A series of PEEM images were captured by tuning the

excitation wavelength from 580 nm to 870 nm in 10 nm increments. By integrating the PE signal across the entire FOV and plotting it against the incident wavelength, the near-field spectrum was obtained. Since the PE intensity correlates with the near-field electric field intensity, the resulting wavelength-dependent near-field PE intensity spectrum reflects the nonlinear near-field response of the ATTA structures.

Figure 2.9 presents the near-field spectra for ATTA structures with Ti films of 0.5, 2.0, and 5.0 nm thicknesses. Two distinct peaks are observed in the near-field spectra, which are consistent with those in the far-field spectra shown in Figure 2.6a. It should be noted that the PE intensity of these two peaks is not in same scale due to differing pulse widths in the two wavelength regions (denoted by the double slash). Notably, the near-field amplitude decreases significantly as the Ti film thickness increases from 0.5 to 5.0 nm, suggesting that the Ti film dampens the near-field enhancement at the Au NDs/TiO_2 interface.

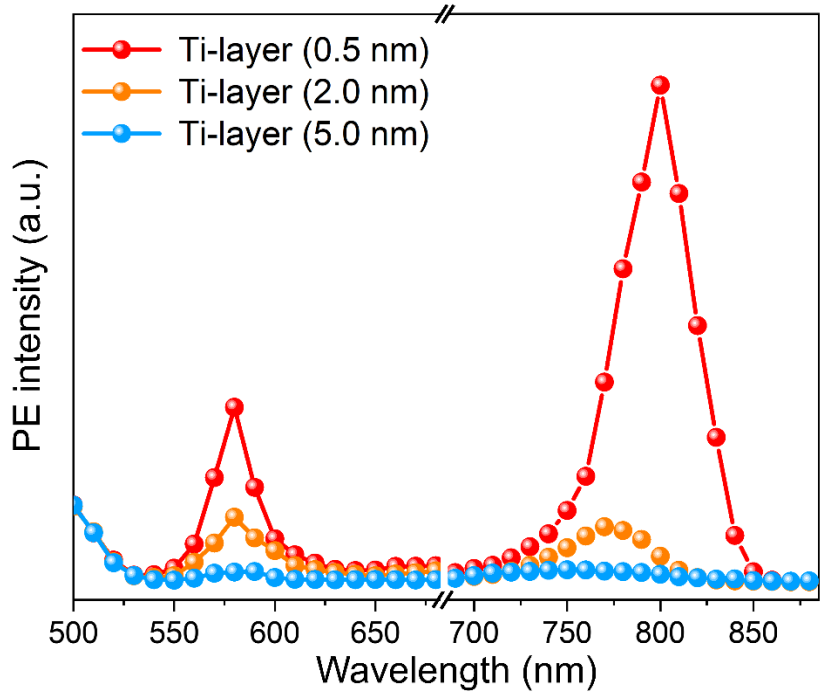

Figure 2.9 Wavelength-dependent PE intensity of the ATTA structures with Ti films of 0.5, 2.0 (orange), and 5.0 nm (cyan).

2.3.3 Numerical simulations

To further validate the experimental results regarding the effect of Ti film thickness on the near-field properties of ATTA structures, FDTD simulations were performed.

Figure 2.10b presents the near-field spectra of ATTA structures with varying Ti film thicknesses, showing that the near-field intensity decreases as the Ti film thickness increases. Figures 2.10c-d show the cross-sectional near-field distributions of different ATTA structures. It is clear that the near-field intensity of the ATTA structure with a thin Ti film is significantly stronger than that of the structure with a thicker Ti film. The maximum near-field intensity, commonly referred to as a "hot spot," is observed at the boundary between the Ti film and the TiO_2 film. This location serves as the monitoring point for obtaining the near-field spectra.

The simulation results are in good agreement with the experimental data obtained from PEEM measurements. These results indicate that the near-field enhancement at the Au/ TiO_2 interface is suppressed by the presence of the Ti film, primarily due to the significant dissipative imaginary component (ε_2) of the Ti material.[25, 26]

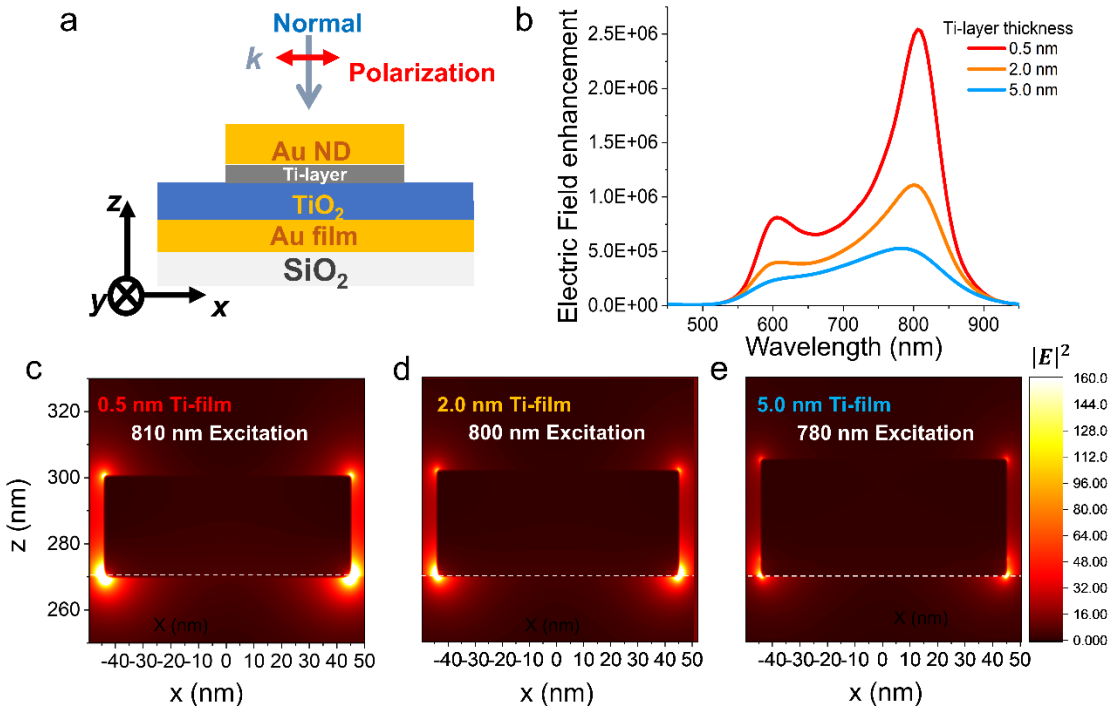

Figure 2.10 (a) Schematic of the simulation model for calculating near-field properties of ATTA structures with various thicknesses of Ti film. (b) Simulated near-field spectra at the Ti/TiO_2 interface as a function of different Ti film thickness. (c)-(d) show the cross-sectional near-field distribution on ATTA structure with 0.5, 2.0, and 5.0 nm-thick Ti film, respectively.

2.3.4 Effect of Ti film thickness on dephasing time of hybrid modes

From the experimental and simulation near-field spectra of ATTA structures, it can be found that the bandwidth of absorption band broaden as increasing of Ti film thickness. The bandwidth directly reflects the dephasing time of hybrid modes, while the investigation of dephasing time provides further insights into the damping effects induced by the Ti film at the Au NDs/TiO_2 interface. However, the dephasing time based on the optical spectral measurements usually suffers from the problem of inhomogeneous spectral broadening caused by the variation in metal nanostructures (e.g., shape and size). A few groups, for instance Petek's group,[27] Aeschlimann's group[28] as well as our group,[29, 30] have successfully measured the dephasing time of individual plasmonic nanostructure directly in the time domain using time-resolved photoemission electron microscopy (TR-PEEM). In this study, we also utilized the TR-PEEM system to directly measure the effect of Ti layer on the dephasing time under the modal strong coupling conditions in the time domain, which has been rarely reported in previous studies.

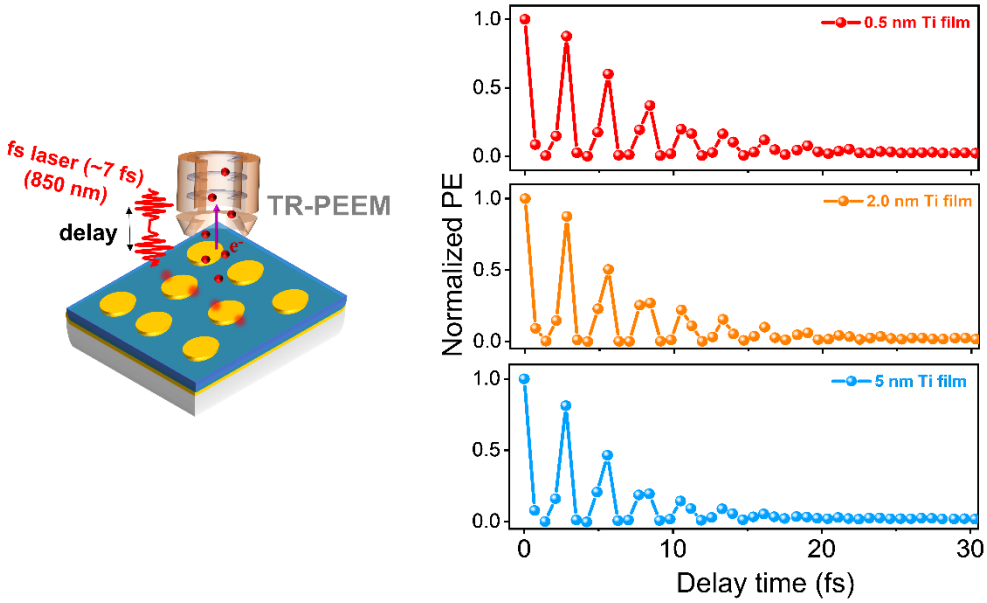

Figure 2.11 Time evolution of the PE intensity on ATTA structure with various thicknesses of Ti film within the delay time of 0-30 fs.

As described in the experimental section, TR-PEEM system is developed by

combining PEEM with the interferometric pump-probe technique. In this setup, a Mach-Zehnder interferometer is used to split and support the pump and probe pulses. PEEM images are recorded by adjusting the delay between the pump and probe pulses. Similar to the near-field spectra, the time evolution of the PE intensity is obtained by integrating the PE intensity of each PEEM image and plotting it against the delay time.

Figure 2.11 presents the time evolution of the PE intensity for ATTA structures with various Ti film thicknesses at the Au NDs/TiO_2 interface, within a phase delay range of 0 to 30 fs. The figure clearly shows that the three curves exhibit identical oscillation frequencies as a function of the delay time between the pump and probe laser pulses. While the oscillation frequency remains unchanged by the Ti film, the coherence between the two fields excited by the pump and probe pulses decays more rapidly as the Ti film thickness increases. This suggests that the Ti film significantly affects the dephasing time, even though it does not alter the oscillation frequency.

To quantitatively determine the dephasing time, the time-resolved nonlinear PE signal is modeled using a plasmon oscillator approach with an exponential damping term, which incorporates the nonlinearity of photoemission.[24, 31] Typically, the model requires two key parameters: the driving electric field $E(t) + E(t + t_{\mathrm{d}})$, where t_{d} is the time delay between the pump and probe pulses. In the experiment, $E(t)$ is defined by the sech²-shaped pulse of the fs laser with a duration of 7 fs. Additionally, the local field enhancement allows for multiphoton photoemission, and the order of nonlinear photoemission is another critical factor that needs to be verified. For the absorption peaks of the ATTA structures at the P- mode, at least three photons are required to induce photoemission. This is confirmed by a laser power-dependent study, where a log-log plot of photoemission intensity versus laser power yields slopes of 3.8, 3.8, and 3.1 for the 0.5, 2.0, and 5.0 nm-thick Ti films at the Au NDs/TiO_2 interface. Once the driving electric field and the nonlinear photoemission order are determined, the time-resolved nonlinear PE signal can be calculated by adjusting the dephasing time fitting parameters. The detailed calculation procedure is outlined below.

A simple damped harmonic oscillator mode was employed to describe the time-

dependent surface plasmon field. The plasmon field $E_{pl}(t)$ can be described as following:

$$E_{pl}(t) \propto \int_{-\infty}^{\tau} \frac{1}{\omega_0} K(t') e^{-\gamma(t-t')} sin[\omega_0(t-t')] dt' \quad 2.3$$

Where the $K(t)$ represents the driving field, which is expressed as $K(t) = E(t) + E(t+t_{\mathrm{d}})$ for the interferometric pump-probe measurements in this study. t_{d} denotes the delay between the pump and probe pulses, while ω_0 represents the plasmon resonance frequency. $\gamma = 1/2T$, where T means the dephasing time of the plasmon field. Given the nonlinearity of the PE signal in this study, the time-dependent PE intensity as a function of the delay time t_{d} can be described by the following expression:

$$I(t_{\mathrm{d}}) \propto \int_{-\infty}^{+\infty} \left|E_{pl}(t)\right|^{2N} dt \quad 2.4$$

Where N means the nonlinear order of PE. By using these two equations, the PE intensity as a function of the t_{d} can be obtained. Using the equations provided, the PE intensity as a function of the delay time t_{d} can be derived. By adjusting the dephasing time and excitation wavelengths, time-resolved PE intensity signal curves were generated, which closely match the experimental results shown in Figure 2.11. Based on these calculations, we determined the dephasing times of the ATTA structures to be 5.6, 4.5, and 3.5 fs for Ti film thicknesses of 0.5, 2.0, and 5.0 nm, respectively. These results clearly indicate that as the Ti film thickness increases, the dephasing time of the ATTA structures decreases.

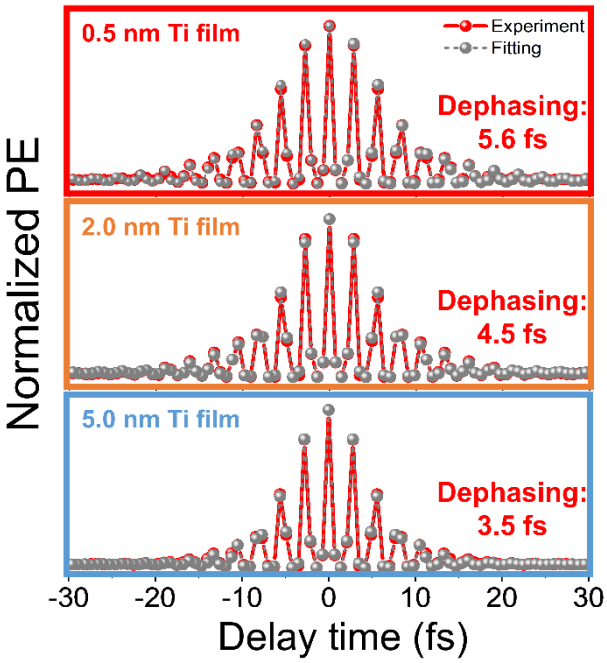

Figure 2.12 TR-PEEM measured (red dotted lines) and numerically simulated (gray dotted lines) PE intensity curves as a function of the delay time between the pump and probe pulses. The panels from top to bottom are ATTA with Ti film thicknesses of 0.5, 2.0, and 5.0 nm.

Combined with the near-field spectra of ATTA structures, we conclude that the Ti film causes LSPR damping due to its large dissipative imaginary component. This damping effect reduces the near-field intensity and shortens the dephasing time.

2.4 Conclusions

In this chapter, the effect of the Ti film on the near-field properties of the ATTA structure under modal strong coupling conditions was investigated using PEEM, including near-field mapping, spectral analysis, and time-resolved measurements. The results showed that near-field enhancement diminished with increasing Ti film thickness. Furthermore, time-resolved PEEM quantified the ultrafast dephasing times of the hybrid modes, revealing a progressive reduction for Ti film thicknesses of 0.5, 2.0, and 5.0 nm. These findings indicate that modifying the Au ND/TiO_2 interface with a Ti film significantly suppresses near-field enhancement and shortens the dephasing time of the hybrid modes under strong coupling conditions. In the next chapter, we will examine how the Ti film influences electron transfer processes at the Au/TiO_2 interface.

2.5 References

[1] Ueno, K.; Oshikiri, T.; Sun, Q.; Shi, X.; Misawa, H. Solid-state plasmonic solar cells. *Chem. Rev.* **2017**, *118*, 2955-2993.

[2] Rao, P. V.; Baral, S. S.; Dey, R.; Mutnuri, S. Biogas generation potential by anaerobic digestion for sustainable energy development in India. *Renew. Sustain. Energy Rev.* **2010**, *14*, 2086-2094.

[3] Catchpole, K. a.; Polman, A. Plasmonic solar cells. *Opt. Express* **2008**, *16*, 21793-21800.

[4] Afgan, N. H.; Al Gobaisi, D.; Carvalho, M. G.; Cumo, M. Sustainable energy development. *Renew. Sustain. Energy Rev.* **1998**, *2*, 235-286.

[5] Su, Y. W.; Lin, W. H.; Hsu, Y. J.; Wei, K. H. Conjugated polymer/nanocrystal nanocomposites for renewable energy applications in photovoltaics and photocatalysis. *Small* **2014**, *10*, 4427-4442.

[6] Walter, M. G.; Warren, E. L.; McKone, J. R.; Boettcher, S. W.; Mi, Q.; Santori, E. A.; Lewis, N. S. Solar water splitting cells. *Chem. Rev.* **2010**, *110*, 6446-6473.

[7] Hashimoto, K.; Irie, H.; Fujishima, A. TiO_2 photocatalysis: a historical overview and future prospects. *Jpn. J. Appl. phys.* **2005**, *44*, 8269.

[8] Ni, M.; Leung, M. K.; Leung, D. Y.; Sumathy, K. A review and recent developments in photocatalytic water-splitting using TiO_2 for hydrogen production. *Renew. Sustain. Energy Rev.* **2007**, *11*, 401-425.

[9] Jia, C.; Li, X.; Xin, N.; Gong, Y.; Guan, J.; Meng, L.; Meng, S.; Guo, X. Interface−engineered plasmonics in metal/semiconductor Heterostructures. *Adv. Energy Mater.* **2016**, *6*, 1600431.

[10] Liu, Y.-E.; Shi, X.; Yokoyama, T.; Inoue, S.; Sunaba, Y.; Oshikiri, T.; Sun, Q.; Tamura, M.; Ishihara, H.; Sasaki, K. Quantum-coherence-enhanced hot-electron injection under modal strong coupling. *ACS Nano* **2023**, *17*, 8315-8323.

[11] Knight, M. W.; Sobhani, H.; Nordlander, P.; Halas, N. J. Photodetection with active optical antennas. *Science* **2011**, *332*, 702-704.

[12] Linic, S.; Christopher, P.; Ingram, D. B. Plasmonic-metal nanostructures for efficient conversion of solar to chemical energy. *Nat. Mater.* **2011**, *10*, 911-921.

[13] Brongersma, M. L.; Halas, N. J.; Nordlander, P. Plasmon-induced hot carrier science and technology. *Nat. Nanotechnol.* **2015**, *10*, 25-34.

[14] Cao, Y.; Shi, X.; Oshikiri, T.; Zu, S.; Sunaba, Y.; Sasaki, K.; Misawa, H. Near-

field engineering for boosting the photoelectrochemical activity to a modal strong coupling structure. *Chem. Commun.* **2021**, *57*, 524-527.

[15] Schweikhard, V.; Grubisic, A.; Baker, T. A.; Thomann, I.; Nesbitt, D. J. Polarization-dependent scanning photoionization microscopy: ultrafast plasmon-mediated electron ejection dynamics in single Au nanorods. *ACS Nano* **2011**, *5*, 3724-3735.

[16] Imura, K.; Ueno, K.; Misawa, H.; Okamoto, H. Anomalous light transmission from plasmonic-capped nanoapertures. *Nano Lett.* **2011**, *11*, 960-965.

[17] Tanaka, Y.; Ishiguro, H.; Fujiwara, H.; Yokota, Y.; Ueno, K.; Misawa, H.; Sasaki, K. Direct imaging of nanogap-mode plasmon-resonant fields. *Opt. Express* **2011**, *19*, 7726-7733.

[18] Geldhauser, T.; Kolloch, A.; Murazawa, N.; Ueno, K.; Boneberg, J.; Leiderer, P.; Scheer, E.; Misawa, H. Quantitative measurement of the near-field enhancement of nanostructures by two-photon polymerization. *Langmuir* **2012**, *28*, 9041-9046.

[19] Leiderer, P.; Bartels, C.; Koenig-Birk, J.; Mosbacher, M.; Boneberg, J. Imaging optical near-fields of nanostructures. *Appl. Phys. Lett.* **2004**, *85*, 5370-5372.

[20] Eversole, D.; Luk'Yanchuk, B.; Ben-Yakar, A. Plasmonic laser nanoablation of silicon by the scattering of femtosecond pulses near gold nanospheres. *Appl. Phy. A* **2007**, *89*, 283-291.

[21] Johnson, P. B.; Christy, R.-W. Optical constants of the noble metals. *Phy. Rev. B* **1972**, *6*, 4370.

[22] Shi, X.; Ueno, K.; Oshikiri, T.; Sun, Q.; Sasaki, K.; Misawa, H. Enhanced water splitting under modal strong coupling conditions. *Nat. Nanotechnol.* **2018**, *13*, 953-958.

[23] Suzuki, M.; Nishiyama, K.; Kani, N.; Yu, X.; Uzumi, K.; Funahashi, M.; Shimokawa, F.; Nakanishi, S.; Tsurumachi, N. Observation of ultrastrong-coupling regime in the Fabry–Pérot microcavities made of metal mirrors containing Lemke dye. *Appl. Phys. Lett.* **2019**, *114*.

[24] Hanke, T.; Krauss, G.; Träutlein, D.; Wild, B.; Bratschitsch, R.; Leitenstorfer, A. Efficient nonlinear light emission of single gold optical antennas driven by few-cycle near-infrared pulses. *Phys. Rev. Lett.* **2009**, *103*, 257404.

[25] Aouani, H.; Wenger, J.; Gérard, D.; Rigneault, H.; Devaux, E.; Ebbesen, T. W.; Mahdavi, F.; Xu, T.; Blair, S. Crucial role of the adhesion layer on the plasmonic fluorescence enhancement. *ACS Nano* **2009**, *3*, 2043-2048.

[26] Habteyes, T. G.; Dhuey, S.; Wood, E.; Gargas, D.; Cabrini, S.; Schuck, P. J.; Alivisatos, A. P.; Leone, S. R. Metallic adhesion layer induced plasmon damping and molecular linker as a nondamping alternative. *ACS Nano* **2012**, *6*, 5702-5709.

[27] Kubo, A.; Pontius, N.; Petek, H. Femtosecond microscopy of surface plasmon polariton wave packet evolution at the silver/vacuum interface. *Nano Lett.* **2007**, *7*, 470-475.

[28] Schmuttenmaer, C.; Aeschlimann, M.; Elsayed-Ali, H.; Miller, R.; Mantell, D.; Cao, J.; Gao, Y. Time-resolved two-photon photoemission from Cu (100): Energy dependence of electron relaxation. *Physi. Rev. B* **1994**, *50*, 8957.

[29] Sun, Q.; Yu, H.; Ueno, K.; Kubo, A.; Matsuo, Y.; Misawa, H. Dissecting the few-femtosecond dephasing time of dipole and quadrupole modes in gold nanoparticles using polarized photoemission electron microscopy. *ACS Nano* **2016**, *10*, 3835-3842.

[30] Sun, Q.; Ueno, K.; Yu, H.; Kubo, A.; Matsuo, Y.; Misawa, H. Direct imaging of the near field and dynamics of surface plasmon resonance on gold nanostructures using photoemission electron microscopy. *Light Sci. Appl.* **2013**, *2*, e118-e118.

[31] Lamprecht, B.; Krenn, J.; Leitner, A.; Aussenegg, F. Resonant and off-resonant light-driven plasmons in metal nanoparticles studied by femtosecond-resolution third-harmonic generation. *Phys. Rev. Lett.* **1999**, *83*, 4421.

Chapter 3

Improving electron transfer under strong coupling conditions via Au/TiO_2 interfacial modulation with a Ti layer

3.1 Introduction

Localized surface plasmon resonance (LSPR) in metallic nanostructures (NSs) enables the conversion of absorbed photons into energetic energy via generating.[1-3] When these metallic NSs are integrated with semiconductor, such as Au/TiO_2, a Schottky barrier was formed at the interface, promoting charge separation and electron injection into the semiconductor's conduction band (CB). Such configurations have been widely applied in photodetectors,[4-8] and photovoltaics,[9-12] with the Schottky barrier playing a crucial role in optimizing charge transfer efficiency. Pioneering studies by Tatsuma's group[13, 14] in 2004–2005 and Furube et al.[15] in 2007 established the foundational understanding of plasmon-induced electron dynamics, demonstrating photocurrent generation and hot electron transfer from Au nanodots to TiO_2 via transient absorption spectroscopy.

Building on these insights, Au nanostructure-loaded TiO_2 systems have been extensively utilized for photochemical reactions under visible-to-near-infrared irradiation, owing to their stability and effective electron transfer at the Au NS/TiO_2 interface.[16-18] However, the conventional single-layer Au NSs on TiO_2 face limitations in photon absorption, resulting in relatively low electron transfer efficiency. The predominant electron transfer mechanism, described by the plasmon-induced hot electron transfer model, involves the decay of LSPR-generated hot electrons across the Schottky barrier into the CB of TiO_2. Addressing these limitations requires advancements in light absorption enhancement and optimization of charge transfer pathways to further improve the efficiency and performance of Au NS/TiO_2 heterostructure devices.

Recently, we developed a strong coupling Au nanodisks (Au NDs)/TiO_2/Au film

(ATA) structure (Figure 2.5) that significantly enhances light absorption efficiency while improving the quantum yield of water oxidation.[19] Building on previous findings that Ti films promote electron transfer at the Au/Si interface,[7] Chapter 2 examines the design and characterization of a strong coupling Au NDs/Ti film/TiO_2/Au film (ATTA) structure. Specifically, it explores the influence of the Ti film at the Au/ TiO_2 interface on the near-field properties of the ATTA structure.

This chapter further investigates the effect of Ti film thickness on electron transfer efficiency and incident photon-to-current efficiency (IPCE) using transient absorption (TA) spectroscopy and a three-electrode system. ATTA structures with Ti films of varying thicknesses (0.5–10 nm) were fabricated, revealing that a suitable Ti film thickness obviously enhances electron transfer efficiency. The TA and IPCE action spectra confirm these improvements. Additionally, the underlying mechanisms by which the Ti film-enhanced electron transfer are discussed, providing insights into the role of interface engineering in optimizing plasmonic photocatalytic systems.

3.2 Experimental details

3.2.1 ATTA, ATT, and ASTTA structure fabrication

The ATTA structures with Ti film thicknesses ranging from 6.0 to 10.0 nm were fabricated, following the fabrication procedures described in Chapter 2. A control group, Au ND/TiO_2 (ATA) structure, was also prepared, with the Ti film thickness varying between 0.5 and 10.0 nm, but without the Au film. Additionally, the Au ND/SiO_2/Ti/ TiO_2/Au film (ASTTA) structure was fabricated using a similar process to that for the ATTA and ATT structures, with the key difference being the deposition of Au, SiO_2, and Ti films via electron-beam evaporation.

3.2.2 Transient absorption measurements

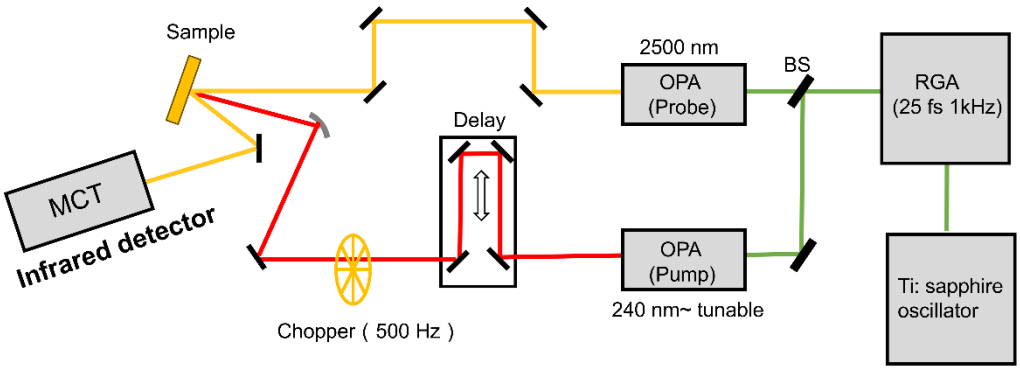

Figure 3.1 The Schematic diagram of pump-probe setup.

The transient absorption (TA) measurement was conducted using the pump-probe technique, as illustrated in Figure 3.1. The fundamental laser source, generated by a Ti: sapphire laser with a central wavelength of 800 nm and a pulse duration of approximately 25 fs, was split into two beams: one for the pump pulse and the other for the probe pulse. The pump pulse was directed into a collinear optical parametric amplifier (TOPAS-C, Light Conversion), chopped at 500 Hz, and used to generate a visible excitation source. The probe pulse was produced by a second TOPAS device, which provided a 2500 nm probe to monitor the transient response. A stepper linear stage (SGSP26-100, Sigma Koki) was employed to control the time delay between the pump and probe pulses. Both pulses were directed onto the sample using a concave mirror, and the reflection signals from the sample were collected and integrated using a liquid-nitrogen-cooled mercury cadmium telluride (MCT) detector.

3.2.3 Photoelectrochemical measurements

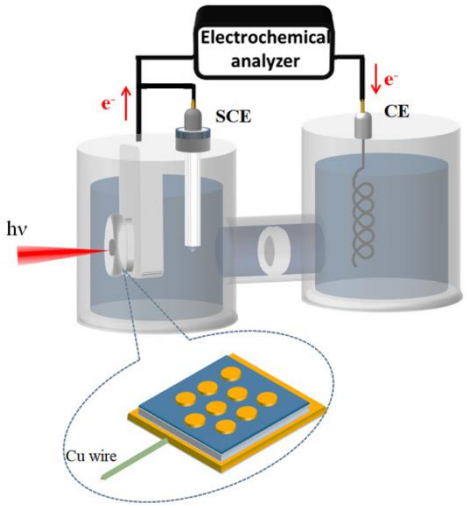

Figure 3.2 Schematic of the three-electrode photoelectrochemical cell for the IPCE measurement.

Photoelectrochemical (PEC) measurements on ATTA structures were conducted using an electrochemical analyzer (CHI660E) with a three-electrode system. The ATTA samples, with varying Ti film thicknesses, were employed as the working electrode. An In-Ga alloy (2:1 weight ratio) film was pasted to the backside and sidewalls of the substrate to establish ohmic contact and was connected to the electrochemical analyzer using copper lead wires. A saturated calomel electrode (SCE) and a platinum wire were used as the reference and counter electrodes, respectively. Potassium hydroxide (KOH) was used as the supporting electrolyte, with a 0.1 mol/dm^3 aqueous solution for the PEC measurements. Prior to the measurements, the electrolyte solution was purged with nitrogen gas for 1 hour to remove dissolved oxygen. An 800 W xenon lamp was used as the light source, with the irradiation wavelength selected using a bandpass filter with a full width at half maximum (FWHM) of less than 15 nm. During all PEC measurements, the working electrode potential was maintained at +0.3 V versus SCE.

3.2.4 Numerical simulations

The energy absorption of the Ti film in ATTA structures was simulated using the finite-difference time-domain (FDTD) method (Lumerical, Inc.). The simulation setup was

similar to that described in Chapter 2, with the main difference being the monitoring approach. A three-dimensional energy monitor was employed, specifically covering only the Ti film, allowing for the detection of the near-field energy absorption efficiency of Au NDs under identical excitation conditions across different Ti film thicknesses.

3.3 Results and discussion

3.3.1 Effect of Ti film thickness on far-field spectra

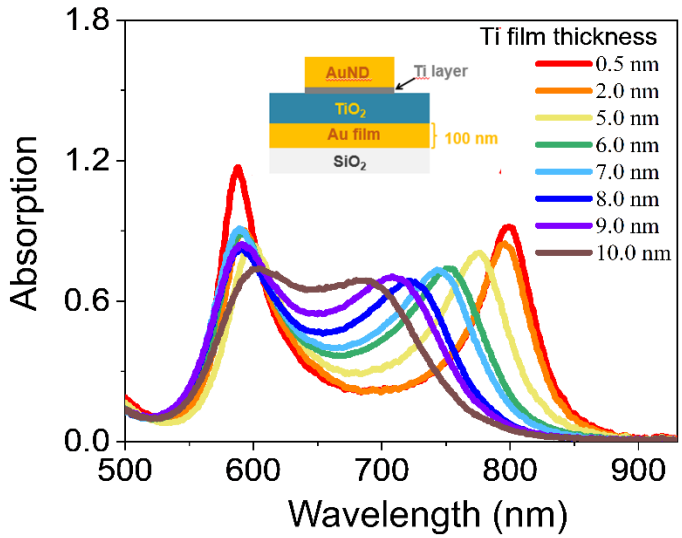

Figure 3.3 (a) Absorption spectra of ATTA structures with varying Ti film thicknesses at the Au ND/TiO_2 interface. (b) Variation of splitting energy as a function of Ti film thickness.

In this study, we used the same strong coupling ATTA structure introduced in Chapter 2, with continue to adjustment the Ti film thickness (ranging from 0.5 to 10 nm) at the Au NDs/TiO_2 interface to investigate its impact on electron transfer. The absorption spectra of these ATTA structures were obtained by using $-log(R+T)$, with varying Ti film thicknesses are shown in Figure 3.3. For all ATTA structures, the absorption spectra exhibit two absorption bands in the measurement wavelength, an upper branch (UB), and a lower branch (LB), which were attributed to the strong coupling between the LSPR of Au NDs and the Fabry–Pérot (F-P) nanocavity modes of the TiO_2/Au film. Note that all ATTA structures shown in Figure 3.3 were adjusted to be near the tunning

condition, meaning that the LSPR mode in each structure is closely near the cavity mode.

To further confirm that the ATTA structures with Ti film thicknesses between 6.0 and 10.0 nm satisfy the strong coupling condition, we measured the absorption spectra of each ATTA structure as a function of TiO_2 thickness. Dispersion curves were obtained by plotting the resonance energies corresponding to the UB and LB, enabling the determination of the splitting energy (E_{spl}) using a coupled harmonic oscillator model, as shown in Figure 3.4. The linewidths of the absorption peaks for each tuned ATTA structure (Figure 3.3a) were estimated using a Lorentzian function. As summarized in Table 1, all the ATTA structures fulfill the strong coupling condition, $E_{spl} > \sqrt{\frac{\gamma_{UB}^2}{2} + \frac{\gamma_{LB}^2}{2}}$, E_{spl} is the splitting energy, the γ_{UB} and γ_{LB} are the full widths at half maximum (FWHM) of the UB and LB, respectively.

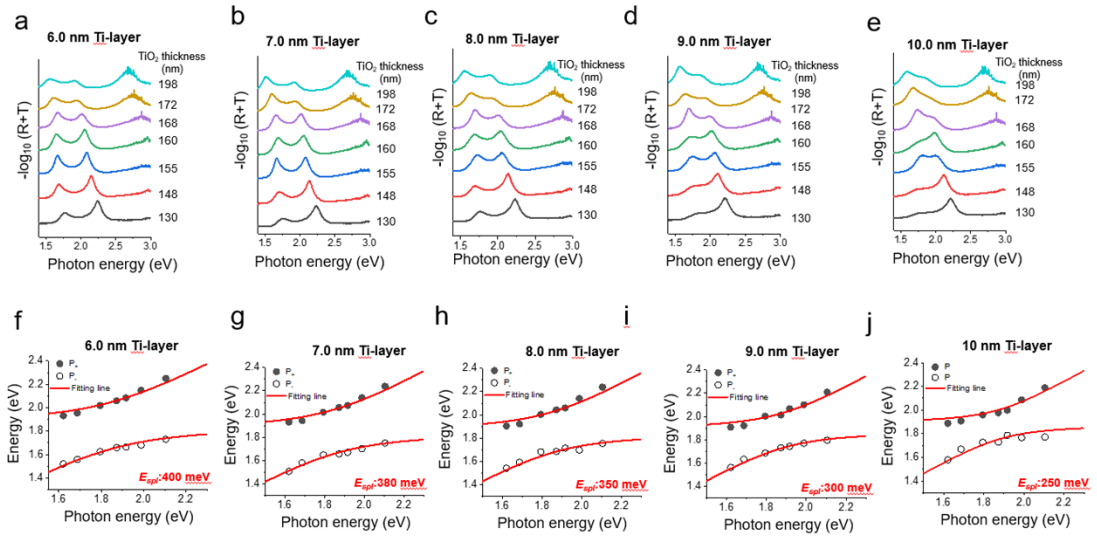

Figure 3.4 Absorption of ATTA structures with 6.0-10.0 nm (a)-(e) Ti film as a function of TiO_2 film. Dispersion curves of hybrid modes in the ATTA structures with 6.0-10.0 nm Ti film (f)-(j). E_{spl} were determined from their absorption spectra in (a)-(e). The red line shows the fit using the harmonic oscillator model.

Table 1. The E_{spl} and linewidth of the absorption bands in Figures 3.3 and 3.4 determine that the structure fulfils the strong coupling condition.

Ti film	E_{spl}(eV)	γ_{LB}(eV)	γ_{UB}(eV)	$\sqrt{(\gamma_{UB}^2+\gamma_{LB}^2)/2}$ (eV)
6.0 nm	0.40	0.22	0.14	0.18
7.0 nm	0.38	0.23	0.15	0.19
8.0 nm	0.35	0.24	0.17	0.21
9.0 nm	0.30	0.25	0.19	0.22
10.0 nm	0.25	0.27	0.21	0.23

A similar trend to that observed in Chapter 2 was found: the E_{spl} continuously decreased as the Ti film thickness increased. To further confirm that this behavior is due to LSPR damping induced by the Ti film, additional experiments were conducted. Au ND/Ti/TiO_2 (ATT) structures without the Au film were fabricated, and the effect of Ti film thickness on the extinction spectra was examined, as shown in Figure 3.5. The results reveal a decrease in LSPR intensity and an increase in the FWHM as the Ti film thickness increases, indicating that plasmon damping becomes more obviously with thicker Ti films. This behavior supports the conclusion that the Ti film reduces the LSPR oscillator intensity, which in turn leads to a decrease in the splitting energy of the strongly coupled ATTA system as the Ti film thickness increases.

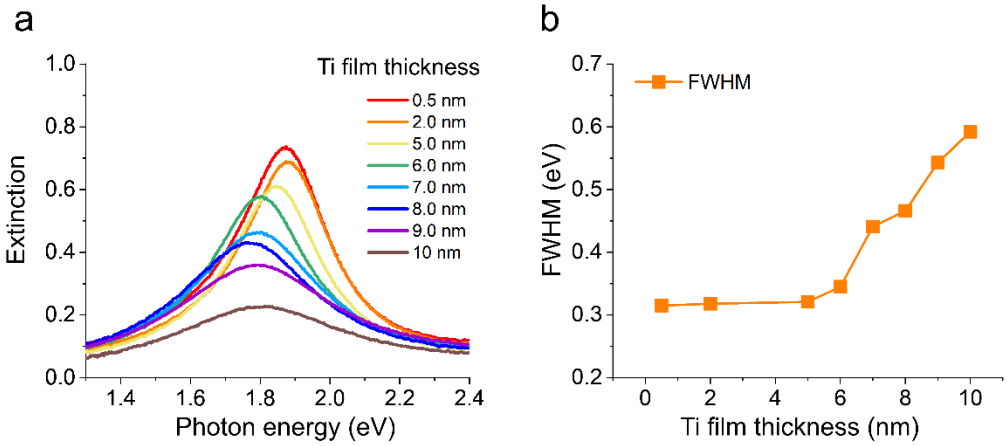

Figure 3.5 (a) Far-field extinction spectra of the ATT structure with varying Ti film thicknesses. (b) The FWHM of the extinction spectra in (a), estimated through Lorentzian fitting, as a function of Ti film thickness.

3.3.2 Effect of Ti film thickness on electron injection

To investigate the impact of the Ti film on electron transfer, we conducted transient

absorption (TA) measurements on the ATTA structures. The transient signals were recorded as $\Delta A = -log_{10}(R/R_0)$, where R and R_0 represent the reflections from the sample with and without pump pulses, respectively, and are expressed in units of optical density (OD). Additionally, we performed TA measurements on the Au NDs/Ti/ TiO_2 (ATT) structure, which lacks the nanocavity, as shown in Figure 3.6. Notably, a clear transient response was observed in the ATTA structure under both the UB and LB pump pulses, while no significant response was detected in the ATT structure. These results prompted further investigation of Ti thickness-dependent electron transfer in ATTA structures using TA measurements.

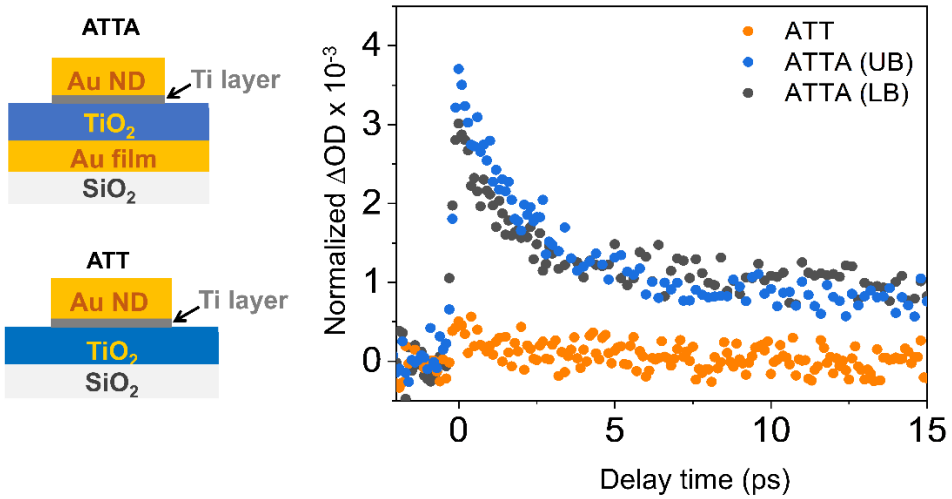

Figure 3.6 The time profiles of the transient measurements for the ATTA and ATT structures with a Ti film thickness of 5 nm are shown. The pump laser wavelengths were 590 nm, 770 nm, and 670 nm for the ATTA (UB), ATTA (LB), and ATT structures, respectively. The time profiles were calculated by normalizing the change in optical density (ΔOD) to the number of incident photons (n) and the absorption at the pump wavelength (A), as represented by the formula $\Delta OD/n/A$ (normalized ΔOD).

The time profiles of the transient response for the ATTA structure were measured upon excitation at its UB and LB absorption peaks. The observed decay in the time profiles of the TA measurements is attributed to the recombination of electrons and holes.[20, 21] Specifically, during LSPR excitation, electrons are injected into the CB of TiO_2. These electrons then recombine with holes at the interface, causing a decay in the transient signal. This decay can be modeled using a second-order reaction model[22]

$$\Delta OD = \frac{\alpha[C_0]}{1+k[C_0]t} + const. \qquad 3.1$$

where $[C_0]$ is the concentration of injected electrons near time zero, k is the decay rate, and α is the extinction coefficient. In this study, we also this model to fit the time profile of the TA measurements as the solid color lines superposed in Figure 3.7.

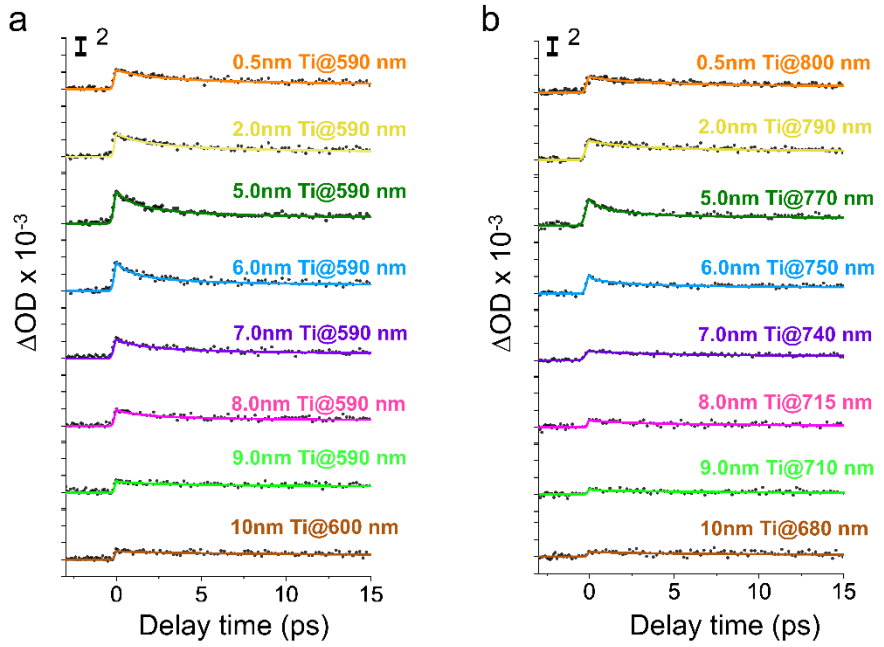

Figure 3.7 Time profiles of the TA measurements pumped at the UB (a) and the LB (b). The insert scale bars in (a) and (b) indicate an ΔOD of 2×10^{-3}.

Table 2 Fit ΔOD_{max} of the hot-electron decay curves shown in Figure 3.5 to the fitting mode of Equation 3.1

Ti film	0.5 nm	2.0 nm	5.0 nm	6.0 nm	7.0 nm	8.0 nm	9.0 nm	10 nm
ΔOD_{max}_UB	2.3	2.8	3.8	3.3	2.4	1.8	1.4	1.0
ΔOD_{max}_LB	1.8	2.3	3.1	2.0	1.3	1.0	0.7	0.6

In the transient curves, the maximum transient signal (ΔOD_{max}) near time zero corresponds to the total amount of electrons injected into the CB of TiO_2. The measured values of ΔOD_{max} for ATTA structures with varying Ti film thicknesses are summarized in Table 2. To further confirm the electron transfer process, the apparent quantum efficiency (AQE) of electron injection into TiO_2 was calculated using the formula $\Delta OD_{max}/n/A$, where n represents the number of incident photons and A is

the absorption at the pump wavelength. For direct AQE comparison, the normalized AQE (N-AQE) was determined by taking the AQE of the Ti film (10.0 nm) as a reference.

Figure 3.8 shows the N-AQE values, pumped at the upper (pink) and lower (orange) branches, as a function of Ti film thickness. The results reveal that electron injection into TiO_2 increased steadily as the Ti film thickness was increased from 0.5 to 5.0 nm, but then decreased as the thickness was further increased from 5.0 to 10.0 nm. Notably, when the Ti film thickness increased from 0.5 to 5.0 nm, the AQE of electron injection into TiO_2 increased appropriately 1.8 times, even though the LSPR was damped by the Ti film, as discussed in Chapter 2.

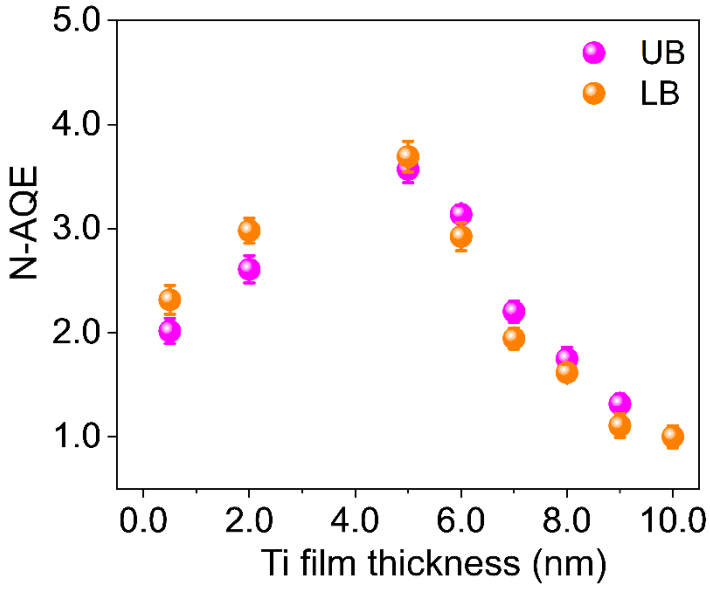

Figure 3.8 N-AQE as a function of Ti film thickness.

3.3.3 Effect of Ti film thickness on photocurrent generation

The photocurrent generation, measured using a three-electrode system, further corroborates the Ti film's influence on electron injection and its applicability to PEC reactions (Figure 3.9a). Figure 3.9b presents the I-t curves obtained under 580 nm light illumination, with the working electrode potential set at +0.3 V vs. SCE. The photocurrent exhibited a clear response to the light being switched on and off. Notably, the ATTA structure with a 5.0 nm Ti film (green) generated the highest photocurrent.

The variation in photocurrent as a function of Ti film thickness closely mirrored the trend observed in the N-AQE of electron injection into TiO_2 (Figure 3.8), reinforcing the link between optimized Ti film thickness and enhanced PEC performance.

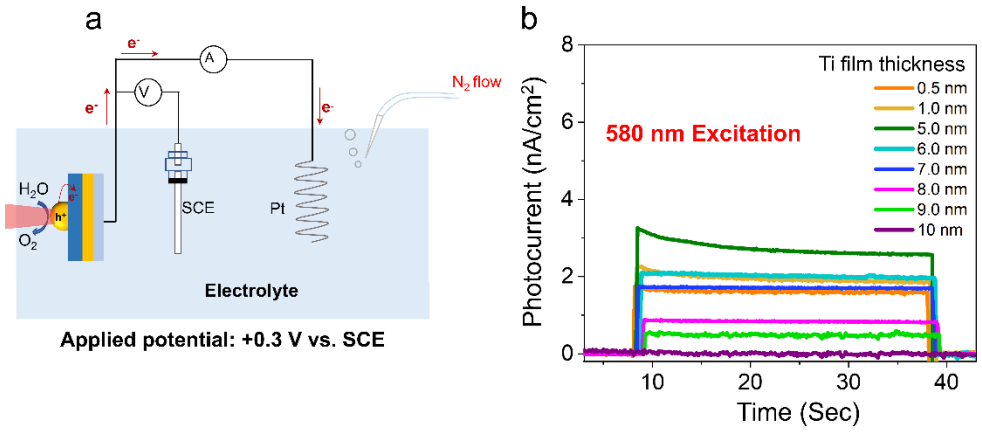

Figure 3.9 (a) Schematic of three-electrode system. (b) I-t curves of ATTA structures with varying Ti film thicknesses corresponding to excitation light of 580 nm. The experiments were performed at an applied potential of +0.3 V vs. SCE during the PEC measurements.

The photocurrent conversion efficiency of ATTA structure with varying Ti film thicknesses was evaluated using the incident photon-to-electron conversion efficiency (IPCE), calculated with the following equation:

$$IPCE(\%) = \frac{1240 \times I(A/cm^2)}{\lambda(nm) \times P(W/cm^2)} \times 100\% \qquad 3.2$$

where, I represents the photocurrent density under monochromatic light irradiation, λ is the wavelength of the incident light, and P denotes the light intensity.

As shown in Figure 3.10, the IPCE values in the visible region reveal a significant plasmon-enhanced IPCE band, with the maximum value observed for the ATTA structure with a 5.0 nm-thick Ti film. These results indicate that the insertion of a 5.0 nm-thick Ti film at the Au NDs/TiO_2 interface notably facilitates plasmon-enhanced photocurrent conversion in the experimental conditions investigated.

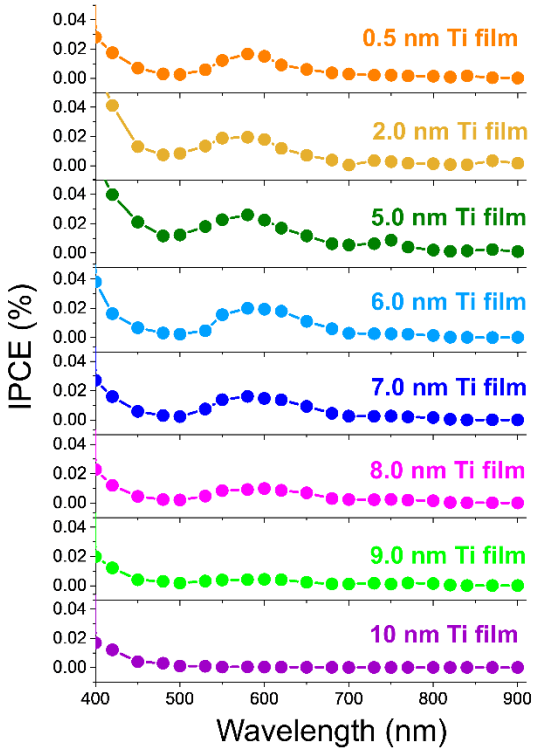

Figure 3.10 The IPCE action spectra of the ATTA structures were measured as a function of Ti film thickness using a three-electrode system.

3.3.4 Influence of excitation wavelength on electron injection

In typical plasmonic systems, such as Au/ TiO_2 without a Ti layer, increased damping generally leads to a reduction in near-field enhancement, which negatively impacts electron generation and transfer from Au to TiO_2.[23, 24] However, in the ATTA system, the efficiency of electron transfer into TiO_2 increased despite the increased damping. This observation suggests that beyond the damping effects, the presence of the Ti film at the Au NDs/TiO_2 interface plays a pivotal role in enhancing the apparent quantum efficiency (AQE) of electron injection.

We hypothesize that energy is transferred from the Au NDs to the Ti film, inducing electronic transitions in the Ti layer, which subsequently injects electrons into TiO_2. To test this hypothesis, TA measurements were performed by pumping the Ti-film (5.0 nm)-ATTA structure at different wavelengths. Figure 3.11 presents the ΔOD_{max} as a function of pump laser wavelength (red curve), superimposed on the absorption spectrum (black curve). Notably, the ΔOD_{max} data closely match the shape of the absorption spectrum, displaying two distinct bands near 600 nm and 770 nm. The

slightly lower ΔOD_{max} at approximately 770 nm is attributed to the reduced photon energy at the lower branch. These findings corroborate our hypothesis that energy transfer occurs from the Au NDs to the Ti film, followed by electron transfer into TiO_2.

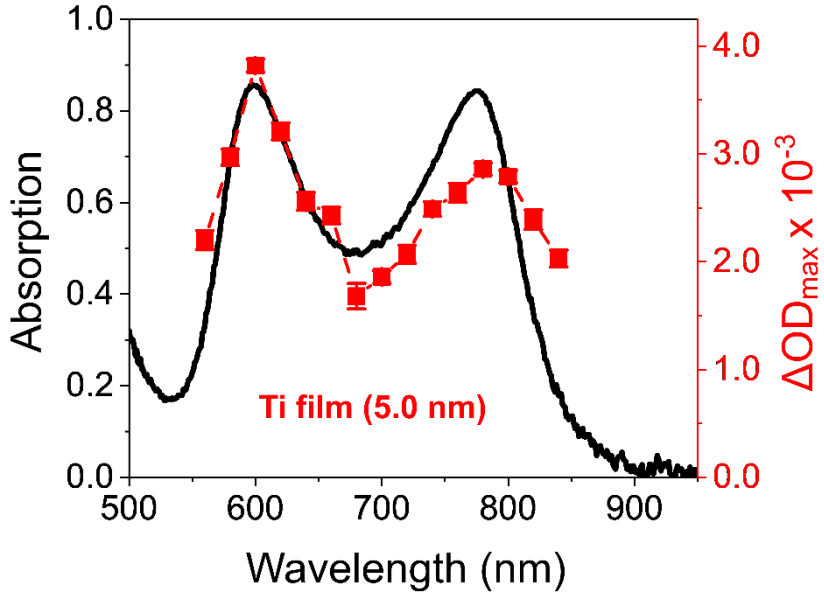

Figure 3.11 ΔOD_{max} as a function of different pump wavelengths of Ti (5.0 nm)-ATTA. The absorption spectrum was also superposed.

3.3.5 Effect of SiO_2 film thickness on electron injection

To further elucidate the mechanism of energy transfer from the Au NDs to the Ti layer, a strong coupling Au ND/SiO_2/Ti/TiO_2 (ASTTA) structure was designed. In this configuration, a SiO_2 film of variable thickness (0-7 nm) was introduced at the interface between the Au NDs and the 5.0 nm-thick Ti film. Acting as an insulating layer, the SiO_2 film effectively blocks direct electron transfer between the Au NDs and the Ti layer while permitting energy transfer across its thickness. This design enables the investigation of the energy transfer process independent of direct electron exchange.

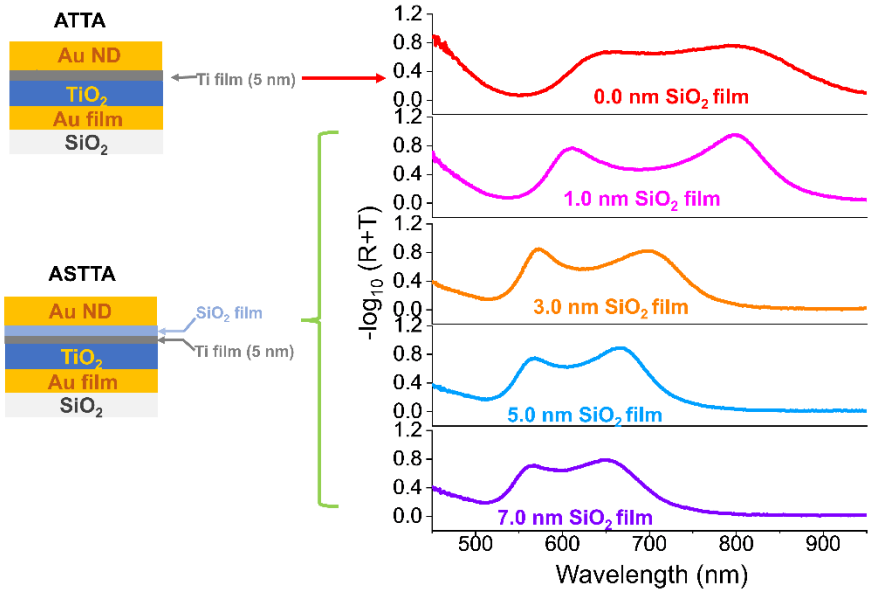

Figure 3.12 Absorption spectra of ATTA structures with varying SiO_2 film at Au NDs/5 nm-thick Ti film interfaces.

Figure 3.12 shows the absorption spectra of ASTTA structures with varying SiO_2 film thicknesses. All ASTTA structures are controlled to be the tuning condition, and showed two distinct absorption bands. Following the strong coupling condition confirmation described above, the values of E_{spl} and $\sqrt{\frac{\gamma_{UB}^2}{2}+\frac{\gamma_{LB}^2}{2}}$ were obtained from each sample from Figure 3.13. As summarized in Table3, the strong coupling condition $E_{spl} > \sqrt{\frac{\gamma_{UB}^2}{2}+\frac{\gamma_{LB}^2}{2}}$ was satisfied for all the structures employed in the present experiment.

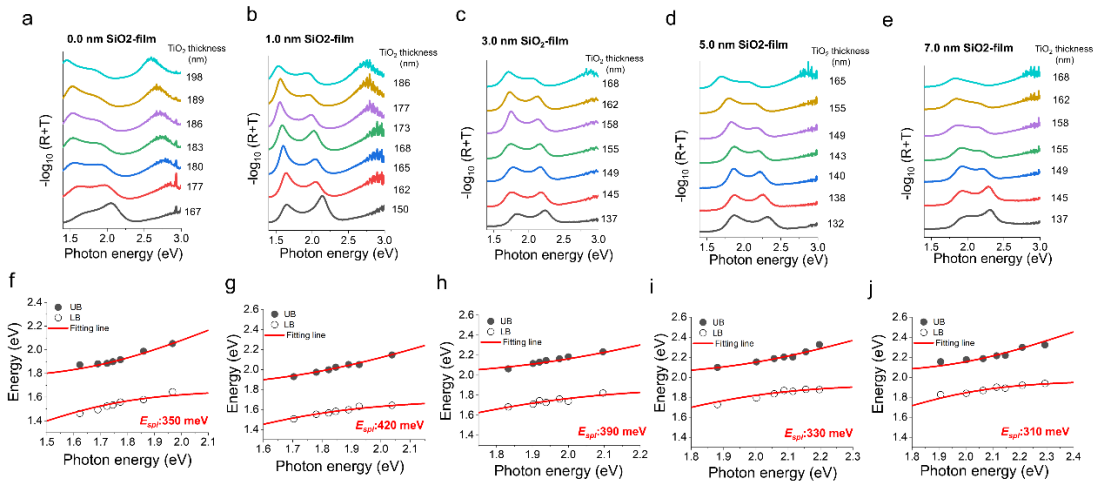

Figure 3.13 Absorption of ASTTA structures with 0.0-7.0 nm (a)-(e) SiO_2 film as a function of TiO_2 film. Dispersion curves of hybrid modes in the ASTTA structures with

0.0-7.0 nm SiO_2 film (f)-(j). E_{spl} were determined from their absorption spectra in (a)-(e). The red line shows the fit using the harmonic oscillator model.

Table 3. The E_{spl} and linewidth of the absorption bands in Figure 3.12 determine that the structure fulfils the strong coupling condition.

SiO_2-layer	E_{spl}(eV)	γ_{UB}(eV)	γ_{LB}(eV)	$\sqrt{(\gamma_{UB}^2+\gamma_{LB}^2)/2}$ (eV)
0.0 nm	0.35	0.29	0.33	0.31
1.0 nm	0.42	0.23	0.17	0.20
3.0 nm	0.39	0.22	0.20	0.21
5.0 nm	0.33	0.21	0.23	0.22
7.0 nm	0.31	0.26	0.25	0.26

Figure 3.14 presents the time profiles of TA measurements performed on the ASTTA structure, excited at the UB and LB, respectively. The experimental data were fitted using the same model described in Figure 3.7, with the fitting curves superimposed on the plots. Analysis of the transient response reveals a clear trend: the intensity of the transient signal decreases as the SiO_2 film thickness increases. This observation suggests that the SiO_2 film modulates the energy transfer efficiency between the Au NDs and the Ti layer.

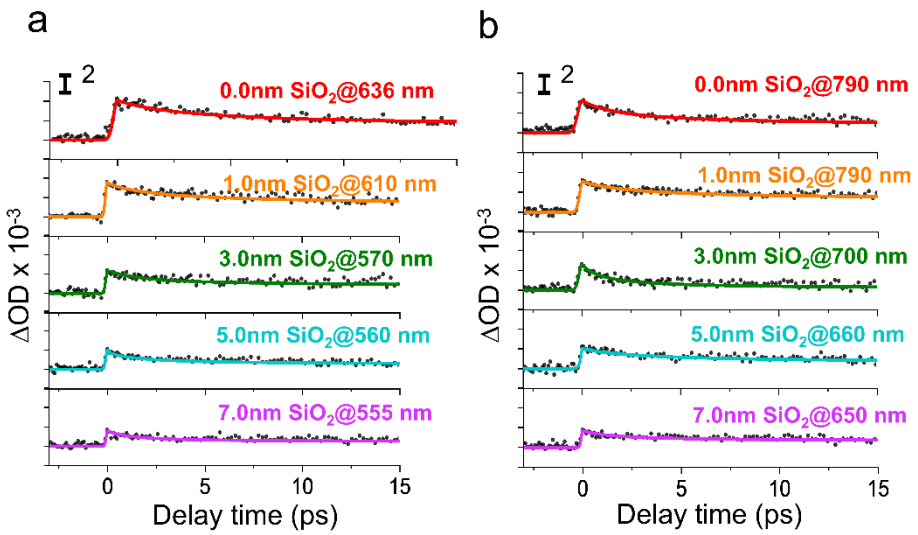

Figure 3.14 Time profiles of TA measurements performed for the UB (a) and LB (b) of the samples after adding the SiO_2 film at the Au ND/Ti film interface. The inserted scale bar in (a) and (b) indicated ΔOD of 2×10^{-3}.

Table 4 Fit ΔOD_{max} of the hot-electron decay curves shown in Figure 3.14 to the fitting mode of Equation 3.1

SiO_2 film	0.0 nm	1.0 nm	3.0 nm	5.0 nm	7.0 nm
ΔOD_{max}_UB	4.5	3.6	2.3	2.0	1.6
ΔOD_{max}_LB	3.3	3.1	2.5	2.0	1.7

To investigate the effect of the SiO_2 film on the AQE of electron injection, we analyzed the decay curves to determine the values of ΔOD_{max}, which are summarized in Table 4. These ΔOD_{max} values were subsequently used to calculate the AQE via the formula $\Delta OD_{max}/n/A$. For clearer comparison, the normalized AQE (N-AQE) was derived by dividing all AQE values by the AQE of the SiO_2 (7.0 nm)-ASTTA structure and plotting the N-AQE as a function of the SiO_2 layer thickness, as shown in Figure 3.15. These results indicate that the N-AQE decreases as the SiO_2 film thickness increases from 0.0 to 7.0 nm. Notably, signals corresponding to electron injection into TiO_2 were detected even when a SiO_2 film up to 7.0 nm thick was introduced at the Au ND/Ti interface.

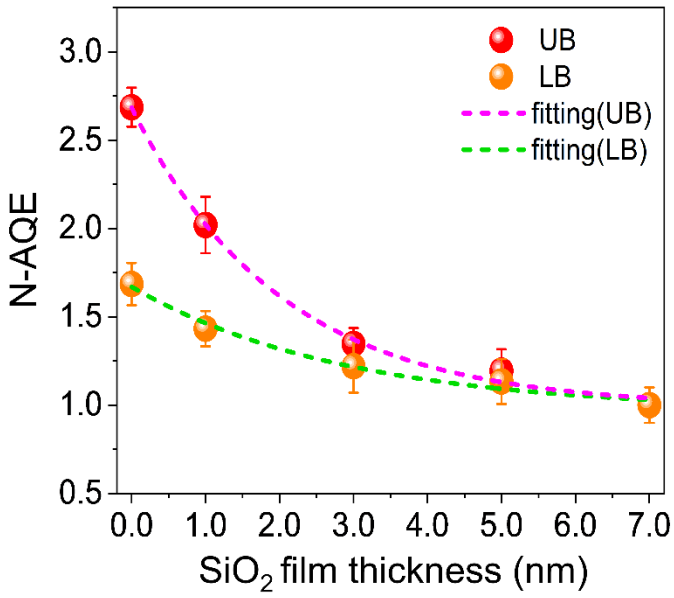

Figure 3.15 N-AQE as a function of the SiO_2 thickness. Red points indicate ASTTA pumped at the UB, and orange points indicate ASTTA pumped at the LB. Dashed lines are exponential fittings.

Typically, electron transfer through a SiO_2 film several nanometers thick is highly improbable.[25] Thus, direct electron transfer from photoexcited Au NDs to the Ti film or TiO_2 in the ASTTA structure is unlikely. This observation implies that energy transfer, rather than direct electron transfer, plays a crucial role in facilitating electron injection into TiO_2. We propose that the electron injection observed, even with the SiO_2 film at the Au ND/Ti interface, results from energy transfer from Au NDs to the Ti film through near-field. This energy transfer excites electrons within the Ti film, which are then injected into TiO_2. To test this hypothesis, we fitted the AQE variation with SiO_2 thickness using an exponential decay model, a standard approach to describing energy attenuation. As shown by the dashed curves in Figure 3.15, the excellent agreement between the fitted model and the experimental data strongly supports the conclusion that electron injection is closely correlated with energy transfer.

3.3.6 Effect of Ti film thickness on energy absorption calculation

As discussed above, the Ti film-enhanced electron transfer mechanism, attributed to energy transfer from Au NDs to the Ti film through the near-field, was further examined using FDTD simulations. The schematic of the simulation model is illustrated in Figure 3.16a. To specifically evaluate energy absorption in the Ti film, a 3D energy absorption detector was designed to exclusively monitor the Ti film. The energy absorption spectra for Ti films in ASTTA structures with varying SiO_2 film thicknesses are presented in Figure 3.16b.

To assess the impact of SiO_2 film thickness on energy absorption in the Ti film, the peak absorption values at the UB and LB were plotted as a function of SiO_2 thickness (Figure 3.16c). The results reveal that energy absorption by the Ti film at both the UB and LB decreases as the SiO_2 thickness increases, a trend consistent with the N-AQE data shown in Figure 3.15. This suggests that the suppression of energy transfer by thicker SiO_2 films arises from near-field attenuation at the Au ND surface due to the increased distance between the Au NDs and Ti film.

Notably, the absorption at the LB was higher than at the UB, in contrast to the N-AQE, which was more pronounced at the UB. This difference can be attributed to the

higher photon energy at the UB, which generates hot electrons with greater energy, leading to more efficient transfer into TiO_2. For further comparison, the energy absorption at the UB and LB was normalized to the corresponding values for the SiO_2 (7 nm)-ASTTA structure, as shown in Figure 3.16d. The normalized energy absorption at the UB exhibited a more rapid decrease compared to the LB, mirroring the trend observed in the N-AQE data in Figure 3.15. This alignment reinforces the correlation between energy absorption and electron injection efficiency.

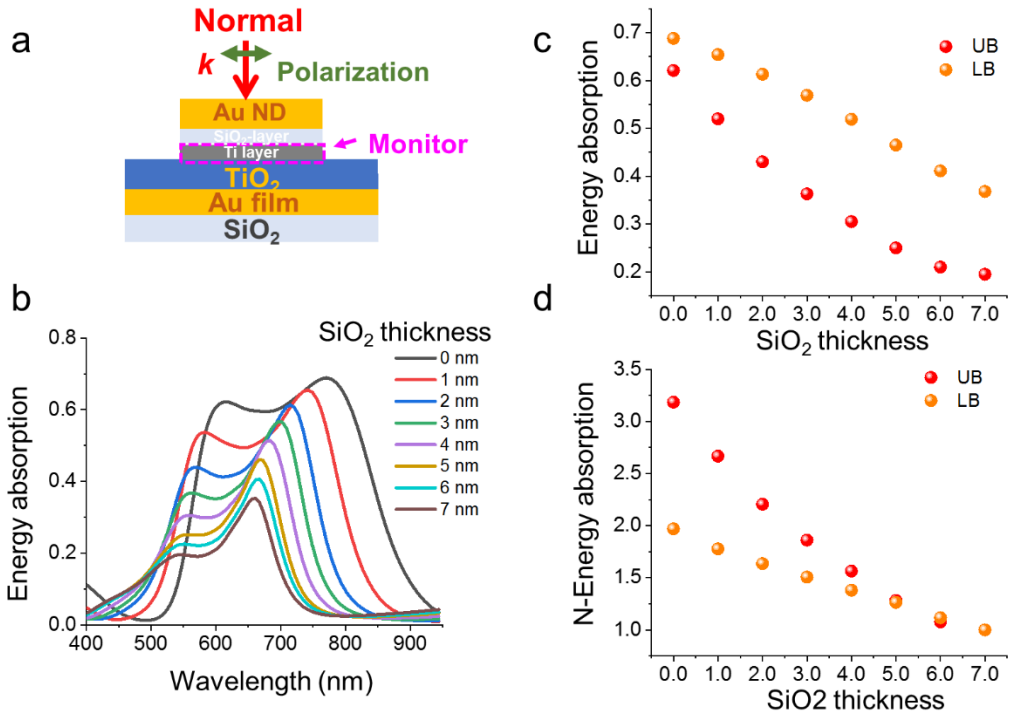

Figure 3.16 (a) Schematic of the simulation model used to calculate the energy absorption in the Ti film. (b) Energy absorption spectra for the Ti film in the ASTTA structure with varying SiO_2 thicknesses, plotted against wavelength. (c) Energy absorption values and (d) normalized energy absorption (N-energy absorption) derived from (b) for different SiO_2 thicknesses. Red and orange points correspond to the absorption at the shorter and longer absorption peaks, respectively. The absorption values are normalized by dividing by the minimum energy absorption value for the SiO_2 (7.0 nm)-ASTTA structure. The UB and LB denote the upper and lower branches of the coupling modes, respectively.

3.3.7 The mechanism of Ti film-enhanced electron injection

Based on our transient measurement experiments on the ATTA and ASTTA structures, we conclude the mechanism of energy transfer from Au NDs to the Ti film as follows:

Upon excitation of Au NDs under modal strong coupling conditions, a strong near-field is generated, facilitating the transfer of energy from the Au NDs to the Ti film through the near-field. This energy transfer excites electron transitions within the Ti film. The excited electrons in the Ti film, with sufficient energy, are then injected into the CB of TiO_2. Subsequently, a portion of these injected electrons undergo recombination following a second-order reaction model, indicating electron recombination with holes either in Ti or at the Ti/TiO_2 interface, as illustrated in Figure 3.17. Notably, in the ATTA system, where the Au ND directly contacts Ti, besides energy transfer via the near-field, plasmon-induced direct electron transitions at the Au ND/Ti interface could also contribute as an additional mechanism that enhances electron transfer efficiency.

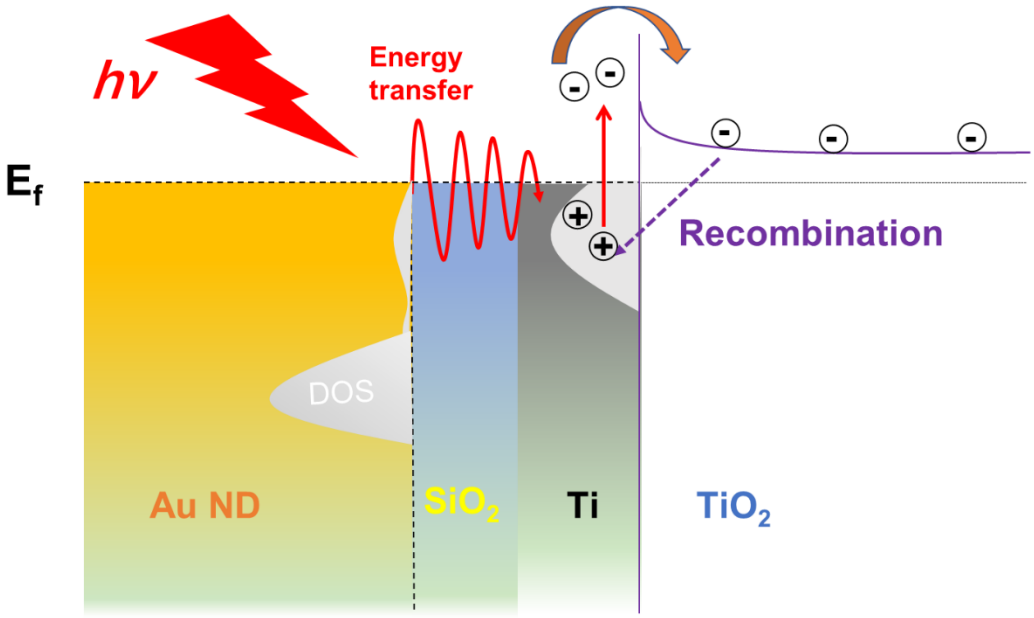

Figure 3.17 Schematic indication of the energy transfer from Au ND to the Ti film through the near-field in enhancing the AQE. The light grey color region schematically indicates the density of states (DOS) of Au and Ti.

The observed enhancement in AQE in the ATTA structure can be attributed to the distinct density of states (DOS) in Au and Ti. In Au plasmonic nanostructures, efficient hot carrier generation is typically dominated by the direct transition from the d-band to unoccupied states above the Fermi level, facilitated by LSPR dipole mode excitation.[26] However, the d-band in Au is located 2.4 eV below the Fermi level, which limits the

generation of high-energy electrons. In contrast, Ti possesses a larger DOS in its d-band, as well as in the s- and p-bands near the Fermi level.[27] This enables more efficient high-energy hot electron generation compared to Au, as electron transitions can be excited from shallow states below the Fermi level.

In the ATTA structure, the Ti-induced plasmon damping enhances energy transfer from the Au NDs to the Ti film via the near-field. This transfer excites high-energy electrons more efficiently than in Au NDs alone, contributing to the observed AQE enhancement for Ti films with thicknesses of less than 5 nm. However, for Ti film thicknesses greater than 5 nm, the increased distance between Ti and TiO_2 reduces the efficiency of electron transfer to TiO_2, leading to a decrease in AQE despite the increase in Ti-induced damping. This indicates an optimal Ti film thickness for maximizing electron transfer and AQE in the ATTA structure.

3.4 Conclusions

In this study, we proposed a strategy to enhance electron transfer by modifying the interface under modal strong coupling conditions and investigated its underlying mechanism. Specifically, we incorporated a thin Ti film at the Au ND/ TiO_2 interface within the ATTA structure. Upon excitation of the Au NDs, energy was transferred to the Ti film through the near-field, generating high-energy electrons within the Ti film that were subsequently injected into the CB of TiO_2. We observed that the efficiency of photoexcited electron transfer to TiO_2 increased by approximately 1.8-fold when a 5 nm Ti film was present at the Au ND/TiO_2 interface, compared to a 0.5 nm Ti film. Near-field simulations performed using FDTD further confirmed the energy transfer from the Au NDs to the Ti film. This approach of enhancing high-energy hot carrier generation through interfacial modification offers a promising strategy for the rational design of multicomponent plasmonic devices, with potential applications in solar energy conversion.

3.5 References

[1] Atwater, H. A.; Polman, A. Plasmonics for improved photovoltaic devices. *Nat. Mater.* **2010**, *9*, 205-213.

[2] Brongersma, M. L.; Halas, N. J.; Nordlander, P. Plasmon-induced hot carrier science and technology. *Nat. Nanotechnol.* **2015**, *10*, 25-34.

[3] Tan, S.; Argondizzo, A.; Ren, J.; Liu, L.; Zhao, J.; Petek, H. Plasmonic coupling at a metal/semiconductor interface. *Nat. Photonics* **2017**, *11*, 806-812.

[4] Sobhani, A.; Knight, M. W.; Wang, Y.; Zheng, B.; King, N. S.; Brown, L. V.; Fang, Z.; Nordlander, P.; Halas, N. J. Narrowband photodetection in the near-infrared with a plasmon-induced hot electron device. *Nat. Commun.* **2013**, *4*, 1643.

[5] Li, W.; Valentine, J. Metamaterial perfect absorber based hot electron photodetection. *Nano Lett.* **2014**, *14*, 3510-3514.

[6] Chalabi, H.; Schoen, D.; Brongersma, M. L. Hot-electron photodetection with a plasmonic nanostripe antenna. *Nano Lett.* **2014**, *14*, 1374-1380.

[7] Knight, M. W.; Sobhani, H.; Nordlander, P.; Halas, N. J. Photodetection with active optical antennas. *Science* **2011**, *332*, 702-704.

[8] Li, W.; Valentine, J. G. Harvesting the loss: surface plasmon-based hot electron photodetection. *Nanophotonics* **2017**, *6*, 177-191.

[9] Cushing, S. K.; Wu, N. Progress and perspectives of plasmon-enhanced solar energy conversion. *J. Phys. Chem. Lett.* **2016**, *7*, 666-675.

[10] Ueno, K.; Oshikiri, T.; Sun, Q.; Shi, X.; Misawa, H. Solid-state plasmonic solar cells. *Chem. Rev.* **2017**, *118*, 2955-2993.

[11] Jang, Y. H.; Jang, Y. J.; Kim, S.; Quan, L. N.; Chung, K.; Kim, D. H. Plasmonic solar cells: from rational design to mechanism overview. *Chem. Rev.* **2016**, *116*, 14982-15034.

[12] Clavero, C. Plasmon-induced hot-electron generation at nanoparticle/metal-oxide interfaces for photovoltaic and photocatalytic devices. *Nat. Photonics* **2014**, *8*, 95-103.

[13] Tian, Y.; Tatsuma, T. Mechanisms and applications of plasmon-induced charge separation at TiO2 films loaded with gold nanoparticles. *J. Am. Chem. Soc.* **2005**, *127*, 7632-7637.

[14] Tian, Y.; Tatsuma, T. Plasmon-induced photoelectrochemistry at metal

nanoparticles supported on nanoporous TiO_2. *Chem. commun.* **2004**, 1810-1811.

[15] Furube, A.; Du, L.; Hara, K.; Katoh, R.; Tachiya, M. Ultrafast plasmon-induced electron transfer from gold nanodots into TiO_2 nanoparticles. *J. Am. Chem. Soc.* **2007**, *129*, 14852-14853.

[16] Nishijima, Y.; Ueno, K.; Yokota, Y.; Murakoshi, K.; Misawa, H. Plasmon-assisted photocurrent generation from visible to near-infrared wavelength using a Au-nanorods/TiO_2 electrode. *J. Phys. Chem. Lett.* **2010**, *1*, 2031-2036.

[17] Nishijima, Y.; Ueno, K.; Kotake, Y.; Murakoshi, K.; Inoue, H.; Misawa, H. Near-infrared plasmon-assisted water oxidation. *J. Phys. Chem. Lett.* **2012**, *3*, 1248-1252.

[18] Shi, X.; Ueno, K.; Takabayashi, N.; Misawa, H. Plasmon-enhanced photocurrent generation and water oxidation with a gold nanoisland-loaded titanium dioxide photoelectrode. *J. Phys. Chem. C* **2013**, *117*, 2494-2499.

[19] Shi, X.; Ueno, K.; Oshikiri, T.; Sun, Q.; Sasaki, K.; Misawa, H. Enhanced water splitting under modal strong coupling conditions. *Nat. Nanotechnol.* **2018**, *13*, 953-958.

[20] Liu, Y.-E.; Shi, X.; Yokoyama, T.; Inoue, S.; Sunaba, Y.; Oshikiri, T.; Sun, Q.; Tamura, M.; Ishihara, H.; Sasaki, K. Quantum-coherence-enhanced hot-electron injection under modal strong coupling. *ACS Nano* **2023**, *17*, 8315-8323.

[21] Suganami, Y.; Oshikiri, T.; Shi, X.; Misawa, H. Water oxidation under modal ultrastrong coupling conditions using gold/silver alloy nanoparticles and Fabry–Pérot nanocavities. *Angew. Chem. Int. Ed.* **2021**, *60*, 18438-18442.

[22] Furube, A.; Asahi, T.; Masuhara, H.; Yamashita, H.; Anpo, M. Charge carrier dynamics of standard TiO_2 catalysts revealed by femtosecond diffuse reflectance spectroscopy. *J. Phys. Chem. B* **1999**, *103*, 3120-3127.

[23] Ingram, D. B.; Linic, S. Water splitting on composite plasmonic-metal/semiconductor photoelectrodes: evidence for selective plasmon-induced formation of charge carriers near the semiconductor surface. *J. Am. Chem. Soc.* **2011**, *133*, 5202-5205.

[24] Zheng, B. Y.; Zhao, H.; Manjavacas, A.; McClain, M.; Nordlander, P.; Halas, N. J. Distinguishing between plasmon-induced and photoexcited carriers in a device geometry. *Nat. Commun.* **2015**, *6*, 7797.

[25] Cushing, S. K.; Li, J.; Meng, F.; Senty, T. R.; Suri, S.; Zhi, M.; Li, M.; Bristow, A. D.; Wu, N. Photocatalytic activity enhanced by plasmonic resonant energy transfer from metal to semiconductor. *J. Am. Chem. Soc.* **2012**, *134*, 15033-15041.

[26] Brown, A. M.; Sundararaman, R.; Narang, P.; Goddard III, W. A.; Atwater, H. A. Nonradiative plasmon decay and hot carrier dynamics: effects of phonons, surfaces, and geometry. *ACS Nano* **2016**, *10*, 957-966.

[27] Li, F.; Zou, Y.; Han, M.-G.; Foyevtsova, K.; Shin, H.; Lee, S.; Liu, C.; Shin, K.; Albright, S. D.; Sutarto, R. Single-crystalline epitaxial TiO film: A metal and superconductor, similar to Ti metal. *Sci. Adv.* **2021**, *7*, eabd4248.

Chapter 4

Activation energy in the electron transfer process and water oxidation intermediate generation under plasmon-nanocavity strong coupling

4.1 Introduction

Titanium dioxide (TiO_2) supported by gold nanoparticles (Au NPs) has gained significant attention as a strategy to enhance the efficiency of photochemical water splitting under visible light, driven by the localized surface plasmon resonance (LSPR) of Au NPs.[1-6] To further optimize this system, we recently developed a strong coupling electrode structure comprising a TiO_2 film deposited on an Au reflective film, with Au NPs positioned on top (Au NPs/TiO_2/Au film: ATA), achieving modal strong coupling between the LSPR of Au NPs and nanocavity of TiO_2/Au film modes.[7] Compared to the conventional Au NPs/TiO_2 (AT) structure without nanocavity, ATA structure demonstrates a remarkable improvement in visible-light absorption intensity and an expanded absorption spectrum. These enhancements make ATA more effective as photoanode, significantly increasing the quantum efficiency of water oxidation.[7-9] Furthermore, the enhanced quantum efficiency of water oxidation under strong coupling condition is attributed to increased electron injection efficiency facilitated by quantum coherence among Au NPs through the nanocavity.[10]

Regarding the subsequent reaction between hot holes and water, although precursors of oxygen evolution, such as water oxidation intermediates, during the water reactions have been detected using surface-enhanced Raman scattering (SERS) measurements,[11, 12] research on the kinetic aspects of intermediate generation and their associated activation is limited. In plasmonic water oxidation reaction using ATA and AT structures, hot holes generated at the continuous energy levels of Au at the Au NPs/TiO_2 interface are thought to be trapped at TiO_2 surface states before participating in water oxidation. This mechanism differs from conventional photooxidation reactions in molecular systems, which typically involve electron transfer from water to discrete energy level.

Instead, the plasmon-induced process operates through continuous energy states, necessitating kinetics studies to clarify the relationship between the energy levels of holes and oxidation potential of water.

In this study, we fabricated a LSPR- Fabry–Pérot nanocavity strong coupling system consisting of Au NPs, TiO_2, and an Au reflective film (ATA) to explore the activation energy of electrons injection into TiO_2 and the generation of water oxidation intermediates. Temperature-dependent transient absorption (TA) measurements were conducted to evaluate the activation energy for electron-hole recombination, shedding light on the electron transfer processes within TiO_2. To further verify the activation energy associated with water oxidation intermediates, temperature-dependent incident photon-to-current conversion efficiency (IPCE) measurements were used to calculate the activation energy for photocurrent generation. By analyzing these results, the electrochemical potential levels of holes trapped at the surface states of the Au/TiO_2 interface were compared for both the ATA and Au NPs/TiO_2 (AT) systems, offering insights into the mechanisms driving water oxidation reactions.

4.2 Experimental details

4.2.1 ATA and AT structure fabrication

As shown in Figure 4.1, the ATA structures were fabricated on 10×10×1 mm^3 silica (SiO_2) substrates. The substrates were sequentially cleaned in an ultrasonic bath using acetone, methanol, and ultrapure water for 5 minutes each, followed by drying with pure nitrogen flow. A helicon sputtering system (MPS-4000C1/HC1, ULVAC) was used to deposit a 2 nm-thick titanium (Ti) film, followed by a 100 nm-thick gold (Au) film onto the cleaned substrates. Subsequently, a 30 nm-thick TiO_2 film was deposited onto the Au film at 300^oC using an atomic layer deposition (ALD) reactor (SUMALE R series, Picosun), forming a Fabry–Pérot (F-P) nanocavity. The ALD process utilized titanium tetrachloride ($TiCl_4$) as the precursor and deionized water for the reaction. A 4 nm-thick Au film was then evaporated onto the TiO_2 film at a deposition rate of 0.2 Å/s using a vacuum evaporator. The samples were annealed at 300^oC for 2 hours to facilitate

the formation of Au nanoparticles (Au NPs). To embed Au NPs within the TiO_2 layer, an additional 7 nm-thick TiO_2 film was deposited onto the ATA structure using ALD. For comparison, an indium-doped tin oxide (ITO) substrate ($10 \times 10 \times 0.7$ mm^3) was used to fabricate the AT structure without the Au film, serving as a control group. The cleaning and fabrication conditions for the 30 nm-thick TiO_2 film with Au NPs on the AT structure were identical to those used for the ATA structure.

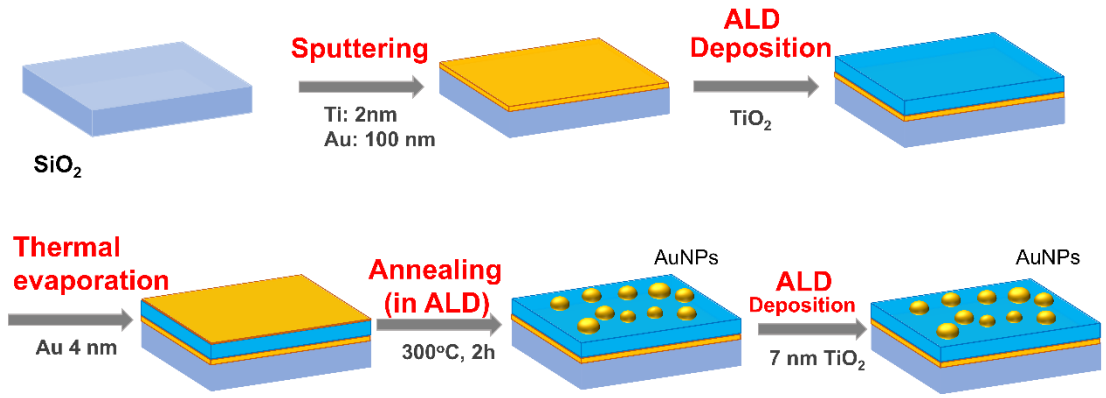

Figure 4.1 The schematic of ATA structure fabrication.

4.2.2 Transient absorption measurements

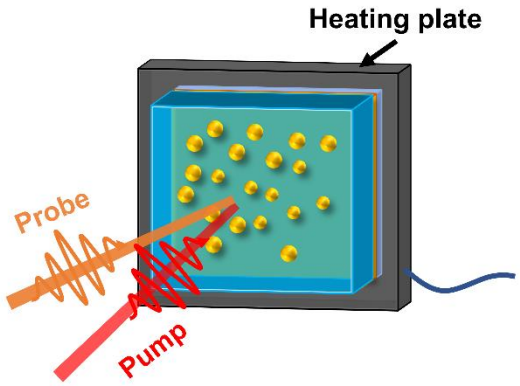

Figure 4.2 The schematic temperature-dependent transient absorption measurements.

As illustrated in Figure 4.2, the samples were mounted in a temperature-controlled sample holder with an accuracy of ±1°C. Transient absorption (TA) measurements were performed using the pump-probe method described in Chapter 3, with the key modification of using 1500 nm laser pulses to probe the transient signals. Furthermore,

to ensure consistent transient reflection measurement configurations between the ATA and AT structures, a 100 nm-thick silver film was deposited on the backside of the AT structure, which lacks the Au film, specifically for the TA measurements.

4.2.3 Photoelectrochemical measurements

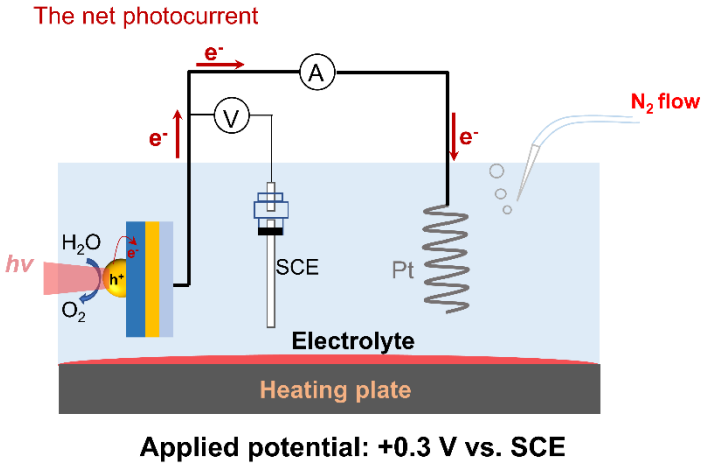

Figure 4.3 Schematic of the three-electrode photoelectrochemical cell for the IPCE measurement.

Temperature dependence IPCE measurements on ATA and AT were performed using an electrochemical analyzer station (CHI660E) with a three-electrode system, as shown in Figure 4.3. An In-Ga alloy film (weight ratio 2:1) was applied to the backside and sidewalls of the substrate to establish ohmic contact and connected to an electrochemical analyzer via a copper lead wire. A saturated calomel electrode (SCE) and a platinum wire were used as the reference and counter electrodes, respectively. 0.1 mol/dm³-potassium hydroxide (KOH) with and without the addition of triethanolamine (TEOA) served as the supporting electrolyte for the IPCE measurements. To eliminate dissolved oxygen, the electrolyte solution was continuously purged with nitrogen gas for 1 hour before the measurements. An 800 W xenon lamp was employed as the excitation light source, with the irradiation wavelength precisely selected using a bandpass filter with a full width at half maximum (FWHM) of less than 15 nm. Throughout the IPCE measurements, the working electrode potential was maintained at +0.3 V versus the SCE.

4.3 Results and discussion

4.3.1 Characterization of morphology and far-field spectra

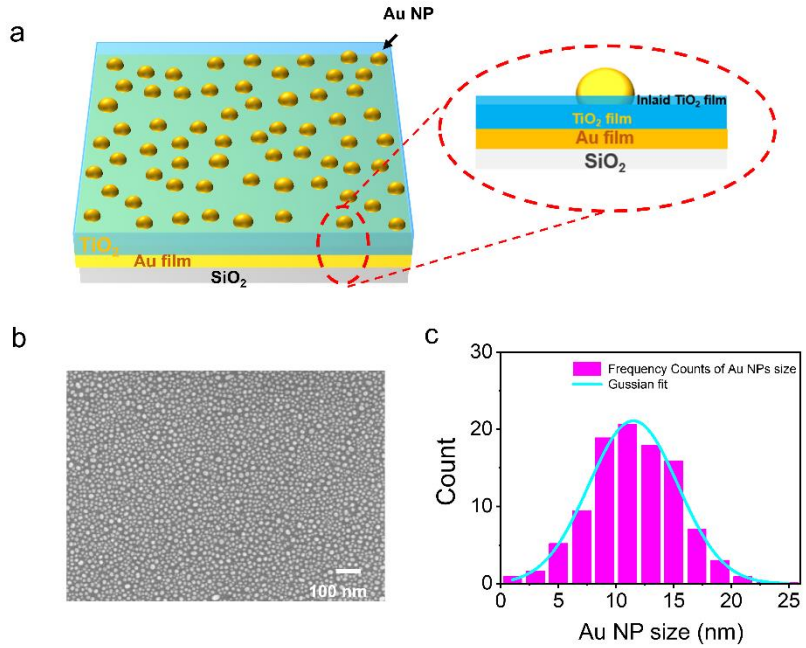

Figure 4.4 (a) Schematic diagram of the ATA structure with cross-sectional view of the ATA structure consisting of Au NP, TiO_2 film, and 100 nm Au film. (b) Top-view SEM images of typical ATA structure. (c) Histogram of Au ND diameter with Gaussian fit shown as cyan line. The average size of the Au NPs was 11.5±4.1 nm.

In this study, ATA and AT structures were fabricated to explore the activation energy of intermediate generation during plasmon-induced water oxidation. The ATA as working electrode structure is illustrated in the schematic diagram provided in Figure 4.4a, with detailed fabrication procedures described in the Methods section. The TiO_2/Au film component in the ATA structure serves as a F-P nanocavity, where the resonance wavelength can be tuned by adjusting the thickness of the TiO_2 film. Au NPs were partially embedded within the TiO_2 film of the F-P nanocavity to a depth of 7 nm. Based on Gaussian fitting analysis of the SEM images (Figures 4.4b and 4.4c), the average diameter of the Au NPs was determined to be approximately 11.5 ± 4.1 nm. Regarding the Au NPs in the AT structure, which were fabricated on an ITO substrate, indicated a similar size distribution.

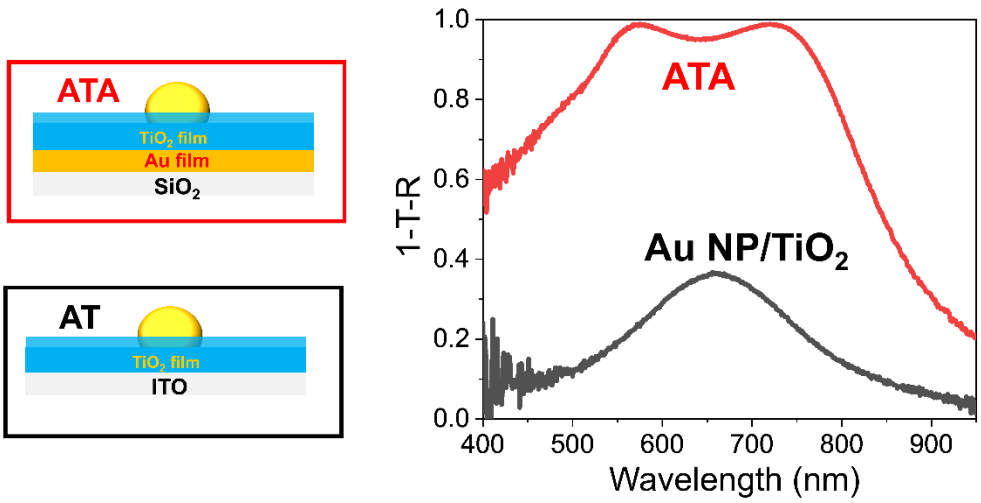

Figure 4.5 The absorption spectra of ATA and AT structure.

Figure 4.5a shows the absorption spectra of ATA and AT by using $1-T-R$. The plasmon band in the AT structure appeared at approximately 600 nm. Because of the strong coupling between the LSPR mode and F-P nanocavity mode, the ATA structure shows distinct dual absorption bands with an upper branch (UB) at around 580 nm and a lower branch (LB) at around 730 nm. It was found that the modal strong coupling ATA structure can efficiently broadens the absorption wavelength range and results in efficient absorption.

To understand the TiO_2 film affects the optical responses, we fabricated the ATA structures with varying thicknesses of the TiO_2 film and compared their absorption spectra, as shown in Figure 4.6a. The absorption spectra of ATA with various TiO_2 film thicknesses were calculated via *–log(T+R)*. Figure 4.6b shows a dispersion curve obtained via plotting the peak energy in absorbance as a function of energy of nanocavity mode. The resonance energy of nanocavity mode were obtained through peak separation using a Lorentzian fitting. From the dispersion curve, the nanocavity mode of the TiO_2/Au film with a 30 nm-thick TiO_2 film closely matched the LSPR mode of the Au NPs forming strong coupling conditions. The splitting energy of tuning structure was calculated to be 380 meV, the strong coupling condition $E_{spl} > \sqrt{\frac{\gamma_{UB}^2}{2}+\frac{\gamma_{LB}^2}{2}}$ was fulfilled by ATA structure investigated in this study.

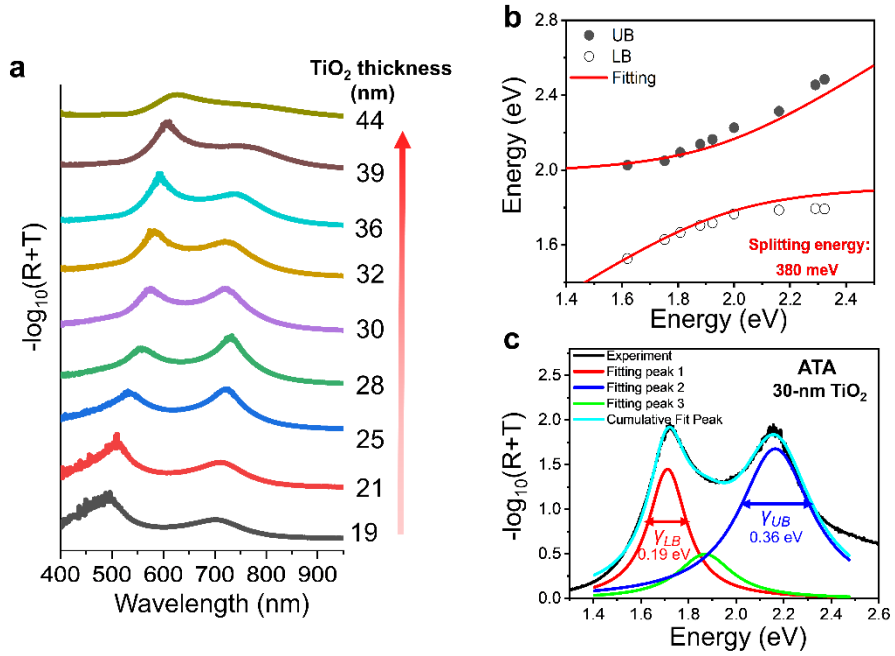

Figure 4.6 (a) Absorption spectra of ATA as a function of TiO_2 film. (b) Dispersion curve of ATA. (c) Spectral separation of the absorption spectrum of tuning ATA (30-nm TiO_2) structure by a Lorentz fitting.

4.3.2 Activation energy of electron-hole recombination in TiO_2

Au NPs-loaded TiO_2 systems have been widely studied for their photochemical reactions involving electron transfer from Au NPs to TiO_2. To investigate the kinetics of electrons injected into TiO_2, we conducted picosecond time-domain TA measurements on ATA and AT structures within the temperature range of 293 K to 353 K. The activation energy for electron-hole recombination ($E_a(\mathrm{r})$), occurring within the initial 20 ps, was evaluated. For the ATA structure, the presence of a 100 nm-thick Au film renders the system nearly opaque, necessitating a reflection-mode configuration for TA measurements. To ensure consistency in transient reflection measurements between ATA and AT structures, a 100 nm-thick Ag film was deposited on the back of the AT structure. Notably, the silver film does not induce a cavity mode or interact with the LSPR of Au NPs.

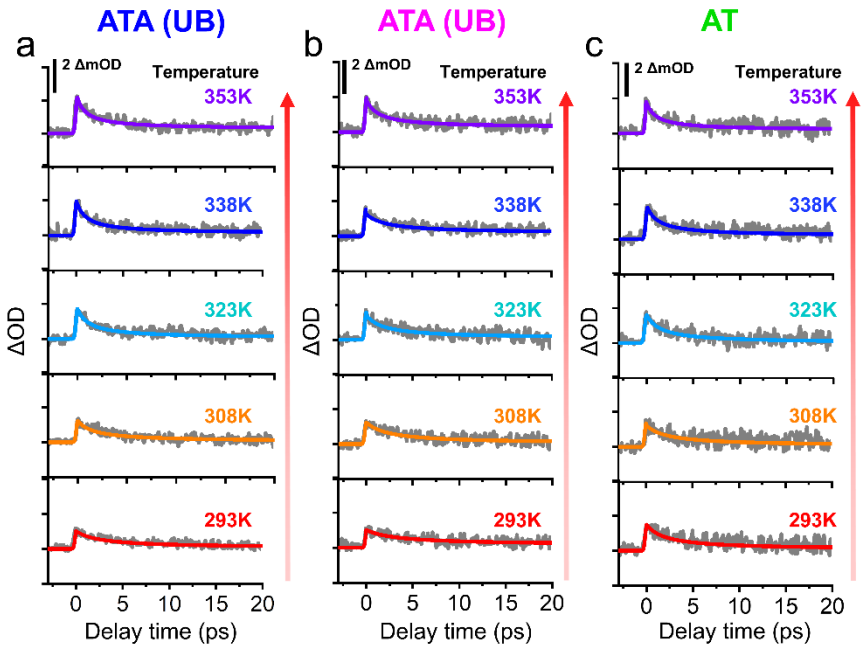

Figure 4.7 Time profiles of the transient measurements pumped at (a) the UB of ATA, (b) the LB of ATA, and (c) the absorption peak of AT under various temperatures. The inset scale bars in (a)–(c) correspond to $2\ \Delta\mathrm{m}OD$, where $\Delta\mathrm{m}OD = \Delta OD \times 10^{-3}$. The pump power was maintained at 0.6 mW, with a 2500 nm laser pulse serving as the probe.

The TA signal, represented in terms of optical density (OD), was calculated using the formula $\Delta\mathrm{OD} = -log_{10}\left(\frac{R}{R_0}\right)$, where R and R_0 correspond to the reflection with and without the pump pulse, respectively. The TA measurements enabled the evaluation of the decay rate constant (k_r) for injected electrons, a key parameter for analyzing their kinetic behavior within TiO_2. Figures 4.7a and 4.7b illustrate the time profiles of the transient signals of ATA structure at various temperatures when excited at the UB and LB, respectively. In contrast, Figure 4.7c presents the transient profiles of the AT structure excited at its absorption peak. To confirm that the decay of injected electrons in the ATA and AT structures follows a second-order reaction model, we performed a comparative analysis of the fitting results over time scales of 20 ps and 100 ps. The results showed highly similar fitting parameters across both intervals, validating the applicability of the model. Consequently, the same second-order reaction model was used to fit the time profiles, as represented by the solid lines superimposed in Figures 4.7a–c.

The electron decay rate constant (k_r) for electron–hole recombination at various

temperatures is summarized in Table 1.

Table 1 Electron-hole recombination rate constants obtained from the fittings presented in Figures 4.7a-c.

	ATA@UB	ATA@LB	AT
Temperature	$k_r[e^-] \pm \Delta k_r[e^-]$ (ps^{-1})	$k_r[e^-] \pm \Delta k_r[e^-]$ (ps^{-1})	$k_r[e^-] \pm \Delta k_r[e^-]$ (ps^{-1})
293 K	401±63	341±123	340±132
308 K	489±70	342±89	365±129
323 K	490±74	399±95	398±40
338 K	504±71	416±131	459±83
353 K	514±64	463±87	589±112

Based on the temperature-dependent k_r shown in Table 1, we found that the decay rate constant of injected electrons increased in both the ATA and AT as the temperature increased from 293 to 353K. The temperature-dependent k_r was then used to determine the activation energy of electron transfer in TiO_2. The activation energy was derived from the logarithmic from of Arrhenius equation:$ln(k_r[e^-]) = ln(k_{r0}[e^-]) - E_a/k_BT$, where k_r, k_{r0}, E_a, $[e^-]$, and T are the electrons decay rate, pre-exponential factor, activation energy, electron number density and absolute temperature, respectively. k_B represents the Boltzmann constant, defined to be about 8.617×10^{-5} eV/K. Based on the k_r estimated from the time profiles of TA measurements under various temperatures, we constructed the Arrhenius plots of $ln(k_r[e^-])$ as a function of $1000/T$, as shown in Figure 4.8. And then, we calculated the activation energy from the slope of these plots ($E_a = -slope \times k_B \times 1000$), and subsequently converted the activation energy from eV to kJ/mol using the Faraday constant. As a result, the $E_a(\mathrm{r})$ in ATA was 3.0±0.8 kJ/mol and 4.9±0.6 kJ/mol when it was pumped at the UB and LB, respectively; the $E_a(\mathrm{r})$ of AT was 8.3±1.9 kJ/mol. It should be noted that the standard error of $E_a(\mathrm{r})$ was calculated from the standard error of the linear fit of the Arrhenius plots.

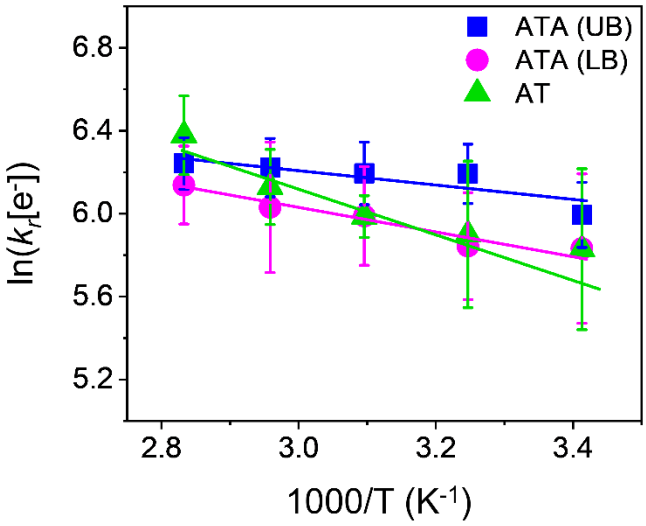

Figure 4.8 Arrhenius plots for the ATA and AT structures. The blue plot and pink plot correspond to the ATA pumped at the UB and LB, respectively, whereas the green plot represents AT. The temperature-dependent electron decay rate constants (k_r) are shown in Table 1. The error bars were calculated by $\Delta k_r/k_r$, where Δk_r and k_r were derived from the fitting of each time profile. Linear fits are superposed on the Arrhenius plots.

Previous studies have reported that electrons in TiO_2 excited by interband transitions from the valence band to the conduction band (CB) are initially trapped at shallow trap sites. These electrons can thermally re-excite back to the CB and recombine with holes.[13, 14] Similarly, in our study, we propose that electrons injected from Au NPs to TiO_2 are also trapped at such sites and recombine with holes via thermal re-excitation into the CB. Consequently, the activation energy for electron-hole recombination, $E_a(\mathrm{r})$, obtained from TA measurements represents the minimum energy required for electrons trapped at these sites to recombine with holes at the surface states of the Au/TiO_2 interface.

Although the $E_a(\mathrm{r})$ values for both ATA and AT are relatively small, the slightly higher value observed in AT is likely due to differences in TiO_2 quality, as the TiO_2 films in these structures were deposited on different substrates. To further study the nature of trap sites in TiO_2, we adjusted the probe laser wavelength in our TA measurements from 2500 nm to 1500 nm. The higher photon energy at 1500 nm (~0.83 eV) compared to 2500 nm (~0.50 eV) enhances the ability to detect electrons trapped at deeper trapped sites. The results of the temperature-dependent TA measurements

using the 1500 nm probe are presented in Figure 4.9.

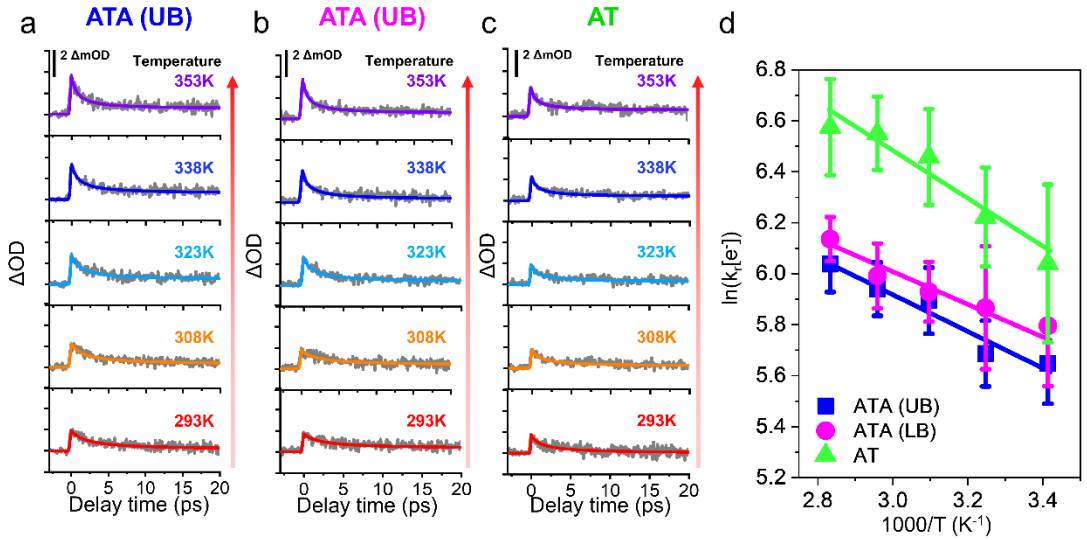

Figure 4.9 Time profiles of the transient measurements pumped at (a) the UB of ATA, (b) the LB of ATA, and (c) the absorption peak of AT at various temperatures. The inserted scale bars in (a)-(c) represent $2\ \Delta\mathrm{m}OD$, where $\Delta\mathrm{m}OD$ denotes $\Delta OD \times 10^{-3}$. The pump power was 0.6 mW, and a 1500 nm laser pulse was used as the probe. (d) Arrhenius plots for the determination of $E_a(\mathrm{r})$ for the ATA and AT structures. The blue plot and pink plot correspond to the ATA pumped at the UB and the ATA pumped at the LB, respectively, whereas the green plot represents the AT. The error bars for each point were calculated as $\Delta k_r/k_r$, where Δk_r and k_r were derived from the fitting of each time profile. The temperature-dependent rate constants (k_r) are shown in Table S1. Linear fits are superposed on the Arrhenius plots.

Table 2. Electron-hole recombination rate constants probed at 1500 nm and obtained from the fittings shown in Figures 4.9a-c.

	ATA@UB	ATA@LB	AT
Temperature	$k_r[e^-] \pm \Delta k_r[e^-]$ (ps^{-1})	$k_r[e^-] \pm \Delta k_r[e^-]$ (ps^{-1})	$k_r[e^-] \pm \Delta k_r[e^-]$ (ps^{-1})
293 K	284±45	329±78	420±130
308 K	295±38	353±85	504±98
323 K	363±47	376±44	638±120
338 K	380±40	400±51	700±101
353 K	419±46	462±40	717±135

From the results summarized in Table 2, the $E_a(\mathrm{r})$ values for the ATA and AT structures were determined based on the temperature-dependent k_r values. For the ATA structure, when probed at 1500 nm, the $E_a(\mathrm{r})$ was calculated to be 5.8±0.7

kJ/mol and 5.3±0.6 kJ/mol when pumped at the UB and LB, respectively. In contrast, $E_a(\mathrm{r})$ value for the AT structure was 7.5±1.2 kJ/mol. A comparison of the $E_a(\mathrm{r})$ values obtained using the 1500 nm and 2500 nm probes were nearly identical. This consistency indicates that the injected electrons in TiO2 are mainly trapped in shallow trap sites.

4.3.3 Activation energy of photocurrent generation

The generation of photocurrents using water as an electron source and the accompanying oxygen production reactions have been widely investigated with Au/TiO_2 heterostructures as working electrodes (photoanodes).[15, 16] The photocurrent was measured by a three-electrode electrochemical system in 0.1 mol/dm^3 KOH, as SCE as the reference electrode, and a platinum wire as the counter electrode. The IPCE of samples were calculated by using a formula described in Chapter 3, as shown in Figure 4.10. It was found that IPCE showed obvious enhanced in ATA system compared to AT without cavity. When the TiO_2 thickness was ~ 30 nm, IPCE reached the maximum value of 1.28%.

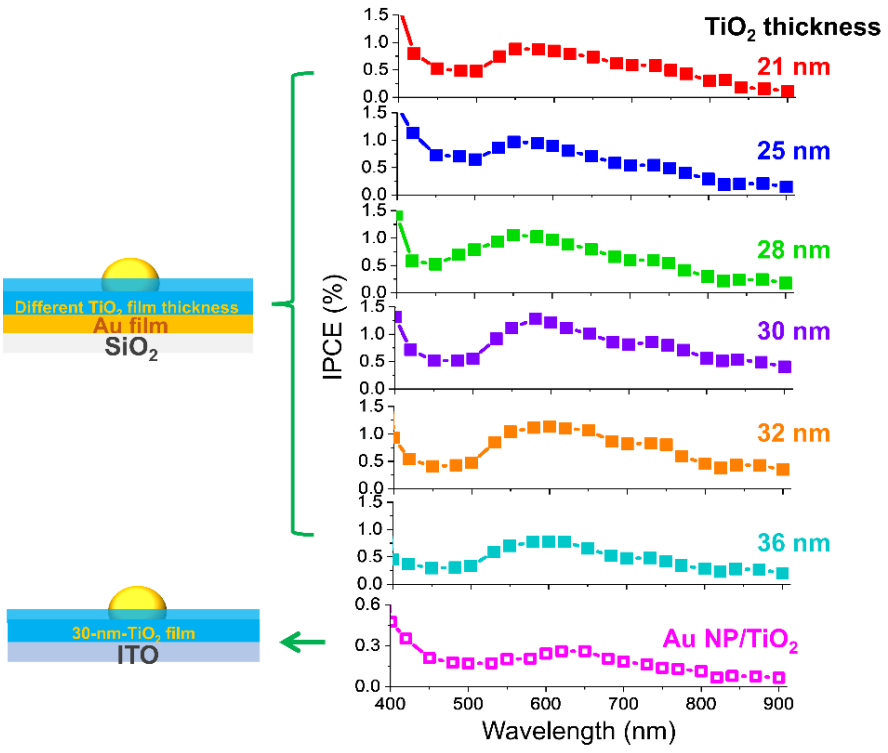

Figure 4.10 IPCE spectra of ATA and AT structures measured in 0.1 mol/dm^3 KOH solution.

Temperature-dependent PEC measurements were conducted on ATA (30-nm TiO_2) and AT structures to determine the activation energy for photocurrent generation (E_a(IPCE)). Figures 4.11a and 4.11b present the IPCE action spectra of ATA and AT structures used as photoanodes at various temperatures. For both structures, the IPCE increased with rising temperatures from 293 K to 353 K. Arrhenius plots were constructed from the temperature-dependent IPCE data to estimate E_a(IPCE), following the same methodology previously used for calculating E_a(r). The E_a(IPCE) values at all measurement wavelengths are summarized in Figure 4.11c.

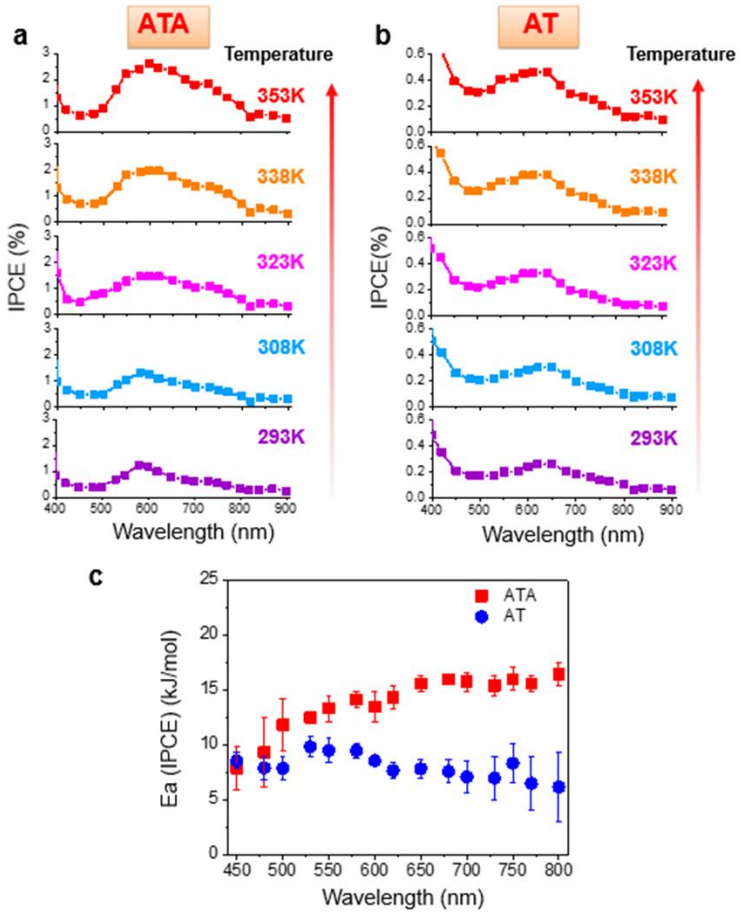

Figure 4.11 IPCE spectra of ATA (a) and AT (b) photoanodes measured at temperatures ranging from 293 to 353 K. (c) Wavelength-dependent E_a(IPCE) for the ATA [17] and AT (blue) photoelectrodes. The scale bar indicates the standards error deviation.

4.3.4 Activation energy of water oxidation intermediates generation

In the case of water splitting, the oxygen evolution reaction is generally considered the rate-determining step.[18] To gain deeper insights into the reaction kinetics of water oxidation intermediate generation, we conducted photoelectrochemical (PEC) measurements at various temperatures using a three-electrode system, focusing on the activation energy for the generation of water oxidation intermediates ($E_a(1)$) with ATA and AT as photoanodes. A schematic illustrating the reaction processes, including electron injection into the TiO_2 layer of AT and ATA structures and hole trapping at surface states at the Au NP/TiO_2 interface, is shown in Figure 4.12. As depicted, hot electrons generated near the Au NP/TiO_2 interface pass through the interface and are injected into TiO_2, where they are rapidly trapped at shallow trap-sites. These trapped electrons are then likely to return to the CB after overcoming a small $E_a(\mathrm{r})$ and recombine either with holes trapped at surface states at the Au NP/TiO_2 interface or with oxidation intermediates produced by the reaction of holes with water or hydroxide ions (OH^-). The rate constants are defined as follows: k_r for the recombination of electrons in the CB with holes, k_1 for the generation of oxidation intermediates by the reaction of water or OH^- with holes, k_r' for electron transfer from the CB to the oxidation intermediates, and k_2 for the subsequent processes following the generation of oxidation intermediates. Note that k_r and k_r' are second-order rate constants, while k_1 and k_2 (which include $[H_2O]/[OH^-]$) are first-order rate constants.

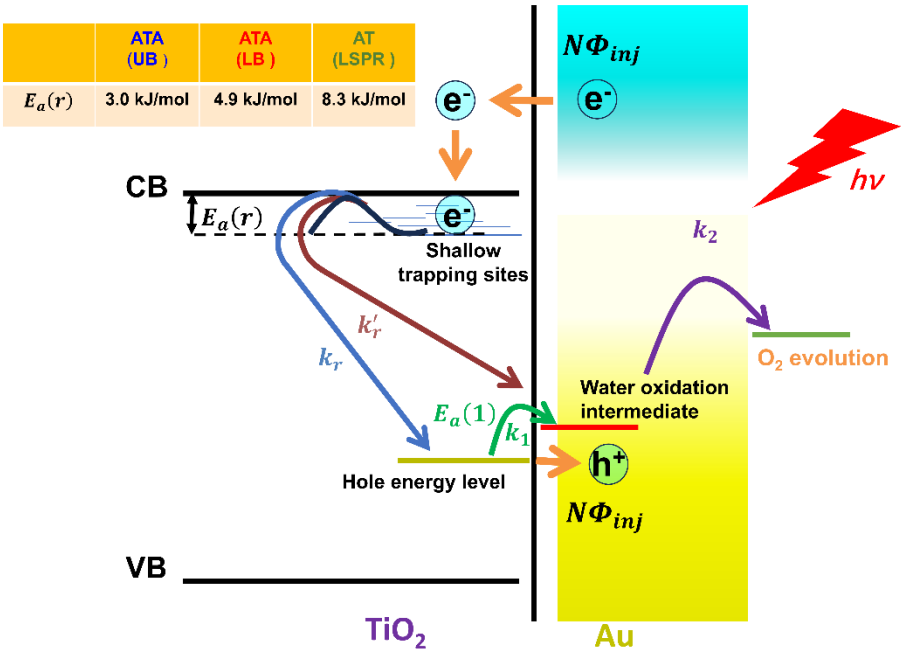

Figure 4.12 Schematic of the reaction processes related to electrons injected into the TiO_2 layer and the holes trapped at surface states at the Au NPs/TiO_2 interface. The parameters k_r, k_r', k_1 and k_2 represent the rate constant for electron–hole recombination, the rate constant for the electron-water oxidation intermediates recombination, the rate constant for the reaction of water oxidation intermediates, and the rate constant for the oxygen evolution from intermediates, respectively. $\boldsymbol{\Phi}_{inj}$ indicates the electron injection efficiency, N represents the number of generated electrons per unit incident light power. $E_a(r)$ and $E_a(1)$ represent the activation energy for electron-hole recombination and the activation energy for the generation of water oxidation intermediates, respectively. The arrows express the direction of reactions. The $E_a(r)$ values for the UB of ATA, LB of ATA, and the LSPR of AT are listed in the table superimposed on the figure.

Based on the reaction model shown in Figure 4.12, the IPCE for the water oxidation process, with ATA and AT as photoanodes, can be expressed by the following equation:

$$\text{IPCE} = N\boldsymbol{\Phi}_{inj}\left(\frac{k_1}{k_r[e^-]+k_1}\right)\left(\frac{k_2}{k_r'[e^-]+k_2}\right) \qquad 4.1$$

In this context, $\boldsymbol{\Phi}_{inj}$ represents the electron injection efficiency, N denotes the number of generated electrons per unit of incident light power, and $[e^-]$ is the concentration of electrons in the CB. Since water oxidation is a kinetically slow reaction, approximately six orders of magnitude slower than typical electron-hole recombination processes,[28] Therefore, the term $k_r[e^-]$ is much larger than k_1.

Taking the natural logarithm of both sides of Equation (1) gives:

$$ln(\text{IPCE}) = ln\left(N\boldsymbol{\Phi}_{inj}\right) + ln(k_1) - ln(k_r[e^-]) + ln(k_2) - ln(k_r'[e^-] + k_2) \qquad 4.2$$

Since the constant term $ln\left(N\boldsymbol{\Phi}_{inj}\right)$ does not influence the slope when the data is fitted to the Arrhenius equation, it does not affect the determination of the activation energy. Therefore, $ln\left(N\boldsymbol{\Phi}_{inj}\right)$ is omitted from the analysis of activation energy. Arrhenius analysis of the last term, $ln(k_r'[e^-] + k_2)$, in Equation 4.2 leads to a pseudo-linear relationship with the apparent activation energy $E_a(2)'$, as the chemical process k_2 has a much larger activation energy than $E_a(r')$ required for electrons to escape the shallow trap. Given that $E_a(2)' \cong E_a(2)$, the activation energy $E_a(r')$ is effectively offset in this analysis. Furthermore, it is important to note that the term $ln(k[e^-])$ can be separated into $lnk + ln[e^-]$, and $[e^-]$ has no activation energy as judged from the sharp rise of the transient signals (Figures 4.9a-c), which is almost equivalent to the response function of our transient measurement system. Then, $ln[e^-]$ should have a constant value without temperature-related function and does not affect the Arrhenius analysis. Thus, $E_a(1)$ can be expressed as follows:

$$E_a(\text{IPCE}) + E_a(r) = E_a(1) \qquad 4.3$$

where $E_a(\text{IPCE})$, $E_a(r)$ and $E_a(1)$ represent the activation energy of photocurrent generation, the activation energy of electron–hole recombination and the activation energy of water oxidization intermediates generation, respectively.

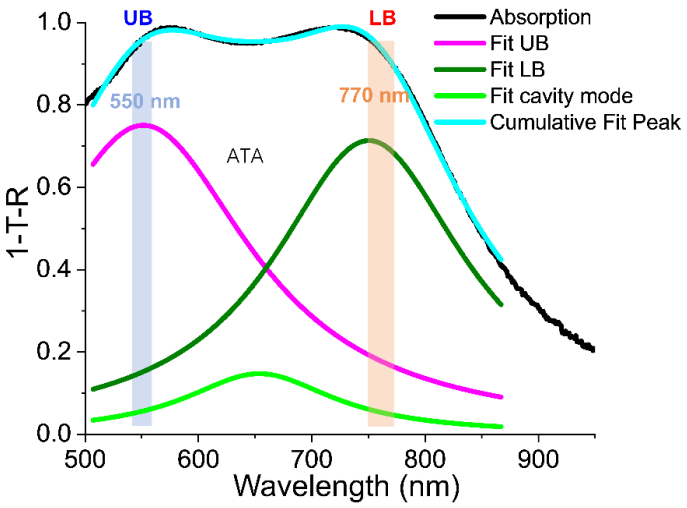

Figure 4.13 Absorption spectrum of ATA, superposed with its spectral separation via

Lorentzian fitting. The pink curve and green curve represent the Lorentz fits of the UB and LB, respectively. The green curve indicates the nanocavity mode, and the cyan curve shows the cumulation of all the fittings. At 550 nm, the contributions from the upper and lower branches are 79% and 16%, respectively. At 770 nm, the contributions are 19% from the upper branch and 77% from the lower branch.

To accurately determine the $E_a(1)$ for UB and LB excitation in ATA, we separated the UB and LB absorption bands using Lorentz fitting, as shown in Figure 4.13. We selected wavelengths of 550 nm at UB and 770 nm at LB to minimize their overlap and calculate the $E_a(1)$ values for the respective excitations. For AT, we chose a wavelength of 650 nm to determine the $E_a(1)$ value. Using Equation 4.3, the calculated $E_a(1)$ values for ATA at UB and LB were 17 ± 1.4 kJ/mol and 21 ± 0.9 kJ/mol, respectively, while for AT, the $E_a(1)$ value was 16 ± 1.9 kJ/mol (Table 3).

Table 3 Activation energy of electron-hole recombination, IPCE measurement and water oxidation intermediates generation.

	ATA@UB (kJ/mol)	ATA@LB (kJ/mol)	AT@LSPR peak (kJ/mol)
$E_a(r)$	3.0±0.8	4.9±0.6	8.3±1.9
$E_a(IPCE)$	14±1.2	16±0.7	7.8±0.8
$E_a(1)$	17±1.4	21±0.9	16±1.9

To verify that the obtained $E_a(1)$ corresponds to the generation of water oxidation intermediates, we introduced TEOA, a sacrificial electron donor with a more negative oxidation potential than water, which is known to efficiently inject electrons into holes, into the electrolyte solution.[19] The temperature dependence of the IPCE was then observed (Figures 4.14 and 4.15).

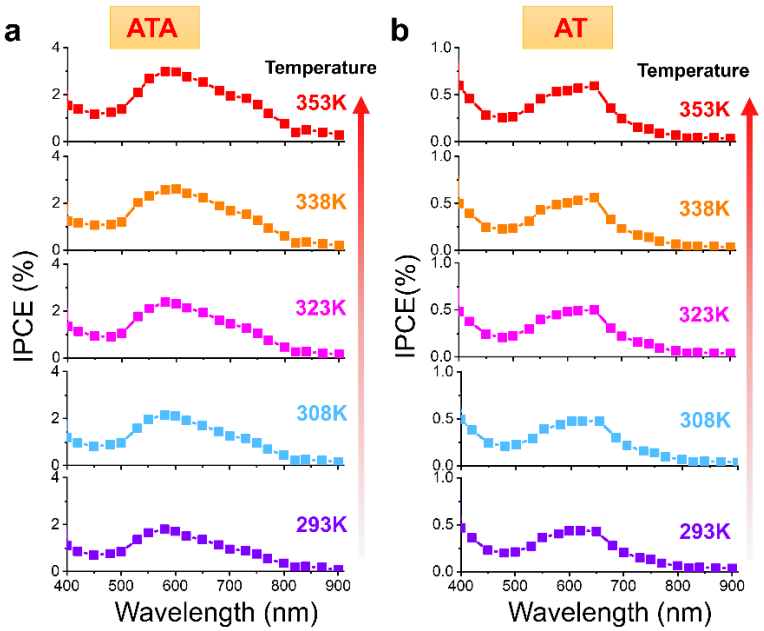

Figure 4.14 Temperature-dependent IPCE of ATA (a) and AT (b) measured in 0.1 mol/dm^3 KOH with the addition of 1vol% TEOA.

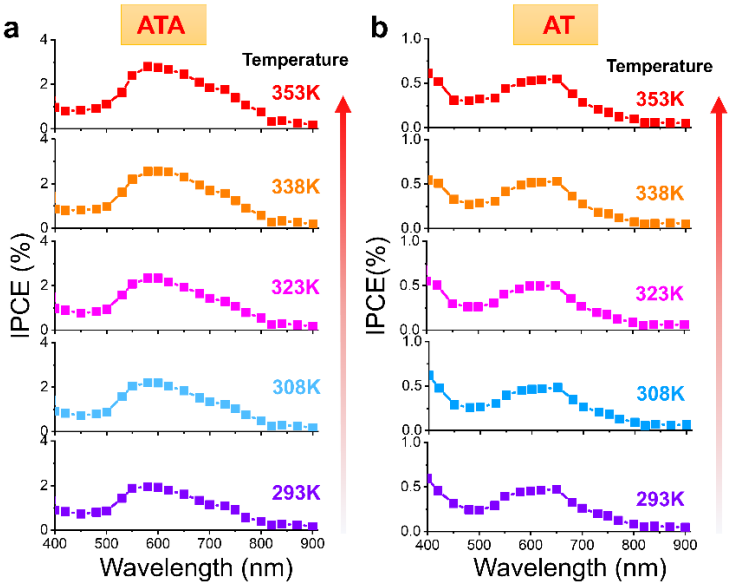

Figure 4.15 Temperature-dependent IPCE of ATA (a) and AT (b) measured in 0.1 mol/dm^3 KOH with the addition of 10 vol% TEOA.

As shown in the figures, adding TEOA increased the IPCE in both ATA and AT photoanodes. This enhancement suggests that TEOA facilitates more efficient electron injection into the holes generated on the Au/TiO_2 surface compared to water or OH^-, thereby reducing electron recombination. The wavelength dependence of E_a(IPCE) with TEOA, presented in Table 4, shows that the presence of TEOA lowers

E_a(IPCE) compared to its absence. Assuming electron injection into the TEOA-generated holes produces reaction intermediates, we calculated the activation energy for their formation using Equation 4.3. For UB excitation in ATA, the $E_a(1)$ values were 10 ± 1.0 kJ/mol and 6.2 ± 0.9 kJ/mol for 1 vol% and 10 vol% TEOA, respectively. For LB excitation, the $E_a(1)$ values were 15 ± 1.2 kJ/mol and 13 ± 1.3 kJ/mol, respectively. In the case of AT, the $E_a(1)$ values for 1 vol% and 10 vol% TEOA were 13 ± 1.9 kJ/mol and 11 ± 1.9 kJ/mol, respectively. The results in Table 5 demonstrate that the $E_a(1)$ values with TEOA are lower than those without it, suggesting that the activation energy measured in the KOH electrolyte corresponds to the energy required for generating water oxidation intermediates.

Table 4 Activation energy of photocurrent generation ($E_a(IPCE)$) in different electrolytes.

	ATA@UB (kJ/mol)	ATA@LB (kJ/mol)	AT@LSPR peak (kJ/mol)
$E_a(IPCE)\_H_2O$	14±1.2	16±0.7	7.8±0.8
$E_a(IPCE)\_1vol\%TEOA$	6.5±0.6	10±1.0	4.6±0.3
$E_a(IPCE)\_10vol\%TEOA$	3.2±0.4	8.4±1.1	2.5±0.3

Table 5. Activation energy of intermediates generation ($E_a(1)$) in different electrolytes.

	ATA@UB (kJ/mol)	ATA@LB (kJ/mol)	AT@LSPR peak (kJ/mol)
$E_a(1)\_H_2O$	17±1.4	21±0.9	16±1.9
$E_a(1)\_1vol\%TEOA$	10±1.0	15±1.2	13±1.9
$E_a(1)\_10vol\%TEOA$	6.2±0.9	13±1.3	11±1.9

4.3.5 Proposed mechanism in water oxidation under strong coupling condition

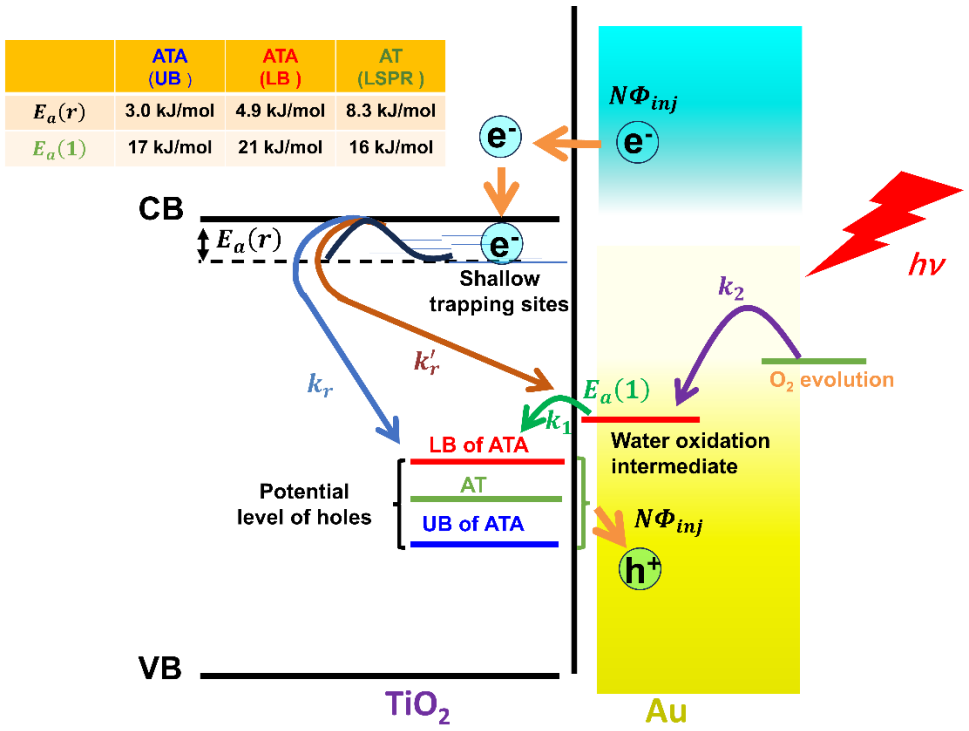

Figure 4.16 The schematic illustrates the generation of water oxidation intermediates facilitated by holes at varying potential levels. Arrows are used to depict the direction of electron flow. The values of $E_a(r)$ and $E_a(1)$ for the UB of ATA, LB of ATA, and the LSPR of AT are listed in the table superimposed on the figure.

The energy levels of holes injected intoTiO_2 via the LSPR band are influenced by the wavelength of the light irradiation. Holes from the UB possess the most positive potential, those from the LB exhibit more negative potentials, and those from AT are located at intermediate levels, as depicted in the schematic diagram in Figure 4.16. Although the presence of $E_a(1)$ could be attributed to the endergonic nature of electron injection into these holes, the observed $E_a(1)$ values (16–21 kJ/mol, Table 3) are notably small. This suggests that the electrochemical level of the water oxidation intermediate may lie slightly above the hole energy level, with a small barrier likely arising from a level crossing between the initial and final states (Figure 4.16). While the precise electrochemical level of the water oxidation intermediate remains to be determined in future studies, it is reasonable to infer that holes with more negative electrochemical potentials generally exhibit higher activation energies. This correlation

provides insight into the energetics of water oxidation and highlights the dependence of activation energy on the potential levels of the photogenerated holes.

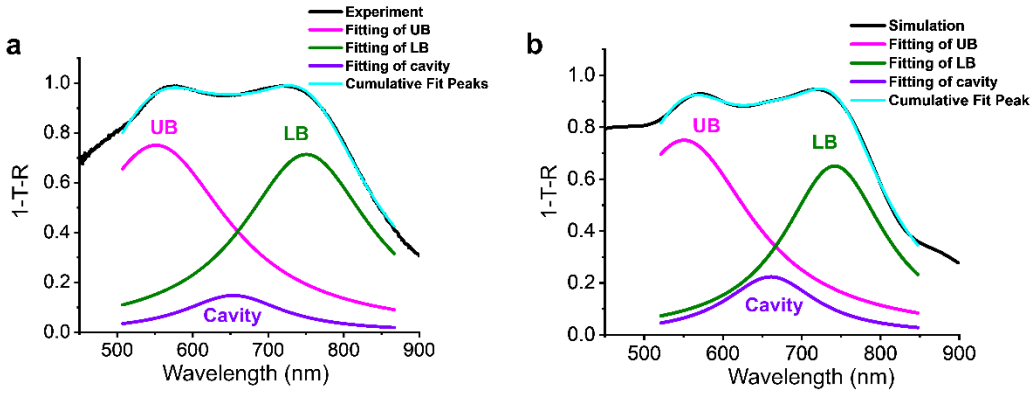

Figure 4.17 Experimental (a) and simulated (b) absorption spectrum of ATA with a TiO_2 thickness of 30 nm, superposed with its spectral separation via Lorentzian fitting. The pink curve and green curve represent the Lorentz fits of the UB and LB, respectively. The purple curve indicates the nanocavity mode, and the cyan curve shows the cumulation of all the fittings. The experimental spectrum corresponds to measurements from an inhomogeneous distribution of Au NPs, while the simulated spectrum reflects the response of a uniform distribution of Au NPs.

This hypothesis is supported by the observation that $E_a(1)$ for LB excitation in ATA is larger than in AT. Conversely, $E_a(1)$ for UB excitation is slightly smaller than that for LB but slightly larger than that in AT (Table 3). Based on these results, we propose that transitions from UB to LB occur in the ATA photoanode. Under typical modal strong coupling conditions, UB and LB modes are orthogonal, making direct transitions unlikely. However, in our ATA structure, the broadening of the LSPR band due to size non-uniformity among Au NPs leads to overlap between the UB and LB bands (see Figure 4.17a), potentially facilitating transitions.

This hypothesis is further supported by FDTD simulations, which indicate that spectral overlap persists even with size-uniform Au NPs (11.5 nm), as shown in Figure 4.17b. When UB in ATA is excited, two pathways may coexist: a direct process generating holes from UB with inherently smaller $E_a(1)$ and an indirect process where transitions to LB generate holes with larger $E_a(1)$. These processes likely produce holes with varying potentials, and their reactions with water or OH^- result in an averaged $E_a(1)$ value across UB and LB, yielding a value comparable to that of AT.

The frequency factors for the ATA and AT photoanodes were further examined using the Arrhenius equation. To focus on the LB excitation in the ATA structure，where transitions from UB to LB may also contribute，we compared the frequency factors of the LB in ATA with those of AT. As depicted in Figure 4.18, the frequency factor-related term, $ln(\boldsymbol{A}_0)$, derived from the Arrhenius plot for the LB of the ATA photoanode, was approximately 40 times larger than that for AT. This result indicates the significantly enhanced efficiency of the water photooxidation reaction in the ATA photoanode compared to AT. The observed enhancement is likely linked to quantum coherence facilitated by the nanocavity, which mediates interactions between LSPR modes in the ATA structure and promotes efficient injection of hot electrons into TiO_2 under modal strong coupling conditions. In our previous study using the ATA structure, we reported that the quantum efficiency of electron injection from gold nanoparticles to TiO_2 increases with the number of gold nanoparticles under the quantum coherence.[10] From the SEM image shown in Figure 4.4b, the Au-NPs in ATA structure shows high particle density, which might consequently facilitate the injection of hot electrons into TiO_2 under the quantum coherence mediated through the nanocavity between LSPR modes.

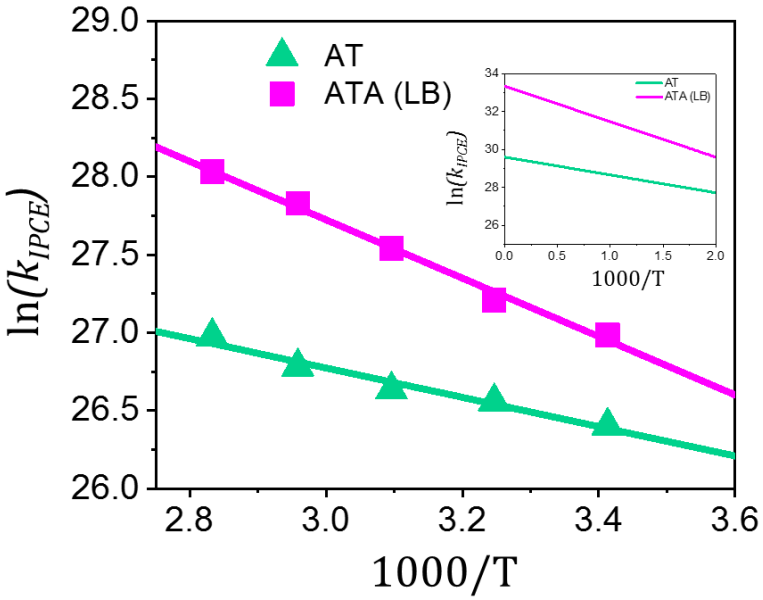

Figure 4.18 Arrhenius plots obtained from temperature-dependent IPCE measurements for the LB of the ATA structure and the absorption band of the AT structure (black), with their respective linear fits superimposed. The inset highlights the vertical intercepts of the linear fits, providing insight into the frequency factors associated with photocurrent generation.

4.4 Conclusions

In this chapter, the ATA structure was employed to study photogenerated electron transfer kinetics and water oxidation intermediates generation under plasmon–nanocavity strong coupling conditions. Temperature-dependent TA and IPCE measurements were conducted to investigate these processes. The small $E_a(r)$ values obtained from TA measurements for both ATA and AT structures indicate that the injected electrons are predominantly trapped in shallow trap sites within TiO_2. From temperature-dependent IPCE measurements, the $E_a(IPCE)$ was calculated, alongside $E_a(1)$, for further analysis. Notably, when the LB of ATA was excited, $E_a(1)$ was higher compared to AT excitation, indicating that holes generated by LB excitation possess a more negative electrochemical potential than those generated by AT excitation.

Additionally, the analysis of $E_a(1)$ values across ATA (UB and LB) and AT suggests a rapid transition from the UB to the LB in ATA, due to the partial spectral overlap between these modes. Moreover, the frequency factor for photocurrent generation in the ATA structure was found to be 40 times higher than that of the AT structure lacking strong coupling. This significant enhancement is likely due to quantum coherence established between the LSPR of Au NPs within the nanocavity of the ATA structure, which facilitates more efficient injection of hot electrons into TiO_2 under modal strong coupling conditions.

4.5 References

[1] Clavero, C. Plasmon-induced hot-electron generation at nanoparticle/metal-oxide interfaces for photovoltaic and photocatalytic devices. *Nat. Photonics* **2014**, *8*, 95-103.

[2] Linic, S.; Christopher, P.; Ingram, D. B. Plasmonic-metal nanostructures for efficient conversion of solar to chemical energy. *Nat. Mater.* **2011**, *10*, 911-921.

[3] Nishijima, Y.; Ueno, K.; Yokota, Y.; Murakoshi, K.; Misawa, H. Plasmon-assisted photocurrent generation from visible to near-infrared wavelength using a Au-nanorods/TiO_2 electrode. *J. Phys. Chem. Lett.* **2010**, *1*, 2031-2036.

[4] Gao, S.; Ueno, K.; Misawa, H. Plasmonic antenna effects on photochemical

reactions. *Acc. Chem. Res.* **2011**, *44*, 251-260.

[5] Liu, Z.; Hou, W.; Pavaskar, P.; Aykol, M.; Cronin, S. B. Plasmon resonant enhancement of photocatalytic water splitting under visible illumination. *Nano Lett.* **2011**, *11*, 1111-1116.

[6] Gomes Silva, C.; Juárez, R.; Marino, T.; Molinari, R.; García, H. Influence of excitation wavelength (UV or visible light) on the photocatalytic activity of titania containing gold nanoparticles for the generation of hydrogen or oxygen from water. *J. Am. Chem. Soc.* **2011**, *133*, 595-602.

[7] Shi, X.; Ueno, K.; Oshikiri, T.; Sun, Q.; Sasaki, K.; Misawa, H. Enhanced water splitting under modal strong coupling conditions. *Nat. Nanotechnol.* **2018**, *13*, 953-958.

[8] Suganami, Y.; Oshikiri, T.; Shi, X.; Misawa, H. Water oxidation under modal ultrastrong coupling conditions using gold/silver alloy nanoparticles and Fabry–Pérot nanocavities. *Angew. Chem. Int. Ed.* **2021**, *60*, 18438-18442.

[9] Cao, Y.; Shi, X.; Oshikiri, T.; Zu, S.; Sunaba, Y.; Sasaki, K.; Misawa, H. Near-field engineering for boosting the photoelectrochemical activity to a modal strong coupling structure. *Chem. Commun.* **2021**, *57*, 524-527.

[10] Liu, Y.-E.; Shi, X.; Yokoyama, T.; Inoue, S.; Sunaba, Y.; Oshikiri, T.; Sun, Q.; Tamura, M.; Ishihara, H.; Sasaki, K. Quantum-coherence-enhanced hot-electron injection under modal strong coupling. *ACS Nano* **2023**, *17*, 8315-8323.

[11] Zang, X.; Shi, X.; Suganami, Y.; Liu, Y.-E.; Oshikiri, T.; Misawa, H. Investigation of enhanced water oxidation under plasmon–nanocavity strong coupling using in situ electrochemical surface-enhanced Raman spectroscopy. *J. Phys. Chem. C* **2023**, *127*, 15087-15095.

[12] Suzuki, K.; Li, X.; Wang, Y.; Nagasawa, F.; Murakoshi, K. Active intermediates in plasmon-induced water oxidation at Au nanodimer structures on a single crystal of TiO_2. *ACS Energy Lett.* **2020**, *5*, 1252-1259.

[13] Colombo Jr, D. P.; Roussel, K. A.; Saeh, J.; Skinner, D. E.; Cavaleri, J. J.; Bowman, R. M. Femtosecond study of the intensity dependence of electron-hole dynamics in TiO_2 nanoclusters. *Chem. Phys. Lett.* **1995**, *232*, 207-214.

[14] Skinner, D. E.; Colombo Jr, D. P.; Cavaleri, J. J.; Bowman, R. M. Femtosecond investigation of electron trapping in semiconductor nanoclusters. *J. Phys. Chem.* **1995**, *99*, 7853-7856.

[15] Shi, X.; Ueno, K.; Takabayashi, N.; Misawa, H. Plasmon-enhanced photocurrent generation and water oxidation with a gold nanoisland-loaded titanium dioxide photoelectrode. *J. Phys. Chem. C* **2013**, *117*, 2494-2499.

[16] Hoang, C. V.; Hayashi, K.; Ito, Y.; Gorai, N.; Allison, G.; Shi, X.; Sun, Q.; Cheng, Z.; Ueno, K.; Goda, K. Interplay of hot electrons from localized and propagating plasmons. *Nat. Commun.* **2017**, *8*, 771.

[17] Hanke, T.; Krauss, G.; Träutlein, D.; Wild, B.; Bratschitsch, R.; Leitenstorfer, A. Efficient nonlinear light emission of single gold optical antennas driven by few-cycle near-infrared pulses. *Phys. Rev. Lett.* **2009**, *103*, 257404.

[18] Abe, R. Recent progress on photocatalytic and photoelectrochemical water splitting under visible light irradiation. *J Photoch Photobio C* **2010**, *11*, 179-209.

[19] Cao, Y.; Oshikiri, T.; Shi, X.; Ueno, K.; Li, J.; Misawa, H. Efficient hot‐electron transfer under modal strong coupling conditions with sacrificial electron donors. *ChemNanoMat* **2019**, *5*, 1008-1014.

Chapter 5

Conclusions and Future perspectives

5.1 Conclusions

In this thesis, we primarily focus on electron transfer and water splitting within the visible region using an Au nanostructure (NS)/TiO_2/Au film (ATA) system under strong coupling conditions. Upon photoexcitation of ATA, hybrid states formed through strong coupling between the nanocavity and LSPR modes emerge at wavelengths shorter and longer than the original resonant wavelengths of the Au NS LSPR, thereby broadening the absorption spectrum and enhancing light-harvesting efficiency. We fabricated a strong coupling Au nanodisks (NDs)/TiO_2/Au film (ATA) structure, where the shape of the Au NDs was precisely controlled using electron-beam lithography. Additionally, the interfacial modification of the Au NDs/TiO_2 with a Ti film, which exhibits notable energy absorption capabilities and a higher density of states (DOS) around its Fermi level, enhanced the generation of higher-energy electrons from Ti, thereby improving the efficiency of electron injection into TiO_2. Subsequently, Subsequently, Au nanoparticles (NPs) were loaded onto the surface of the TiO_2/Au film via annealing of the Au film, replacing the Au NDs. This approach was employed to further investigate the activation energy associated with electron injection into TiO_2 and the generation of water oxidation intermediates under strong coupling conditions.

In the chapter 2, the effect of the Ti film at the Au NDs/TiO_2 interface on the near-field properties of the Au NDs/Ti/TiO_2/Au film (ATTA) structure was investigated using a PEEM system. The experimental details related to this study are introduced. Near-field mapping and spectral measurements of the ATTA structures reveal that the presence of Ti dampens the near-field enhancement effect, with a further reduction in enhancement observed as the Ti film thickness increases. Additionally, time-resolved PEEM was used to study the influence of Ti film thickness on the dephasing time of hybrid modes in strong coupling ATTA structures. Specifically, it was experimentally

demonstrated that the dephasing time decreases as the Ti film thickness increases. These findings indicate that modifying the Au ND/TiO_2 interface with a Ti film significantly suppresses near-field enhancement and shortens the dephasing time of hybrid modes under strong coupling conditions.

In Chapter 3, we investigated the enhancement of electron transfer facilitated by interfacial modification under modal strong coupling conditions, along with its underlying mechanism. Specifically, the Au NDs/TiO_2 interface in the ATTA structure was modified with a Ti film. Upon excitation of the Au NDs, energy transfer occurs from the Au NDs to the Ti film via the near field. This observation aligns with the findings in Chapter 2, which demonstrated that near-field intensity decreases with increasing Ti film thickness. This energy transfer facilitates the generation of high-energy electrons in the Ti film, which subsequently inject into the conduction band of TiO_2. Notably, the efficiency of photoexcited electron transfer to TiO_2 was enhanced by approximately 1.8 times with the incorporation of a 5 nm-thick Ti film. These results highlight that electron injection efficiency into TiO_2 can be significantly improved through interface engineering, providing a novel design strategy for LSPR-based reaction systems.

In Chapter 4, the photogenerated electron transfer kinetics within TiO_2 and the generation of water oxidation intermediates under plasmon-nanocavity strong coupling conditions were investigated using temperature-dependent TA and IPCE measurements. Temperature-dependent TA measurements revealed that the small activation energies for electron-hole recombination in both Au NPs/TiO_2/Au film (ATA) and Au NPs/TiO_2 (AT) structures indicate that the injected electrons are primarily trapped in shallow trap sites within TiO_2. Through temperature-dependent IPCE measurements, the activation energy for photocurrent generation was determined to assess the process of water oxidation intermediate formation. When the lower branch (LB) of the ATA structure was excited, the activation energy for water oxidation intermediates generation was found to be higher than that observed for AT excitation, indicating that holes generated under LB excitation exhibit a more negative electrochemical potential. Additionally, an analysis of values of activation energy of water oxidation intermediates generation for

the upper branch (UB) and LB of the ATA structure, as well as for the AT structure, revealed evidence of a rapid energy transition from UB to LB in the ATA structure, likely driven by spectral overlap between the two branches. Furthermore, the frequency factor for photocurrent generation in the ATA structure was approximately 40 times higher than that in the AT structure without strong coupling. This remarkable enhancement is attributed to quantum coherence effects arising from the interaction between the LSPR of Au NPs, facilitated by the nanocavity in the ATA structure. These effects significantly enhance the efficient injection of hot electrons into TiO_2 under modal strong coupling conditions.

In summary, this study focused on the optimization and investigation of a modal strong coupling structure, specifically involving the resonance between the LSPR mode of Au NS and the nanocavity mode of the TiO_2/Au film. A strategy was proposed to enhance electron transfer efficiency through Au NS/TiO_2 interfacial modification with a Ti film under strong coupling conditions. It was demonstrated that the Ti film's exceptional energy absorption capability facilitates the generation of high-energy electrons, which, in turn, enhances electron injection into TiO_2. Furthermore, the activation energies for electron-hole recombination and photocurrent generation were estimated using temperature-dependent TA and incident IPCE measurements. These analyses allowed for the determination of the activation energy for water oxidation intermediates generation. By evaluating these activation energies of water oxidation generation, insights were gained into the electrochemical potential levels of holes trapped at surface states at the Au/TiO_2 interface, contributing to a deeper understanding of the mechanisms underlying water oxidation.

5.2 Future perspectives

Building on the findings of this thesis, a forward-looking perspective can be proposed for the development of plasmon-induced solar energy conversion devices as a sustainable energy solution aligned with green societal goals. The ultimate aim is to realize a long-term stable plasmon-enhanced solar energy device capable of efficiently

utilizing visible light. Achieving this goal involves optimizing plasmon-induced electron transfer through precise control of metal nanostructure components and modifications at the metal/semiconductor interface with additional materials. The modal strong coupling ATA structure utilized in this study serves as a photoelectrochemical cell, where charge carriers are generated and separated at the interface between the metal nanoparticle (NP) and nanoscale material. By carefully selecting appropriate metal NS and semiconductor materials, the photochemical fuel energy conversion efficiency could be significantly enhanced under plasmon-nanocavity strong coupling conditions. Moreover, this approach holds promise for application beyond photoelectrochemical cells, extending to solid-state devices such as plasmon-enhanced solar cells, potentially advancing the efficiency and practicality of solar energy technologies.

According to the views mentioned above, suggestions for further work are:

(1) To improve the electron transfer, alloy metal NPs could be loaded on the surface of TiO_2 film instead of Au NPs. Alloying can introduce charge trapping sites or promote directional charger flow, reducing electron-hole recombination. For example, Au-Pd alloys, where the Pd serves as a co-catalyst that traps electrons and facilities their transfer to TiO_2. This is not only enhancing charge transfer but also improves the catalytic activity for subsequent reactions, including water splitting and CO_2 reduction.

(2) Two-dimensional materials like MoS_2 and graphene enhance charge transfer efficiency by acting as conductive bridges with unique band alignments and high mobility. For instance, MoS_2 can accept photogenerated electrons from Au, reducing recombination, while graphene facilitates rapid charge transfer into TiO_2 due to its excellent conductivity and seamless interface.

(3) Combining additional materials, such as MoO_3 or Cu, with Au and TiO_2 creates synergistic systems that optimize light absorption, energy band alignment, and charge mobility. For example, an Au-TiO_2-MoO_3 composite can utilize plasmonic enhancement from Au, charge separation by TiO_2, and the strong oxidizing ability

of MoO_3, resulting in superior photocatalytic performance.

Publication List

1. **E. Cao**, X. Shi, H. Inoue, T. Oshikiri, Y. Liu, H. Misawa,
   "Activation Energy in the Electron Transfer Process and Water Oxidation Intermediate Generation Under Plasmon-Nanocavity Strong Coupling"
   Journal of Physical Chemistry C **2025**, 129(3), 1590-1597.
2. **E. Cao**, X. Shi, T. Oshikiri, Y. Liu, Q. Sun, K. Sasaki, H. Misawa,
   "Improving Charge Transfer under Strong Coupling Conditions via Interfacial Modulation"
   ACS Photonics **2024**, 11(3), 1205-1212.
3. Q. Yan, **E. Cao**, X. Hu, Z. Du, Y. Ao, S. Chu, Q. Sun, X. Shi, C. Chan, Q. Gong, H. Misawa,
   "Edge states in plasmonic meta-arrays"
   Nanophotonics, **2022**, 11(15), 3495-3507.
4. Q. Yan, **E. Cao**, Q. Sun, Y. Ao, X. Hu, X. Shi, Q. Gong, H. Misawa,
   "Near-Field Imaging and Time-Domain Dynamics of Photonic Topological Edge States in Plasmonic Nanochains"
   Nano letters, **2021**, 21(21), 9270-9278.
5. S. Zu, Q. Sun, **E. Cao**, T. Oshikiri, H. Misawa,
   "Revealing the Chiroptical Response of Plasmonic Nanostructures at the Nanofemto Scale"
   Nano letters, **2021**, 21(11), 4780-4786.